DEVELOPMENT OF A MULTIFOCAL CONFOCAL FLIM MICROSCOPE

DEVELOPMENT OF A MULTIFOCAL CONFOCAL FLUORESCENCE LIFETIME IMAGING MICROSCOPE FOR HIGH-CONTENT SCREENING APPLICATIONS

By

ANTHONY TSIKOURAS, B.ENG.

A Thesis

Submitted to the School of Graduate Studies

In Partial Fulfillment of the Requirements for the Degree

Doctor of Philosophy

McMaster University

DOCTOR OF PHILOSOPHY (2017) McMaster University

Department of Engineering Physics Hamilton, Ontario

TITLE:	Development of a multifocal confocal fluorescence lifetime imaging microscope for high-content screening applications
AUTHOR:	Anthony Tsikouras, B.Eng., McMaster University
SUPERVISOR:	Qiyin Fang, Ph.D.
NUMBER OF PAGES:	xvi, 103

Lay Abstract

Fluorescent proteins are commonly used to tag subcellular targets so that they can easily be distinguished with a fluorescence microscope. While this can help visualize where different organelles and proteins are located in the cell, a great deal more information can be gained by measuring the fluorescence lifetime at each point in the sample, which is highly sensitive to the microenvironment. Fluorescence lifetime imaging microscopy (FLIM) has the potential to be a powerful technique for testing drug leads in the drug discovery process, although current FLIM systems are not able to provide the high throughput speeds and high temporal resolution required for drug screening. This thesis project has succeeded in improving a highly parallel FLIM microscope by reducing inter-channel crosstalk, implementing an optical scanner, improving power and optical throughput, and investigating future time-resolving instruments. This progress has brought the prototype setup closer to being used in a drug screening environment.

Abstract

Fluorescence lifetime imaging microscopy (FLIM) is an imaging modality that is able to provide key insights into subcellular processes. When used to measure Förster resonance energy transfer (FRET), for instance, it can discern protein-protein interactions and conformational changes. This kind of information is highly useful in the drug screening process in order to determine the effectiveness of drug leads and their mechanisms of action. FLIM has yet to be successfully translated to high-content screening (HCS) platforms due to the high throughput and fine temporal and spatial resolution requirements of HCS.

Our prototype HCS FLIM system uses a time-resolving instrument called a streak camera to multiplex the FLIM scanning process, allowing for 100 confocal spots to be simultaneously scanned across a sample. There have been a few major advancements to the prototype. First the fiber array used to connect the fluorescence channels to the streak camera was characterized. Its alternating fiber delay scheme was successful in greatly reducing optical crosstalk between adjacent channels. Next, an optical beam scanner for parallel excitation beams was designed and implemented, greatly improving the possible scan speeds of the system. The streak camera was upgraded to a higher repetition rate sweep, and modifications to system components and reconstruction procedures were made to accommodate the new sweep unit. A single-photon avalanche diode array was also tested as a possible replacement for the streak camera, and was found to offer photon detection efficiency advantages. Finally, improvements were made to the excitation power and optical throughput of the system in order to reduce the required exposure time.

These advances to the prototype system bring it closer to realizing the requirements of HCS FLIM, and provide a clear picture for future improvements and research directions.

Acknowledgements

I would like to thank my supervisor Dr. Qiyin Fang for his constant support and advice. I am grateful to have worked under a supervisor who is always approachable and willing to discuss the project and any other aspect of graduate studies. You have helped me research more effectively, and provided me with some great opportunities throughout my degree. Thank you for guiding me to where I am now.

I also want to thank the other members of my supervisory committee: Dr. David Andrews, Dr. Joe Hayward and Dr. Richard Berman. You have helped me to better frame a project that is built across a range of disciplines, and I have always been grateful for your advice and insights on different aspects of the project. My research progress always received a significant boost following a committee meeting.

I feel lucky to have been surrounded by a great collection of colleagues from our lab group and others, and I value everyone who has helped me think about my project differently. In particular, I would like to thank Nehad Hirmiz, who is my successor on the project. I am very happy that we were able to work on the project together for the overlap period. Thank you for always being willing to go the extra mile, and carrying out countless experiments and data analyses with me. Thank you to Jin Ning, who worked on the project before me and helped me become familiar with the instruments. Thank you also to Allison Yeh, Sharon Goh and Elizabeth Osterlund for all of your help on the biochemistry side and with cell culturing. Thank you to Zhaojun Nie and Darek Palubiak for help in understanding some aspects of the technical side.

Thank you to my parents as well, who have always been supportive of me, even when they can’t understand exactly what my project is. And a special thank you to my wife Afrisa, for always being by my side through every stage of the Ph.D., and making my life easier and more enjoyable in the process.

Table of Contents

List of Figures

List of Tables

List of Abbreviations

1D	one dimensional
2D	two dimensional
3D	three dimensional
AIF	apoptosis inducing factor
AP	afterpulsing probability
AR	antireflective
Bcl-2	B-cell lymphoma 2
CCD	charge coupled device
CMOS	complementary metal oxide semiconductor
DCR	dark count rate
DNA	deoxyribonucleic acid
DFF-40	DNA fragmentation factor 40
FD	frequency domain
FLIM	fluorescence lifetime imaging microscopy
FRET	Förster resonance energy transfer
FWHM	full-width at half-maximum
GaAsP	gallium arsenide phosphide
galvo	galvanometer
HCS	high-content screening
HIV	human immunodeficiency virus
ICCD	intensified CCD
IRF	impulse response function
MCP	microchannel plate
NA	numerical aperture
PDE	photon detection efficiency
PMT	photomultiplier tube
PPI	protein-protein interactions
sCMOS	scientific CMOS
SNR	signal-to-noise ratio
SPAD	single-photon avalanche diode
STED	stimulated emission depletion
TAC	time-to-amplitude converter
TCSPC	time-correlated single-photon counting
USB	universal serial bus
WF	widefield

Declaration of Academic Achievement

Academic Works

Publications

A. Tsikouras, J. Ning, S. Ng, P. Sinclair, R. Berman, D.W. Andrews, Q. Fang, "Streak camera crosstalk reduction using a multiple delay optical fiber bundle." Optics Letters 37: 250-252 (2012).

A. Tsikouras, R. Berman, D.W. Andrews, Q. Fang, "High-speed multifocal array scanning microscopy using refractive window tilting." Biomedical Optics Express 6(10): 3737-3747 (2015).

A. Tsikouras, P. Peronio, I. Rech, N. Hirmiz, M. J. Deen, Q. Fang, "Characterization of SPAD array for multifocal high-content screening applications." MDPI Photonics 3(4): 56 (2016).

Conference Presentations

A. Tsikouras, J. Ning, S. Ng, P. Sinclair, R. Berman, D.W. Andrews, Q. Fang, "High throughput FLIM-FRET nanoimaging for quantification of protein-protein interactions." SPIE Optics + Photonics, 8460-04 (2012).

A. Tsikouras, S.C. Yeh, Q. Fang, "Instrumentation design for high-speed FLIM for applications in high-content screening," Electrochemical Society Meeting 225, 1487 (2014).

A. Tsikouras, "Designing a scanning system for multiplexed confocal FLIM microscopy using refractive window tilting." Society of Biomolecular Imaging and Informatics 1 (2015).

Provisional Patents

A. Tsikouras, Q. Fang, WO 2015031988 A1, "Foci array scanning through an adjusting refractive medium," Mar. 12, 2015.

A. Tsikouras, Q. Fang, WO 2015024112 A1, "Apparatus, method and system for calibration of a streak camera," Feb. 26, 2015.

Project Contributions

The original system as highlighted in the Introduction is inherited from the work of the previous Masters student Jin Ning. This system was designed with Dr. Qiyin Fang, Dr. Richard Berman and Dr. David Andrews.

All manuscripts were written by me, and revised with feedback from the coauthors.

The fiber delay scheme (Chapter 3) was developed by Jin Ning and Dr. Qiyin Fang. The experiments to characterize the optical crosstalk and scan the *Convallaria* sample were performed and analyzed by me in consultation with Dr. Qiyin Fang. The reconstruction script was developed by me, though a previous version had been used by Jin Ning. The fiber intensity normalization script was developed by me.

The window galvanometer scanner (Chapter 4) was conceived, designed and implemented by me. Undergraduate researcher Ian Wigboldus performed early calculations on alternative scanning options. The hardware control of the galvanometer through an Arduino microcontroller was done by me and undergraduate researcher Iman Lau. Linearity and uniformity experiments were performed and analyzed by me, as well as the scan of *Convallaria*. Step and tilt alignment procedures and live feedback through a microscope camera were developed by me, and performed by me and Nehad Hirmiz. A custom window galvanometer holder that connects to the microscope side port was designed by me and fabricated with Thorlabs parts modified in the machine shop.

The 32-channel SPAD array experiments (Chapter 5) were conceived by me and Dr. Qiyin Fang, and performed and analyzed by me and Pietro Peronio. Previous experiments on single SPAD and 8-channel SPAD arrays were performed by me and Matteo Crotti. I performed the theoretical calculations relating SPAD characteristics to FLIM requirements, and calculating the data throughput of the future 32 x 32 SPAD array concept.

The 40 MHz synchroscan was purchased from the manufacturer, Optronis. I requested a reduced sweep amplitude setting at the cost of time axis linearity. I designed the new 2D-1D fiber array to pair with the streak camera's synchroscan unit, and conceived of the new streak decay scheme. I developed and implemented the linearization algorithm as well as the barrel distortion correction, though Nehad Hirmiz has since made adjustments. I designed the 7-delay reference fiber for real-time streak camera drift correction, based on ideas from Dr. Qiyin Fang and Patrick Summ from Optronis.

The square core fiber beam shaper was based on the existing Borealis product from Spectral Applied Research, and provided by them based on our specifications. The antireflective coating of scanner windows and microlens arrays was done at the suggestion of Dr. Qiyin Fang.

The C++ acquisition code was developed by me to replace the previous LabView program. This included interfacing with the motorized microscope stage, the delay generator and the CCD camera in the original system, and the window galvanometer scanners and the sCMOS camera after the system upgrades. Modifications to provide real-time reconstruction feedback were done by Nehad Hirmiz.

Chapter 1

Introduction

The pharmaceutical industry has been experiencing increasingly rising costs associated with drug development. A significant reason for this trend is due to the lack of success of drug candidates during clinical trials, as only 10% of the drug candidates succeed in all clinical trial phases and are ultimately approved [1, 2]. As the main cost of drug development is the clinical phase, this represents a near-tenfold increase in cost of developing a single approved drug, in order to cover the costs of the failed drugs [1, 3]. There is a significant need for a new screening modality that can provide more telling results at the early stage to prevent such a high percentage of failures and their costs.

1.1. Motivation

A very desirable screening feature is the ability to monitor protein-protein interactions (PPI). The interactions of proteins within a cell are responsible for how a cell reacts to internal and external signals. Many diseases are related to imbalances in these PPI pathways, causing a protein-mediated event to be over- or under-regulated. The members of the Bcl-2 family of proteins are known to promote and inhibit apoptosis – also known as programmed cell death – and an imbalance in their expression levels can cause diseases associated with overactive or underactive rate of apoptosis [4, 5, 6]. Being able to monitor how drug leads modulate PPI pathways would provide valuable information as to the working mechanism of the drug lead [5, 7].

The ability to measure PPIs is not straightforward, as these interactions occur at a scale of 10 nm, which is well below the optical diffraction limit [8, 9]. Förster resonance energy transfer (FRET), however, is a technique that is very sensitive to small distances between fluorophores. FRET is the process by which the excited energy of a “donor” fluorophore is non-radiatively transferred to an “acceptor” fluorophore [10, 11]. The likelihood of FRET occurring is strongly dependent on the proximity of the acceptor, with the FRET efficiency inverse proportional to the sixth power of distance separation. By attaching FRET pairs of fluorophores to intracellular proteins of interest, it is possible to detect PPIs such as binding, cleaving and conformational changes [5, 12].

While there are a few ways to measure FRET, including spectrally and by polarization anisotropy, fluorescence lifetime is considered the most reliable measurement technique [13]. It is also the most complex and costly method, requiring excitation sources that can generate sub-nanosecond pulses and detectors that can measure the nanosecond decays with fine resolution. The temporal resolution necessary to measure the degree of FRET occurring in a confocal volume is especially fine, since it requires the fitting of a biexponential decay to separate out the FRET and no-FRET components [14].

High-content screening (HCS) is the process by which live cells are treated with a large variety of drug leads and subsequently imaged to measure the drug effectiveness [15]. It is at this stage that better selectivity in advancing drug candidates is required in order to reduce the cost of later failures. While applying FLIM-FRET to HCS would allow for an unprecedented level of biochemical relevance to be attached to phenotypic screening results, a FLIM module would need to meet certain requirements in order to make it suitable for a high-throughput screening platform. The primary requirement is that the imaging must be fast, in order to keep up with the 1 sample per second benchmark of HCS [16]. The system must also be gentle, which means the laser intensity must be kept low in order to prevent photodamage of the cells and photobleaching [17, 18]. Widefield excitation is gentle for fluorescence imaging mode, since the excitation power is spread evenly across the field-of-view. Widefield imaging is unsuitable for screening, however: a confocal approach is required to optically section the sample and remove out-of-focus light to properly discern subcellular components on interest [19]. In order to balance the need for high throughput, gentle excitation and confocal, a multiplexed confocal approach is considered ideal.

The most common multi-point confocal scanner is the Nipkow spinning disk [20, 21]. The spinning disk is patterned with nested spirals of pinholes that, when spun, cover the entire sample in one twelfth of a revolution. At any point in acquisition, the sample is being excited by over one thousand foci. This allows for a widefield approach to achieve all of the benefits of confocal, and the resulting confocal image is painted across an imaging detector. The spinning disk unit is now present in nearly all commercial confocal HCS microscopes [22]. One of the primary advantages of spinning disk confocal is also its drawback: the technique can only be used with a widefield detector. While this allows for virtually no scan reconstruction to be required, it also limits the types of time-resolved detectors that can be used to measure the signal. The only time-resolved widefield detector suitable for FLIM is the gated intensified CCD, but this sensor suffers from poor spatial and temporal resolution, low photon detection efficiency, and high noise [23]. While a FLIM module with a gated intensified CCD was previously provided by Perkin Elmer, it is no longer offered.

A multiplexed confocal technique where there are a number of discrete detectors equal to the number of emission foci would allow for the use of more sensitive and better time-resolving detectors. The gold standard of fluorescence lifetime measurement is time-correlated single-photon counting (TCSPC) [24]. Since TCSPC is a photon counting technique, it has very little noise in its signal, and offers excellent temporal resolution. It is an inherently slow technique, since it requires very low emission levels to prevent distortions to the signal. A multiplexed approach would help mitigate this requirement, however TCSPC detectors (photomultiplier tubes and single-photon avalanche diodes (SPADs)) and their electronics do not currently achieve a high enough degree of multiplexing. The largest multiplexing achieved in a TCSPC detector is only 8 channels [25]. While single-photon avalanche diode arrays are an active field of research, they are only just emerging as a commercial product [26, 27].

Another option for time-resolved measurement is a streak camera, where photocathode-generated electrons are accelerated down a vacuum tube with a time-varying electric field applied perpendicular to the direction of travel [28]. This perpendicular electric field pulls the electrons one way or the other based on their arrival time, and so this axis of the resulting image becomes a temporal axis. Not only are streak cameras able to achieve excellent temporal resolution, but their remaining spatial axis is able to fit a high number of discrete channels. The most deterring aspect of the streak camera is its poor detection efficiency, which is not the best fit for photon-starved applications such as live cell imaging, though its degree of multiplexing is currently unparalleled. It is for this reason that a streak camera-based is pursued in this dissertation.

1.2. Description of the original system

The concept behind the multifocal FLIM solution is to use a large number of foci on the sample, such that each confocal point needs only to be scanned over a subregion of the field of view, and the final image can be reconstructed by stitching together the subregions of all of the confocal points. A two-dimensional (2D) grid of 10 x 10 foci is generated with a microlens array for this purpose. Meanwhile, since the streak camera's entrance slit can only accommodate a one-dimensional (1D) array of channels, a specially designed fiber array is used to reorganise the fibers from a 2D to a 1D arrangement. A streak camera image is acquired for each scan position. Therefore, an N x N scan will produce N^2 streak camera images, which are used to create a 10N x 10N FLIM reconstruction.

The optical setup of the original system is outlined in Figure 1-1. A pulsed diode laser is used as the excitation source. A pair of cylindrical lenses is used to reshape the laser beam from its original elliptical shape to a large circular illumination that can be used to cover the 10 x 10 microlens array. The collimated light is reflected by the dichroic mirror before reaching the first microlens array. The resulting 2D array of excitation foci is generated at the conjugate plane of the microscope's side port, where it is then relayed to the microscope's sample plane. The foci remain stationary as the sample moves: scanning is accomplished by step commands sent to the motorized microscope stage.

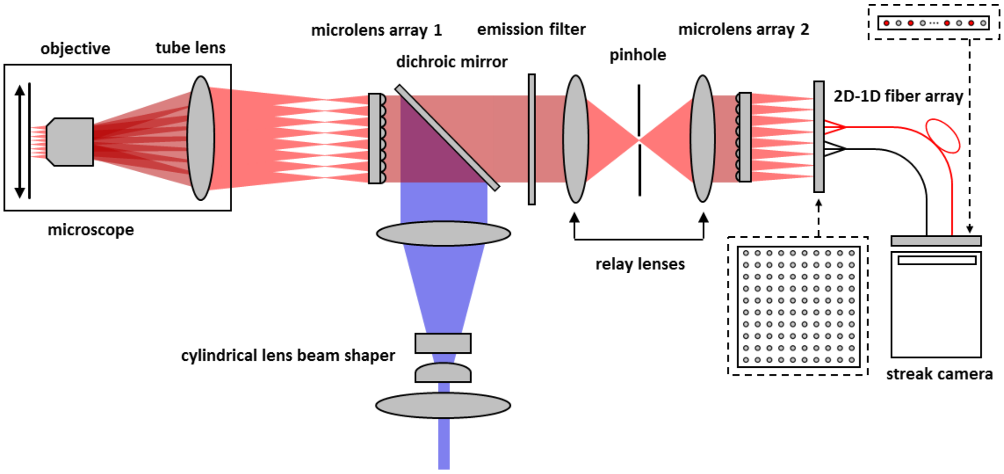

Figure 1-1: Original experimental setup for HCS FLIM module.

The fluorescence light returns back through the side port and is recollimated by the first microlens array. The collimated light from all of the microlenses is focused to a single confocal pinhole in order to reject the out-of-focus light, and then reaches a second microlens array that returns it to a grid of foci. The grid of foci is paired to the 2D end of the 2D-1D fiber array, while the 1D end is coupled to the input slit of the streak camera.

The streak camera slit can accommodate a length of 100 fibers, but there begin to be issues with optical crosstalk when the channels are arranged this tightly. In order to reduce the crosstalk, the optical fibers were staggered in length on the 1D end, such that the fibers alternated between 1 m and 2 m in length. The extra distance of the 2 m fiber results in a 4.8 ns delay, and this causes a spatial separation on the time axis of the streak camera readout, greatly reducing the optical crosstalk.

While the system as described was a successful proof-of-concept, it fell well short of the 1 image per second throughput requirement of an HCS system. With an integration time of 0.5 s per streak camera frame, a 40 x 40 scan (resulting in a 400 x 400 reconstruction) took over 13 minutes to acquire.

There are a few competing bottlenecks for the acquisition speed of the multifocal system. The primary bottleneck is that there is insufficient fluorescence signal collected, such that shorter integration times would result in a significant loss in image quality and lifetime estimation precision. There are two facets to this problem: the initial excitation power and the optical throughput. The excitation power can be improved by upgrading to a higher optical power diode laser model, as well as better matching the excitation band of the targeted donor fluorophore. The laser power could also be improved by increasing the repetition rate to 40 MHz, though the maximum allowed repetition rate is limited by the streak camera's sweep unit. In terms of optical throughput, the excitation power can be improved by better beam shaping that is less wasteful, as well as antireflective coating at each lens interface.

If the light economy is not considered the bottleneck, the slow scanning speed of the microscope stage becomes the limiting factor. An optical beam scanner incorporated into the optical path could provide for faster scanning. This is also fitting for the application, which should be an all-included module, and should not involve unnecessary vibrations of the live cell sample plates. The readout camera's frame rate is also a potentially limiting factor, though high frame rate scientific CMOS cameras are becoming increasingly available.

1.3. Thesis overview

The goal of this research is to improve upon the original design in order to make it a more attractive option for HCS FLIM. In order to realize this, five milestones were achieved.

First, the crosstalk of the optical fiber delay scheme of the 2D-1D fiber was characterized. The fluorescence lifetime of a fluorophore with a known reported lifetime value was also used to confirm that the additional length of fiber did not have an impact on the estimated fluorescence lifetime.

Second, an optical scanner was developed that could scan the entire foci array without needing to move the microscope stage. A novel window-based galvanometer scanner design was implemented to perform the parallel motion of the foci, and the result was validated with a proof-of-principle experiment and a successful scan reconstruction.

Third, a synchroscan sweep unit was implemented on the streak camera, allowing for the repetition rate of the laser to be increased to 40 MHz. In order to use the synchroscan sweep unit, the alternating fiber length difference of the 2D-1D fiber array was redesigned. The non-linear time axis resulting from the sinusoidal synchroscan deflection was characterized and corrected. The fluorescence lifetime of known fluorophores was tested to ensure the successful linearization of the streak camera's time axis.

Fourth, an exploration was done into the use of emerging SPAD array options with parallel TCSPC electronics as a detector alternative to the streak camera. A 32-channel SPAD array was characterized, and the parameters of interest were applied to the HCS FLIM application. The parameters were also used along with the proposed scheme for a future 32 x 32 channel SPAD array to see if the design could provide suitably fast count collection and readout to achieve the high throughput requirements of HCS.

Finally, the light throughput in the experimental setup was improved in many components of the optical path. The original diode laser was replaced with a higher laser power with a better matching wavelength for exciting the target fluorescent protein. The beam shaper was replaced with a square core optical fiber that allowed for better transmission efficiency and significantly improved illumination uniformity. The microlens arrays and scanner windows were also given an antireflective coating to reduce reflection losses at each interface.

1.4. Thesis organization

This Introduction chapter provides an overview of the motivations and challenges for the HCS FLIM project, and outlines the original system from which this thesis work began.

Chapter 2 provides more relevant background on the pharmaceutical drug screening process and highlights the reasons why HCS FLIM could be an important development in the drug discovery process. FLIM is contrasted with other methods of measuring FRET, and the various implementations of FLIM are explored. The case is also made for multifocal confocal FLIM, and various multifocal microscope systems are considered.

Chapter 3 investigates the optical crosstalk of adjacent channels in the streak camera readout, and demonstrates how the fiber delay scheme succeeds in reducing the optical crosstalk. The results show that the optical crosstalk is reduced from 52% to 19% according to our crosstalk metric, and the measured fluorescence lifetimes are not impacted by the differing lengths of optical fiber.

The resulting image reconstructions using the delay scheme show significantly improved contrast due to the suppression of crosstalk signal contributions.

Chapter 4 presents the development and implementation of an optical beam scanner for multifocal applications, using galvanometers fitted with fused silica windows to produce the lateral translations via refraction. Simulations are done to show the shortcomings of using mirror galvanometers for multifocal scanning, and a proof-of-principle is performed to demonstrate the high linearity and uniformity with which the window galvanometer scanner displaces each focal point. The implementation of an XY window galvanometer scanner in the multifocal system shows the successful raster scanning and reconstruction of a fixed sample.

Chapter 5 provides a characterization of a 32-channel SPAD array prototype, and explores the multiplexed TCSPC approach for the application of HCS. The relevant parameters of a SPAD detector and TCSPC circuit are highlighted with a focus on translating them into terms relevant to FLIM. The data collection rate was also investigated based on the concept of a future 32 x 32 SPAD array.

Chapter 6 concludes the thesis, providing a summary of the improvements to the HCS FLIM system, and future direction based on the current system's results and exploration into alternative options.

1.5. Contributions

This thesis is presented as three journal articles from **Chapters 3 to 5**. I wrote the original drafts of each of the articles, and made revisions based on the feedback of the listed coauthors.

Chapter 3 was written on an aspect of the system that was already in place before I began my work, created by Dr. Qiyin Fang and former Masters student Jin Ning. I performed the data acquisition for optical crosstalk measurement and data analysis, while the optical crosstalk metric was devised in talks with Dr. Qiyin Fang. I performed the fluorescence lifetime measurement experiments with Coumarin 6 and estimated the fluorescence lifetimes. I also acquired the scans of Convallaria, while the reconstruction was done by modifying an existing reconstruction script developed by Jin Ning.

I developed the concept of the window galvanometer scanner in **Chapter 4**, as well as the exact parameters for the window. I designed and performed the linearity and uniformity tests for the scanner, and implemented the scanner into the multifocal system. I performed the Convallaria scan and reconstruction. The framing of the article was done with consultation from Dr. Qiyin Fang and Dr. David Andrews.

The fluorescence lifetime experiments for **Chapter 5** were performed and analyzed with Pietro Peronio, and were designed in consultation with Dr. Qiyin Fang. I developed the outline of the article, and performed the calculations to relate SPAD characteristics to HCS requirements, with feedback from Dr. Ivan Rech. I also made the calculations for the theoretical throughput of the 32 x 32 SPAD array, based on discussions with Pietro Peronio and Dr. Ivan Rech.

For the implementation of the 40 MHz synchroscan, I requested the reduced amplitude sweep, such that a larger fraction of the sweep occurred on the screen at the cost of time axis linearity. I also developed the 2D-1D fiber array design with a 12.5 ns to better match the synchroscan scheme. I developed the reference fiber concept with Dr. Qiyin Fang, and I implemented it. Measurements with the reference fiber were performed by me and Nehad Hirmiz, and analyzed by me. I developed the barrel distortion correction, which was later improved upon by Nehad Hirmiz. I developed the linearization algorithm for the streak camera's time axis. Experiments to measure optical crosstalk, fluorescence lifetime for different schemes, and real-time drift correction were designed by me, and performed by Nehad Hirmiz. Nehad Hirmiz performed the analysis for these experiments.

References

[1] S. M. Paul, D. S. Mytelka, C. T. Dunwiddie, C. C. Persinger, B. H. Munos, S. R. Lindborg and A. L. Schacht, "How to improve R&D productivity: the pharmaceutical industry's grand challenge," *Nature Reviews Drug Discovery,* vol. 9, no. 3, pp. 203-214, 2010.

[2] M. Hay, D. W. Thomas, J. L. Craighead, C. Economides and J. Rosenthal, "Clinical development success rates for investigational drugs," *Nature Biotechnology,* vol. 32, no. 1, pp. 40-51, 2014.

[3] Tufts University, "Cost to develop and win marketing approval for a new drug is $2.6 billion," 18 November 2014. [Online]. Available: http://csdd.tufts.edu/news/complete_story/pr_tufts_csdd_2014_cost_study. [Accessed 22 September 2016].

[4] I. M. Ghobrial, T. E. Witzig and A. A. Adjei, "Targeting apoptosis pathways in cancer therapy," *CA: Cancer Journal for Clinicians,* vol. 55, no. 3, pp. 178-194, 2005.

[5] H. Brahmbhatt, S. Oppermann, E. Osterlund, B. Leber and D. W. Andrews, "Molecular pathways: leveraging the BCL-2 interactome to kill cancer cells

- mitochondrial outer membrane permeabilization and beyond," *Clinical Cancer Research,* vol. 21, no. 12, pp. 2671-2676, 2015.

[6] C. B. Thompson, "Apoptosis in the pathogenesis and treatment of disease," *Science,* vol. 267, no. 5203, pp. 1456-1462, 1995.

[7] D. E. Scott, A. R. Bayly, C. Abell and J. Skidmore, "Small molecules, big targets: drug discovery faces the protein-protein interaction challenge," *Nature Reviews Drug Discovery,* vol. 15, no. 8, pp. 533-550, 2016.

[8] H. P. Erickson, "Size and shape of protein molecules at the nanometer level determined by sedimentation, gel filtration, and electron microscopy," *Biological Procedures Online,* vol. 11, no. 1, pp. 32-51, 2009.

[9] G.-J. Kremers, D. W. Piston and M. W. Davidson, "Microscopy U: Basics of FRET Microscopy," Nikon Instruments, 2016. [Online]. Available: https://www.microscopyu.com/applications/fret/basics-of-fret-microscopy. [Accessed 17 January 2017].

[10] H. C. Ishikawa-Ankerhold, R. Ankerhold and G. P. C. Drummen, "Advanced fluorescence microscopy techniques - FRAP, FLIP, FLAP, FRET and FLIM," *Molecules,* vol. 17, no. 4, pp. 4047-4132, 2012.

[11] J. R. Lakowicz, "Energy Transfer," in *Principles of Fluorescence Spectroscopy*, New York, Springer, 2006, pp. 443-475.

[12] Y. Sun, C. Rombola, V. Jyothikumar and A. Periasamy, "Förster resonance energy transfer microscopy and spectroscopy for localizing protein-protein interactions in living cells," *Cytometry Part A,* vol. 83, no. 9, pp. 780-793, 2013.

[13] D. W. Piston and G.-J. Kremers, "Fluorescent protein FRET: the good, the bad and the ugly," *Trends in Biochemical Sciences,* vol. 32, no. 9, pp. 407-414, 2007.

[14] J. Lakowicz, "Time-Domain Lifetime Measurements," in *Principles of Fluorescence Spectroscopy,* New York, Springer, 2006, pp. 97-155.

[15] F. Zanella, J. B. Lorens and W. Link, "High content screening: seeing is believing," *Trends in Biotechnology,* vol. 28, no. 5, pp. 237-245, 2010.

[16] W. F. An and N. Tolliday, "Cell-based assays for high-throughput screening," *Molecular Biotechnology,* vol. 45, no. 2, pp. 180-186, 2010.

[17] E. Wang, C. M. Babbey and K. W. Dunn, "Performance comparison between the high speed Yokogawa spinning disc confocal system and single-point scanning confocal systems," *Journal of Microscopy,* vol. 218, pp. 148-159, 2005.

[18] V. Magidson and A. Khodjakov, "Circumventing photodamage in live cell microscopy," *Methods in Cell Biology,* vol. 114, pp. 545-560, 2013.

[19] S. E. Webb, Y. Gu, S. Lévêque-Fort, J. Siegel, M. J. Cole, K. Dowling, R. Jones and P. M. French, "A wide-field time-domain fluorescence lifetime imaging microscope with optical sectioning," *Review of Scientific Instruments,* vol. 73, no. 4, p. 1898, 2002.

[20] D. Toomre and J. Pawley, "Disk-scanning confocal microsopy live cell imaging: probing the future," in *Biological Confocal Microscopy,* New York, USA, Springer, 2006, pp. 223-238.

[21] D. K. Toomre, M. F. Langhorst and M. W. Davidson, "Introduction to Spinning Disk Confocal Microscopy," [Online]. Available: http://zeiss-campus.magnet.fsu.edu/articles/spinningdisk/introduction.html. [Accessed 18 January 2017].

[22] L. Li, Q. Zhou, T. C. Voss, K. L. Quick and D. V. LaBarbera, "High-throughput imaging: Focusing in on drug discovery in 3D," *Methods,* vol. 96, no. 6, pp. 97-102, 2016.

[23] D. M. Grant, W. Zhang, E. J. McGhee, T. D. Bunney, C. B. Talbot, S. Kumar, I. Munro, C. Dunsby, M. A. A. Neil, M. Katan and P. M. W. French, "Multiplexed FRET to image multiple signaling events in live cells," *Biophysical Journal,* vol. 95, pp. L69-L71, 2008.

[24] W. Becker, "Fluorescence lifetime imaging - techniques and applications," *Journal of Microscopy,* vol. 247, no. 2, pp. 119-136, 2012.

[25] S. Kumar, C. Dunsby, P. A. A. De Beule, D. M. Owen, U. Anand, P. M. P. Lanigan, R. K. P. Benninger, D. M. Davis, M. A. A. Neil, P. Anand, C. Benham, A. Naylor and P. M. W. French, "Multifocal multiphoton excitation and time correlated single photon counting detection for 3-D fluorescence lifetime imaging," *Optics Express,* vol. 15, pp. 12548-12561, 2007.

[26] A. Cuccato, S. Antonioli, M. Crotti, I. Labanca, A. Gulinatti, I. Rech and M. Ghioni, "Complete and compact 32-channel system for time-correlated single-photon counting," *IEEE Photonics Journal,* vol. 5, no. 5, 2013.

[27] S. P. Poland, N. Krstajić, J. Monypenney, S. Coelho, D. Tyndall, R. J. Walker, V. Devauges, J. Richarson, N. Dutton, P. Barber, D. D.-U. Li, K. Suhling, T. Ng, R. K. Henderson and S. M. Ameer-Beg, "A high speed multifocal multiphoton fluorescence lifetime imaging microscope for live-cell FRET imaging," *Biomedical Optics Express,* vol. 6, no. 2, p. 277, 2015.

[28] R. V. Krishnan, H. Saitoh, H. Terada, V. E. Centonze and B. Herman, "Development of a multiphoton fluorescence lifetime imaging microscopy system using a streak camera," *Review of Scientific Instruments,* vol. 74, no. 5, pp. 2714-2721, 2003.

Chapter 2

Applying confocal fluorescence lifetime imaging microscopy to high-content screening

The cost of drug discovery has been increasing due to increased safety regulations and notable late-stage failures. The ability to correctly identify promising drug leads at an early stage is critical in improving this process. This requires a screening method that provides both a suitable environment to mimic *in vivo* conditions and biochemical relevance to determine the mechanism of action behind a drug lead. Imaging protein-protein interactions (PPIs) is attractive for this purpose, and this can best be accomplished applying fluorescence lifetime imaging microscopy (FLIM) to a high-content screening (HCS) microscope. This chapter presents the motivation for the development of a multi-point confocal FLIM microscope and the requirements for the prototype system. The challenges facing the pharmaceutical industry in developing novel drugs are outlined in Section 2.1. The importance of monitoring PPIs is discussed in Section 2.2, and Förster resonant energy transfer (FRET) is introduced as a method of monitoring them in Section 2.3. The approaches to measuring FLIM FRET are discussed in Section 2.4. Section 2.5 describes the requirements of a FLIM system for the application of HCS FRET. Existing commercial confocal microscopes are outlined in Section 2.6, along with alternative multi-point scanners. A discussion of the presented options is provided in Section 2.7 to justify the selections for the system.

2.1. The current state of drug discovery

The drug discovery pipeline refers to the entire process by which new drug leads are found, optimized, tested and approved. Unfortunately, this pipeline has become significantly longer and more expensive in recent years, with the successful development of a drug spanning over a decade and exceeding 2.6 billion dollars in cost [1]. There are many causes associated with this trend, including an exhaustion of the easy targets [2] and more stringent clinical phase testing following the emergence of life-threatening side effects with established drugs [3]. The expiration of existing patents and expected legislation for drug price control for the large aging population has led the industry to a point of desperation [3]. Counterintuitively, the trend has been to target specialty medications with lower likelihood of approval and smaller treatment population, as this approach leads to higher profits and slower competition [2].

Behind these reactionary changes to drug development portfolios, there is clearly a strong requirement for early phase testing that can better identify successful leads. As a whole, only 10% of drug leads that reach clinical trials succeed on all phases and become approved, and many of the failures occur at very late phases – often after years of testing [4]. As is shown in Figure 2-1, clinical trials also represent half of the average 14-year drug development time, and more than 90% of the $260 million drug development cost [5]. The ability to better recognize these failures at the lead identification phase would greatly improve the efficiency and cost of the drug discovery process.

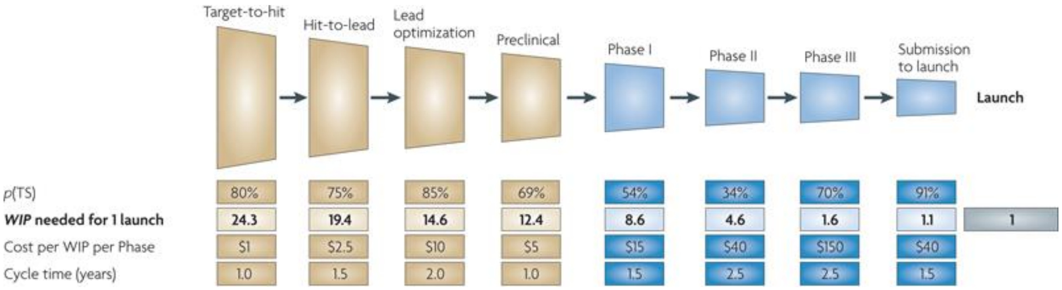

Figure 2-1: The drug development pipeline, with each stage denoting the average probability of success (p(TS)), cost per work-in-progress (WIP), and cycle time. It is also noted the number of WIP at a given stage in order to result in an average of one successful drug approval. Source [5].

Phenotypic screening represents one major drug screening paradigm for lead identification. In phenotypic screening, a library of drug leads is tested on biological samples to see which drugs might result in desired treatment effects – these outward signs of treatment being denoted as “phenotypes”. Traditionally, this was a very laborious approach, since the phenotypes had to be inspected visually [6]. Over the past decades, significant advances have been made to improve the information and validity of drug screening: from cell-based assays that better mimic the *in vivo* environment, to high-content screening (HCS) where the cells in each microwell are imaged to provide a wealth of localized and spatial information, along with increasing computational power to better analyze complex phenotypes [7]. An HCS phenotype can now be any cellular feature that is determined by analyzing readout images. Common phenotypes involve cell viability and morphology, as well as the size and shape of organelles and other cellular components [8]. By tagging proteins of interest with fluorescent proteins, it is also possible to determine the location and expression levels of these proteins. All of these phenotypes can provide evidence of how a drug lead has effected a cell sample, though they tend to be endpoints. In other words, they do not explicitly show which target the drug acts upon, and therefore do not provide a molecular mechanism of action behind the drug's function [9]. Since the mechanism is often unknown, it also makes it difficult for a drug lead to be further optimized. Discovering the biological target in a phenotypic screen – also known as "target deconvolution" – is considered the rate-limiting step of screening [10].

In contrast, target-directed screening measures the effect of drug leads on purified target proteins. This was considered a revolution for the pharmaceutical industry in the 1980s, as this allowed for explicit results for the interaction and modulation of drug leads against targets [9]. With target-directed screening, there is no question as to the target of the drug, which makes the drug's validation and optimization significantly easier. This may lead to very good knowledge of the drug's interaction, but the interaction is less meaningful when it occurs outside of a live cell environment [9]. In reality, it is the drug binding that is being optimized in target-based screening, and not the biological effect. Despite the widespread implementation of target-based screening techniques, drug candidates continued to fail at later testing stages along the drug discovery pipeline [9]. Target-based screening also tends to cast a small net, since it inherently excludes drugs that may create a desirable biological effect along unpredicted pathways. It is also difficult to purify full-length proteins for *in vitro* testing, which limits the range of target proteins available to target-based screening [11].

2.2. Protein-protein interactions

As phenotypic screening has advanced with technology, it has become possible to quantitatively measure phenotypes that occur closer to the level of molecular biology, blurring the lines between the two techniques. At a molecular biology level, the actions of a cell are governed by a complex network of protein-protein interactions (PPIs) known as an interactome. Human disorders are often the result of imbalances and perturbations in these cellular networks. The ability to tag proteins of interest with fluorescent proteins allows phenotypic screening to image the presence and location of these tagged proteins in the cell, providing some downstream knowledge of what cellular processes are at work. Even better though would be an HCS technique that would allow for the direct monitoring of PPIs themselves, as an indicator of which molecular pathway a drug lead is modulating. Furthermore, there is an emerging field of drug molecule design that seeks to directly act upon the proteins themselves in order to disrupt PPIs [12, 11].

One important cellular process regulated by PPI pathways, for example, is apoptosis. Apoptosis is the process of programmed cell death induced by the body to remove unwanted cells. Ideally, this process should be perfectly balanced with cell proliferation, maintaining a constant cell population. However, an imbalance of factors regulating apoptosis can lead to cancerous tumours. Similarly, overactive apoptosis signaling can cause a degenerating population of cells, which has been linked to Parkinson's disease and Human Immunodeficiency Virus (HIV) [13].

While there are many different ways in which the body can trigger the apoptosis of a cell, and there is continuous debate over the exact mechanisms involved, the final act of apoptosis involves a nuclease fragmenting the DNA in the nucleus, resulting in chromatin condensation. Caspase-dependent pathways are triggered by signals external to the cell, and ultimately lead to the activation of caspase-3 by caspase-8 or caspase-9. Caspase-3 then cleaves DNA fragmentation factor 40 (DFF-40), a nuclease that acts to break apart the DNA in the nucleus. There are also more recently discovered caspase-independent pathways, where apoptosis-inducing factor (AIF) is released from inside the mitochondria to trigger chromatin condensation [14]. A diagram of the PPI pathways involved in apoptosis is shown in Figure 2-2.

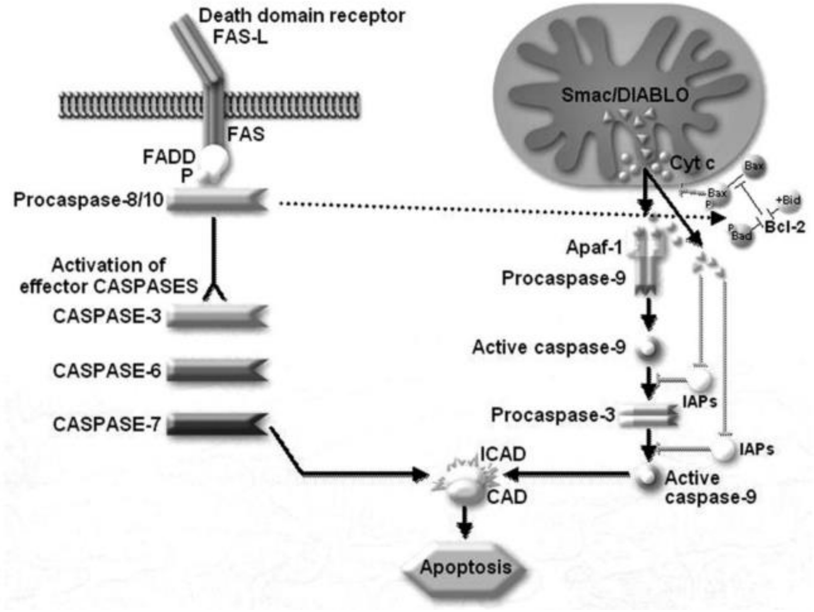

Figure 2-2: Cellular pathways towards triggering apoptosis. Source: [14].

During these processes, there are a number of intermediate proteins that can support or hinder the cascade. Bcl-2 family proteins are termed pro- or anti-apoptotic depending on how they influence the process. For instance, the BH3 component of Bax and Bak proteins create oligomers on the outer mitochondrial wall to form pores, facilitating the release of cytosol – an ingredient in the cleaving of procaspase-3. Meanwhile Bcl-2 and Bcl-xL isolate BH3, preventing it from damaging the mitochondrial wall. Beyond this, there are apoptosis inhibitors, like XIAP, that bind to caspase-3 and caspase-9, preventing them from carrying out apoptosis [14]. The balanced expression of these proteins is critical in ensuring that PPIs are occurring at the proper rate, and resulting in the proper processes through the interactome.

While being able to monitor how PPIs are modulated by a drug candidate could provide unprecedented clarity into the drug candidate's function, the scale at which these interactions occur is far below the optical diffraction limit. Cellular proteins are typically smaller than 10 nm [15], and the interaction occurs when proteins are separated by less than 10 nm as well. This is compared to the optical diffraction limit which is λ/2NA, or around 200 nm for a high NA objective (NA 1.4, λ = 500 nm). Even novel super-resolution imaging techniques, such as photoactivation localization microscopy and stimulated emission depletion microscopy, cannot typically reach the resolution range required to image these interactions [16].

2.3. Förster resonance energy transfer for monitoring PPIs

Instead of directly resolving the proteins in order to detect the PPIs, an alternative method is to measure the Förster resonance energy transfer (FRET): the non-radiative transfer of energy between an excited "donor" fluorophore and a nearby "acceptor" fluorophore. FRET only occurs at very small separations between two fluorophores. The FRET efficiency E_{FRET}, which is the quantum yield of FRET, at a given distance is provided by the relation:

$$E_{FRET} = \frac{1}{1 + \left(\frac{r}{R_0}\right)^6} \tag{2.1}$$

In this equation, r is the distance separation of the donor and acceptor fluorophores, and R_0 is the Förster distance, a fluorophore-pair specific distance corresponding to 50% FRET efficiency. Förster distances are typically less than 10 nm. A table of common FRET pairs is presented in Table 2-1.

Table 2-1: Common donor and acceptor fluorescent protein FRET pairs and their corresponding Förster distances. Source: [17]

FRET Protein Pair	Donor Excitation Peak (nm)	Acceptor Emission Peak (nm)	Förster Distance (nm)
EBFP2-mEGFP	383	507	4.8
ECFP-EYFP	440	527	4.9
Cerulean-Venus	440	528	5.4
MiCy-mKO	472	559	5.3
TFP1-mVenus	492	528	5.1
CyPet-YPet	477	530	5.1
EGFP-mCherry	507	610	5.1
Venus-mCherry	528	610	5.7
Venus-tdTomato	528	581	5.9
Venus-mPlum	528	649	5.2

In order to use FRET as an indicator for PPIs, the donor and acceptor fluorophore each need to be linked to a protein of interest. Therefore, when the two proteins of interest are interacting, they will be in close enough proximity for FRET to occur between their linked fluorophores. The modified forms of the proteins with the connected fluorophore are developed as a plasmid and introduced to the cells via transfection. It is important to consider that the PPIs being investigated are very small and abundant. Within the diffraction-limited volume being investigated by a focused spot, there is likely to be a large population of the FRET fluorophore pairs. This includes a population of proteins that are interacting (FRET occurring) and a population that are not interacting (FRET not occurring). It is important to be able to extract information about the degree of FRET occurring at each spot of the image, that is, the fraction of the population of donor fluorophores that are experiencing FRET.

2.3.1. Ratiometric FRET

There are a few indicators for measuring FRET, the most obvious of which is wavelength. If FRET does not occur, the donor fluorophore emits a photon, and the wavelength of the photon will be in the donor fluorophore's emission band. When FRET occurs, however, it will be the acceptor's fluorophore that emits a photon, and so the photon's wavelength will be in the acceptor fluorophore's emission spectrum. This process is shown in Figure 2-3. Therefore, the FRET efficiency can be solved as the ratio of signal on the acceptor channel to the combined signal. While easy to visualize, there appear to be many complications in practice. First, there will be several cases for spectral bleeding: the acceptor fluorophore could be directly excited by the excitation source, or the donor fluorophore could emit a photon that falls in the acceptor emission band. This also assumes that fluorescence and FRET are the only two possible processes by which the fluorophores can return to their ground states: other internal and external processes complicate this picture. Finally, population differences between the proteins of interest can lead to misinterpretation of the data: is the FRET efficiency low, or are there just more donor fluorophores than acceptor fluorophores in the area? Similarly, different photobleaching rates between the donor and acceptor can affect the ratios. For this reason, it is preferred to use intensity-based FRET measurement in cases where a conformational change is being monitored, so that there is always a perfect 1:1 relation between the donor and acceptor populations. In any case, while intensity-based FRET measurement is simple to collect, it requires significant calibration to properly interpret the results, which impacts the precision of the results [18, 19].

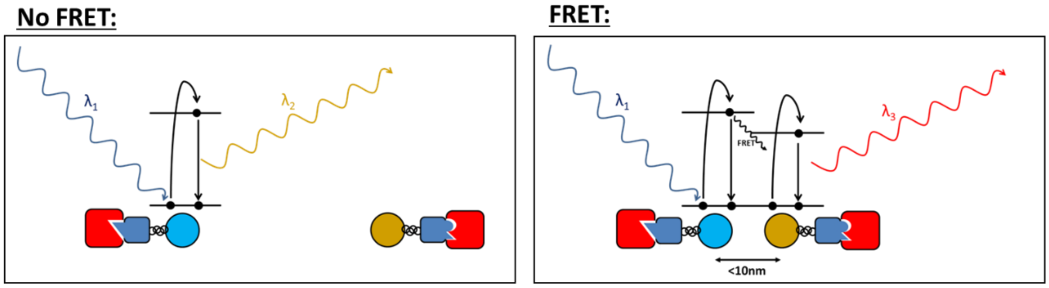

Figure 2-3: The illustrated process of FRET. No FRET: The targets are sufficiently far apart that there is no FRET occurring between the tagged fluorophores. FRET: The targets are closer, leading to the possibility of FRET being used to excite the acceptor fluorophore.

2.3.2. Polarization anisotropy FRET

Polarization anisotropy can also be used to measure FRET. The donor fluorophore is only excited by excitation light that is polarized parallel to its absorption vector. By exciting the sample with linear polarized light, only the population of fluorophores that have a shared orientation with the light polarization will be excited. In the case where there is no FRET interaction, the fluorescence will be polarized along the same axis as the excitation. However, if FRET occurs, the misalignment between the axes of the two fluorophores will result in a change in the polarization axis of the fluorescent light. It is therefore possible to determine the level of FRET by measuring the polarization of the donor fluorescence. Since only the donor fluorescence is measured, this does not share the significant correction requirements of ratiometric FRET. The nanosecond-regime fluorescence lifetime of the fluorophores also suggests that rotations and collisions of molecules will not have an impact on the measured anisotropy. Polarization anisotropy is also the only way of measuring FRET where the donor and acceptor are the same fluorophore (“homo-FRET”), since this does not result in a change in emission wavelength or fluorescence lifetime [19]. However, while the anisotropy measure is very sensitive at measuring the presence of FRET, it is not particularly good at distinguishing the degree of FRET. Another concern is maintaining polarization through each optical element of the microscope: high numerical aperture objectives in particular tend to degrade the polarization [19].

2.3.3. Lifetime FRET

FRET activity can instead be measured by fluorescence lifetime imaging microscopy (FLIM), which is regarded as the most rigorous method [18]. In this case, the acceptor's fluorescence is ignored entirely, and all that is of interest is that the acceptor fluorophore's proximity adds another possible pathway for the donor fluorophore to return to ground state. Since a new pathway is provided with FRET, excited donor fluorophores do not stay in an excited state for as long, hence a reduction in the lifetime of the fluorescence state. The primary benefit of this approach is that the presence of FRET can be measured without needing to correct for spectral bleeding and fluorophore variability. Fewer corrections lead to more precise results that are easier to interpret. One drawback to FLIM is that it typically involves higher cost measurement equipment in order to resolve the fluorescence decay with sufficient temporal resolution. Biological fluorophores commonly used as FRET pairs typically have lifetimes in the range of a few nanoseconds. Also, as the lifetime of the fluorescence decay is a direct representation of the lifetime of the fluorophore's excited state, changes in lifetime can also be caused by any other unforeseen quenching mechanisms besides FRET, including collisions, acidity, and temperature in the fluorophore's microenvironment. It is then important to carefully maintain the cellular environment in order to ensure only the desired quenching pathway (FRET in this case) is being modulated. Conversely, it can also be said that the applications of FLIM extend far beyond FRET, and as long as care is taken in setting up the experiment, different parameters such as ion concentrations and cellular metabolic state can be determined in a FLIM experiment.

2.4. Time-resolved approaches to FLIM FRET

For the case of FLIM FRET, the FRET efficiency can be determined based on the ratio of the quenched and unquenched lifetime:

$$E_{FRET} = 1 - \frac{\tau_{DA}}{\tau_D} \tag{2.2}$$

where τ_D is the fluorescence lifetime of the donor fluorophore alone, and τ_{DA} is the fluorescence lifetime of the donor fluorophore in the presence of the acceptor fluorophore.

In a fluorescence lifetime image, each pixel of the image is false coloured to represent the fluorescence lifetime. Depending on what property the fluorescence lifetime is a surrogate for, the false colour legend can be converted to more meaningful units (e.g. ion concentration [20], pH [21], FRET efficiency [22]). While the average fluorescence lifetime at each point in the sample is sufficient information for many FLIM applications, this is not the case for FLIM-FRET. As discussed earlier, there are two discrete populations of donor fluorophores in each sampled volume: unbound and bound. If the FRET-positive fluorophores have a quenched lifetime τ_{DA} and the FRET-negative fluorophores have an unquenched lifetime τ_D, then the resulting signal would take the form of a biexponential decay s(t):

$$s(t) = N_D \exp\left(\frac{t}{\tau_D}\right) + N_{DA} \exp\left(\frac{t}{\tau_{DA}}\right) \tag{2.3}$$

where t is time after excitation, and N_0 and N_{FRET} are proportional to the populations of unquenched and quenched fluorophores respectively [23]. The addition of a second exponential term makes the process of lifetime fitting more difficult.

There are other factors that can complicate the fluorescence signal. A common problem is the exponential decay model relies on the assumption that the excitation pulse is sufficiently narrow to be considered an ideal pulse. This requirement depends on the fluorescence lifetimes of interest, but when the pulse width cannot be ignored, the impulse response function of the excitation pulse needs to be factored into the fitting process, making the calculation more intensive and less accurate. Pulsed diode lasers typically have a pulse width of around 50-100 ps [24]. While shorter pulses are possible (e.g. Ti:Sapphire and fiber lasers), pulse diode lasers are significantly less expensive and are available in a larger variety of wavelengths. Finally, there can be other unforeseen and unavoidable sources of fluorescence in the sample, known as autofluorescence. Due to these considerations, it is important that the fluorescence signals are collected with high temporal resolution in order to be able to accurately separate out the contributions and determine the actual FRET efficiency.

There are a host of methods for measuring a fluorescence lifetime signal. These methods are summarized in Table 2-2 along with typical values for specifications.

Table 2-2: Comparison of FLIM acquisition methods, listed with representative detector options and pertinent technical specifications. "Array" refers to the largest commercially available detector array for multiplexing purposes. "WF" indicates widefield technique. "Slit" refers to the streak camera's entrance slit being available for multiplexing.

Acquisition	Detector	PDE @ 550nm	MCR	Temporal resolution	Array	Ref
TCSPC	PMT, SPAD	50%	2 Mcps*	50ps	16	[25]
Gated	ICCD	20%	N/A	300 ps	WF	[26, 27]
Digitizer	PMT, APD	50%	N/A	400 ps	2	[28]
Streak Camera	Photocathode	5%	N/A	< 50 ps	slit	[29]

* MCR is maximum collection rate, based on 5% of 40 MHz laser repetition rate to prevent pulse pileup

2.4.1. Time-correlated single-photon counting

Time-correlated single-photon counting (TCSPC) has been established as the gold standard in time-resolved imaging [30]. TCSPC uses a photomultiplier tube (PMT) or single-photon avalanche diode (SPAD) as a detector to receive an amplified pulse signal upon arrival of a single photon count. While the pulse itself has a width in nanoseconds, the timing jitter of the pulse is in the range of 50 ps, depending on the detector and excitation source. By ensuring that only one photon count is expected to arrive within a single excitation period, it is possible to very precisely measure the arrival time of the photon count, and achieve temporal resolution limited either by the timing jitter or by the resolution of the timing circuitry. After many photon counts, the arrival times can be arranged into a histogram to create the fluorescence lifetime decay waveform.

TCSPC excels in precision, and since it is a discrete photon detection technique, there is no analog noise in the measurement. Sources of detector-specific noise are limited to dark counts and afterpulsing. The primary drawback to TCSPC is that it is an inherently slow technique. If more than one photon count arrives within the same period, only the first photon count is detected and subsequent photon counts are lost. By systematically ignoring photons that arrive later in time, the resulting photon arrival histogram is artificially distorted to show a shorter than expected lifetime – an effect called pulse pile-up distortion. In order to prevent distortion, the photon count collection rate must be kept very small compared to the repetition rate. A typical rule is to ensure that the collection rate never exceeds 5% of the repetition rate. Therefore, if a repetition rate of 40 MHz is used, the collection rate must be kept below 2 Mcps.

The limited collection rate sets a strict bottleneck on the acquisition speed of a FLIM image while using a TCSPC approach. If 10,000 counts are required in a histogram in order to sufficiently estimate a biexponential decay [31], then each scan position will require at least 5 ms to acquire these counts with a 2 Mcps collection rate. It would then take over 5 minutes to acquire a 512 x 512 FLIM image. While low laser powers must be used for TCSPC in order to avoid pulse pileup, it is also beneficial to use low laser powers on live cells in order to prevent photobleaching and phototoxicity [32].

2.4.2. Time-gated acquisition

Time-gated acquisition is a method of time-resolved imaging that typically uses an intensified CCD (ICCD). A micro-channel plate (MCP) image intensifier is placed in front of the camera sensor in order to selectively amplify (or gate) incident photons. Depending on the model of ICCD, the MCP can be gated to a time window as short as 300 ps, and collected at high megahertz repetition rates [26]. In order to measure a fluorescence lifetime, signal from the fluorescence decay must be collected at different time windows relative to the laser trigger. For instance, two windows are sufficient to estimate the lifetime of a single exponential fluorescence decay.

The primary benefit to the time-gated approach is acquisition speed. First, it is a widefield approach where the fluorescence decays for every part of the image can be acquired simultaneously. It also does not have any excitation level limitation, and so signal can be acquired more quickly by increasing the laser power – as long as it is below the photobleaching limit. An entire FLIM image can be acquired with the readout of N frames, where N is the number of time windows required to discern the components in a given fluorescence decay. The widefield approach can also be made confocal by attaching a spinning disk confocal unit in front of the ICCD [33]. A confocal acquisition, where the out-of-focus emission light is rejected via pinholes, is essential for optically sectioning a live cell sample. It is even more important in FLIM, where out-of-focus fluorophores could also contribute their own lifetime components, further complicating the lifetime fitting.

There are also a number of practical drawbacks. First, the 300 ps time resolution is not great, and not sufficient for a lifetime analysis that requires unmixing lifetime components and deconvolving the impulse response function. The technique is also very wasteful, since it rejects photons that arrive outside of the current narrow time window. Therefore, its photodetection efficiency is much worse than simply the quantum efficiency of the MCP detector. Since fluorophores can only be excited a limited number of times before they are permanently photobleached, efficient collection of photons is critical to live cell FLIM. Finally, the ICCD is an analog approach, and therefore its signal is degraded by the readout noise of the sensor and the multiplicative noise of the intensifier. More signal is then required in order to achieve a suitable SNR than would be for TCSPC.

2.4.3. High speed digitizer

A high-speed digitizer can also be used to collect a time-resolved signal from a point detector. This acquisition method simply digitizes the detector signal and reads it into a computer. This approach has a number of advantages beyond its simplicity and cost. There is no inherent limit to photon collection rates as with TCSPC, and no segment of the signal is rejected as with time-gated acquisition.

High-end digitizers are able to acquire at rates of up to 10 GS/s with a bandwidth of 2.5 GHz [28]. This corresponding roughly to a temporal resolution of 400 ps, which is a bit coarse for the multi-exponential FLIM application. The digitizers can also work with real-time averaging, where the time-resolved signal is accumulated from many repetitions [28]. Digitizers acquire an analog signal, which does mean that their signal can be noisier from analog noise sources compared to TCSPC. The main drawback for digitizer acquisition is that they do not offer a significant level of multiplexing: when digitizers contain multiple channels, the multiplexing capability comes at the cost of sampling rate.

2.4.4. Streak camera

The streak camera is a time-resolving instrument that is particularly unique to the alternatives explored above. Instead of achieving its temporal resolution by high-speed electronics or pulse centroiding, the streak camera converts the temporal dimension to a spatial one that can easily be captured by a readout camera. At the entrance slit of the streak camera, a photocathode produces electrons in response to incident photons, and the electrons are then accelerated through a vacuum tube. A time-varying electric field is applied perpendicular to the electrons path, veering them to the left or right depending on the time of their arrival. The axis on which acts the electric field acts then effectively becomes the temporal axis of the readout. The remaining axis (up and down) can still be spatially resolved, and can then be used to accommodate either a multitude of parallel channels or another measurement dimension. For example, a streak camera can be used in series with a spectrometer to produce a two-dimensional spectral-temporal measurement. At the end of the vacuum tube, the electrons are multiplied through an MCP, converted back to photons through a phosphor screen, and then measured by a scientific camera. This process is shown in Figure 2-4.

Streak cameras have a number of attractive features. First, depending on the parameters for the time-varying electric field, it is possible to achieve sub-picosecond temporal resolution – far lower than the limits of TCSPC. It also has no inherent limit to the signal level that it can collect, unlike the TCSPC pulse-pileup limit. It can collect the signal in its entirety, unlike a gated approach that can only collect signal that falls within its gated window. It can even achieve some level of photon-counting ability, given that the bright spots associated with each incident photon are sufficiently separated. Finally, its entrance slit can be filled with a large array of independent channels, allowing it to accommodate a multi-point scanning approach.

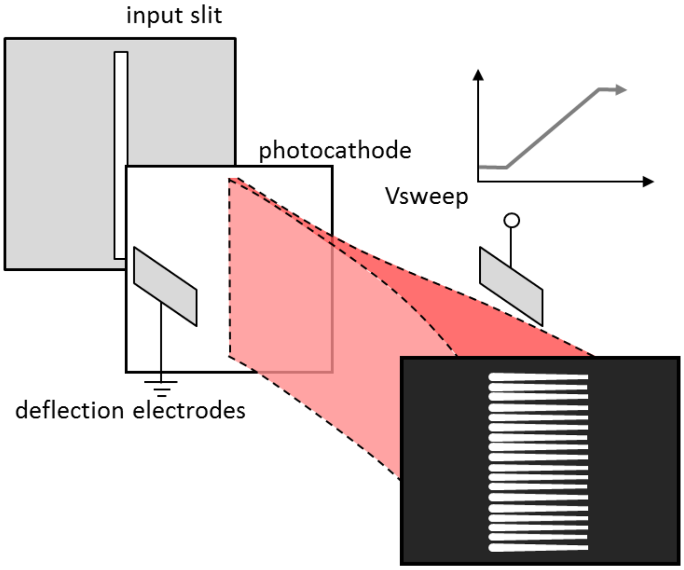

Figure 2-4: Working principle of the streak camera. Phosphor screen shows the result of the streak camera's input slit being fit with a 1D array of discrete channels.

The largest drawback to the streak camera is due to its exceptionally poor photodetection efficiency. The combination of the photocathode's quantum efficiency [34] and its isotropic emission [35] mean that the fraction of photons that result in an electron being released *and* travelling in the forward direction is quite low. There are also other small losses along the electrons path, such as the extraction mesh and the MCP's quantum efficiency, which only reduce this further. In the end, the photodetection of the streak camera is approximated 5% [29]. This results in the tragic conclusion that, while the streak camera can handle a much higher photon flux than TCSPC, its low photodetection efficiency requires that a much higher photon flux be used in order to achieve similar signal levels. This is at the cost of the sample, as well, since the higher required excitation level or extended excitation time will lead to photodamage more quickly. This is combined with the fact that it is typically run an analog device, in which there is significant multiplicative noise to further reduce the quality of the received signal.

There are other aspects where the streak camera requires compromises, such as its repetition rate. The streak camera's time-varying electric field typically takes the form of a ramp voltage, resulting in a linear temporal axis. The ideal ramp voltage cannot be achieved beyond a repetition rate of a few megahertz. In order to achieve a repetition rate of 40 MHz – considered ideal for the fluorescence lifetimes of most biological fluorophores – it can only provide a sinusoidal waveform, and therefore a non-linear time axis. Typically, the sinusoidal deflection is amplified such that only the linear sections of the sinusoidal waveform are used, effectively resulting in a ramp. This, however, comes at the cost of a reduced time window.

Finally, the streak camera practically requires multiplexing in order to do a decently fast scan of a sample. The acquisition speed of the streak camera is limited by its readout camera. While scientific CMOS (sCMOS) cameras have made great strides in terms of providing both high quality images and high speed readouts, the data transfer rate is still limited to hundreds of frames per second. Since a 512 x 512 FLIM image contains 262,144 pixels, it would take a 100 fps camera 44 minutes to acquire every pixel in the image. Meanwhile, if 100 channels are used in each frame, then the entire image can be collected in 26 seconds. While future developments could lead to higher frame-rate cameras with suitably high image quality, the frame rate will ultimately be limited by the response time of the phosphor screen on the readout, which is on the order of 3 ms [36, 34].

2.4.5. Frequency domain FLIM

The methods outlined above are examples of time-domain lifetime measurement, but there are also methods for performing frequency-domain FLIM (FD-FLIM). In its simplest form, FD FLIM uses a modulated light source instead of a pulsed light source. The modulation depth and phase of the fluorescence signal are both impacted by the lifetime of the fluorophore. Therefore, the fluorescence lifetime can be estimated by measuring the degree of demodulation, the phase shift, or both. The response of the fluorophore acts like a low-pass filter: the longer the fluorescence lifetime, the larger the phase shift and the larger the degree of demodulation. At its limit, the output signal is full demodulated and reaches a phase shift of 90°.

The most common implementation of FD FLIM is to use an ICCD much in the same way as the time-gated acquisition of time-domain FLIM. Instead of applying discrete gates, the intensifier is modulated at the same frequency as the excitation source, also called “homodyne detection”. The largest signal is measured when the modulation of the intensifier is phase-matched to the fluorescence signal. By iterating the phase of the intensifier’s modulation, the phase shift and degree of demodulation of the signal can be determined, and thus the fluorescence lifetime can be estimated.

Alternatively, a point-scanning approach can be implemented with “heterodyne detection”, where the point detector is modulated at a different frequency from the excitation source. The resulting signal collected by the digitizer would be a sinusoidal signal whose frequency is the difference between modulation frequencies of the excitation source and detector. In the output signal, the phase delay and degree of demodulation are preserved, and can still then be used to measure the fluorescence lifetime. The heterodyne detection scheme has the advantage of being able to very quickly collect the sinusoidal waveform without needing to iterate the phase. Point source detectors are also capable of higher modulation frequencies, making them more suitable for measuring very short fluorescence lifetimes. Modulated ICCDs, however, are able to acquire a widefield image with each frame, and can quickly create an average lifetime image in 2 frames with 90° phase separation.

FD FLIM acquisition can be achieved with a significant reduction in system complexity: pulsed excitation sources can be replaced with frequency-modulated excitation sources, and the detector does not need to have sub-nanosecond gating or resolution. It is also scalable over a very large range of fluorescence lifetimes by changing the modulation frequency.

FD FLIM has the inherent problem that the frequency domain results are harder to interpret than the time-domain decay. Factors such as background noise and unwanted fluorescence components affect the signal less intuitively and are more difficult to tease out. In the case of measuring FRET, where two components of the lifetime are present, a single measurement of the fluorescence lifetime is insufficient. Instead, in order to separate out the lifetime components and their fractions, multiple acquisitions at different modulation frequencies are required. FD FLIM has also been found to use each photon less efficiently than TD FLIM. Sinusoidal excitation in particular has also been determined to be very inefficient for measuring fluorescence lifetime [37, 38]. However, if pulsed lasers (equivalent to a sum of harmonic frequencies) and high temporal resolution detectors are used, the cost and complexity advantages of FD FLIM are quickly diminished.

It is worth noting that, while FD FLIM typically uses modulated sources and detectors, a frequency-domain analysis can be applied to time-domain data (e.g. TCSPC). In fact, commercial TCSPC systems have begun to use the frequency domain phasor approach [39, 40].

2.5. HCS FLIM requirements

In order for FLIM to be a useful technique in an HCS environment, it needs to be able to achieve certain benchmarks.

1. Speed: One image should take one second to acquire
2. Gentle: Low excitation intensity in order to reduce phototoxicity
3. Spatial resolution: Ability to resolve submicron cellular features
4. Optical sectioning: Ability to resolve an optical section through center of cells
5. Field-of-view: Greater than 100 μm x 100 μm
6. Modular design: Works as an added module to existing microscope platforms
7. Temporal resolution: Less than 100 ps in order to work with complex decays

The acquisition speed requirement is essential in order to make the imaging modality attractive for HCS applications. A typical HCS microscope images 100,000 samples per day, which works out to roughly one sample image required every second [41].

The requirement of gentle imaging sets a limit on the excitation intensity on the sample. There are two reasons for this. First, the rate of photobleaching, where a fluorophore becomes irreversibly damaged and is no longer able to fluoresce, increases with higher laser irradiance [42]. This is a problem from a photon budget perspective, since the number of photons that can be extracted from a cell sample is very limited. The faster rate of photobleaching limits the total number of emitted photons that can be extracted from the sample, meaning there might not be enough photons collected for meaningful lifetime analysis. Furthermore, there is also the concern of photodamage to the cells at higher excitation intensities [43]. If the excitation light is causing toxic effects to the cells, the data collected is not reflective of a healthy cellular response, which introduces artifacts (e.g. changes in fluorescence lifetime).

The solution must also be confocal in order to achieve the optical sectioning through the center of the cells, such that the organelles are in sharp focus. Confocal imaging is especially important in the case of FLIM, since the out-of-focus light being rejected by the confocal pinhole would also infiltrate the time-resolved fluorescence signals with out-of-focus contributions [44].

There is an immediate dilemma early on in the requirements, where high-speed acquisition is needed alongside gentle laser levels. For a confocal approach, increasing the laser power is a sure way to improve the collected signal and hence be able to perform a sample scan more quickly. Widefield is less damaging on a sample, since the excitation light per unit area of the sample is kept low. It is essential, however, that a confocal method is used, since widefield imaging is unable to meet the required spatial resolution and optical sectioning ability. The time-gated cameras are also unable to reach the required temporal resolution. Another way to reduce the local laser power with a confocal approach is to multiplex the process with multiple isolated foci scanning different sections of the sample at any given point in time. It is clear that, in a multiplexed scheme of N foci each supplying an ideal laser power, the scan could be completed N times as quickly as a single focal point at the same laser power.

The reasons for the temporal resolution requirements of the system have already been described as necessary for measuring the complex bi-exponential fluorescence response. This limits the time-resolved detector options to two – TCSPC and the streak camera – since gated and sampling techniques do not have sufficient temporal resolution. In the context of a multiplexed solution, using a large number of foci on the sample, the slit of the streak camera makes it the best candidate for achieving high-throughput FLIM for HCS.

It is worth noting that there have been recent developments in SPAD that have allowed for large SPAD arrays of over 1000 units to be manufactured on a chip [45]. This is certainly an area of interest for the project, and their suitability to the project will be explored in Chapter 5.

2.6. Existing commercial platforms

The most common implementation of a multi-point confocal solution is the spinning disk confocal module, also known as the Nipkow disk. A Nipkow disk is patterned with an arrangement of pinholes in nested spirals outward from the center of the disk. Each pinhole on the disk acts as an independent confocal pinhole: excitation light incident on the disk generates excitation foci at each pinhole, and returning emission light will be transmitted through the same pinhole in order to remove out-of-focus light. When the disk is spun even one twelfth of a revolution, the pinholes will have collectively covered every point in the field of view, generating a full confocal image of the sample on the imager. The disk is typically rotated at a speed of up to [46] , and while the pinholes are constantly moving, they are effectively stationary for the duration of the excitation-emission process. Traditionally, a significant drawback of spinning disk confocal was the inefficiency with which the excitation light was used, since all excitation light that did not reach a pinhole was rejected. This problem was solved with the Yokogawa CSU10 module, which uses a corresponding microlens array disk to focus excitation light into the pinhole array disk. This greatly improves the excitation light throughput from 4% to 40% [47]. Today, there are very few spinning disk confocal modules that have not implemented the double-disk design, and so the light efficiency drawback of spinning disk is a relic of the past.

2.6.1. HCS platforms

A list of major HCS platforms with confocal capabilities is provided in Table 2-3. The majority of commercial HCS platforms use spinning disk confocal arrangements in order to achieve high-speed confocal imaging, and with good reason. Spinning disk confocal is able to achieve high-speed and gentle excitation with its multi-beam arrangement while achieving confocal performance with sufficient optical sectioning for thin samples. The latest evolution of the spinning disk scanner, the Yokogawa CSU-W1, is capable of imaging a 500 μm field-of-view using a 40x objective [48] with a 2048 x 2048 pixel readout at 200 frames per second – fluorescence levels permitting. It is also inherently modular, and typically connects to a side port or bottom port of a commercial inverted microscope. The main drawback remains the inability to perform time-resolved imaging with the required precision for FLIM FRET measurement. Spinning disk systems cannot perform any kind of descanning, and so the resulting image is painted across an array imager. These platforms are still amenable to time-gated imaging, and the Perkin Elmer Opera once included the option of a gated CCD camera for FLIM [49], the latest Opera Phenix platform has removed the capability [50].

Besides spinning disk solutions, GE Healthcare's IN Cell Analyzer 6000 uses a line scan to achieve some level of confocality [51]. Instead of descanning to a line sensor, the line is scanned across an sCMOS area sensor [52]. The sCMOS camera uses a rolling shutter setup where only a small number of rows of pixels are able to collect light at any given time. This creates a virtual confocal slit on the sensor, which can be synchronized with the position of the detected fluorescent line. Since an imaging sensor is used, this method is similarly limited to intensity fluorescence measurements rather than time-resolved.

Table 2-3: List of confocal HCS platforms, based on those listed in [52] and revised with the latest commercial systems and additional information found on company websites.

HCS Platforms					
Maker	Instrument	Confocal	Detector	FLIM	Ref
BD Biosciences	BD Pathway 855	SD	CCD	N/A	[53]
GE Healthcare	IN Cell Analyzer 6000	LS	sCMOS	N/A	[51]
Molecular Devices	ImageXpress Micro Confocal	SD	sCMOS	N/A	[54]
Perkin Elmer	Opera Phenix	SD	sCMOS	N/A	[50]
Thermo Fisher	ArrayScan XTI	SD	CCD	N/A	[55]
TTP Labtech	Acumen Cellista	SP	PMT	N/A	[56]
Yokogawa	CellVoyager CV7000S	SD	sCMOS	N/A	[57]

2.6.2. Alternative multi-point scanners

There are a few multi-point confocal scanners available that do not employ a spinning disk. These are of special interest to a FLIM application, as they are still able to descan the emission light to a static array of discrete detectors. These are outlined in Table 2-4.

Table 2-4: List of alternative (non-spinning-disk-based) multi-point scanners.

Alternative Multi-Point Scanners					
Maker	Instrument	Confocal	Detector	FLIM	Ref
Bruker	Opterra II	1D array	CCD	N/A	[58]
LaVision BioTec	TriM Scope II	1D array	sCMOS	x16	[59]
Visitech	VT-Infinity3	2D array	CCD	N/A	[60]

Bruker Opterra II

The Bruker Opterra II provides a selection of confocal apertures: a range of width of slits and diameter of pinholes in a 1D array. The line of excitation is swept across the sample using a galvo head, while the returning emission light is descanned and transmitted through a corresponding pinhole array or slit aperture. The back face of the galvo is used to rescan emission light across a CCD sensor. In the case where a pinhole array is selected, a piezo scanner is used before the entrance of the microscope and before the camera in order to scan the interstitial space between foci. This is shown in Figure 2-5.

There are a few advantages with the Opterra II compared to spinning disk. First, there is the potential for descanned emission spots. Bruker has chosen to rescan onto a CCD imager by default, which makes sense for confocal intensity imaging, but it would be very easy to adapt the design by placing a discrete array detector soon after the emission pinhole array. Next, the Opterra II's foci array is one-dimensional which means that there is significantly less optical crosstalk from out-of-focus light going through adjacent pinholes. The immediate drawback to this is that a 1D arrangement cannot achieve the same degree of multiplexing as a 2D arrangement: while a spinning disk patterning uses over 1000 pinholes in the field-of-view, the Opterra is capable of only 32 pinholes in its line arrangement.

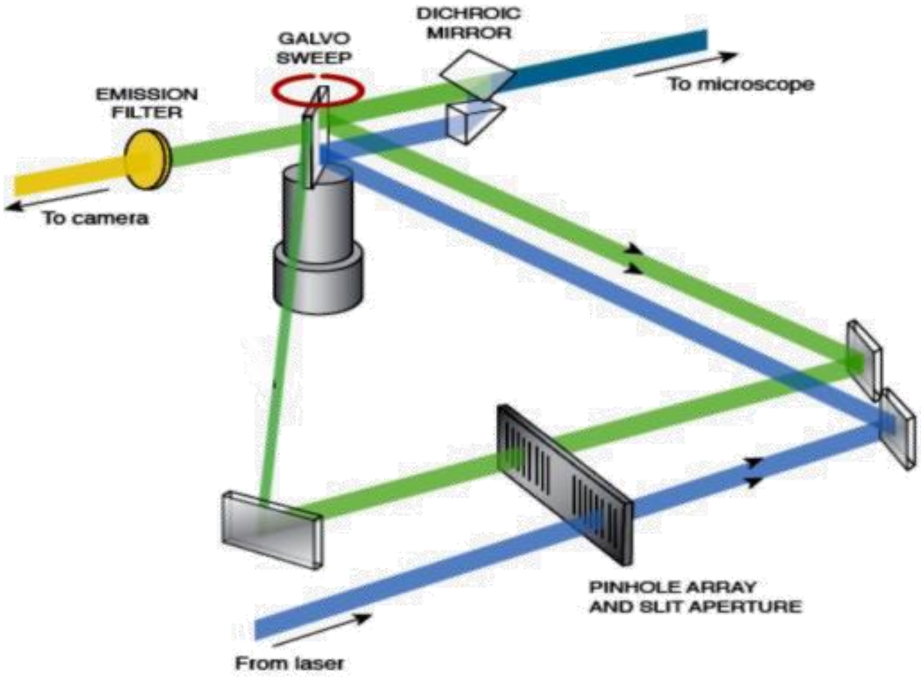

Figure 2-5: Light path of the Bruker Opterra [63].

LaVision BioTec TriM Scope II

The LaVision BioTec TriM Scope II is another multi-point scanner, capable of generating a line of up to 64 excitation foci through beam splitting, shown in Figure 2-6. The TriM Scope II is used for multiphoton microscopy, so there is no return path through a pinhole array, and the resulting image is scanned across an image sensor without descanning. Similar to the Opterra II, the TriM Scope II is limited by how many foci it can support along a single 1D axis. The crosstalk advantage of a 1D array is also not significant in the case of multiphoton microscopy, where out-of-plane multiphoton excitation is minimal.

A unique feature of the TriM Scope II is the option of a FLIM module: a 16-channel PMT array with matching TCSPC array. The PMT array features 16 rectangular detectors of 0.8 x 16 mm^2 active area, with a 1 mm channel pitch. In its standard arrangement, the PMT array is used with only a single excitation point, and the emission signal is spread across the entire array. Since each PMT detector – TCSPC channel pair has its own pulse pileup limit of 5% of the repetition rate, the instrument is able to perform TCSPC with a 16-fold increase in collection rate without suffering pileup effects. While this addresses the pulse pileup limit, it does not take into account cell viability: photobleaching and photodamage. Notably, it has also been found that the higher order photon interactions in multiphoton excitation lead to faster photobleaching compared to one-photon excitation [61], meaning a multiphoton technique should be even more constrained to a maximum excitation power.

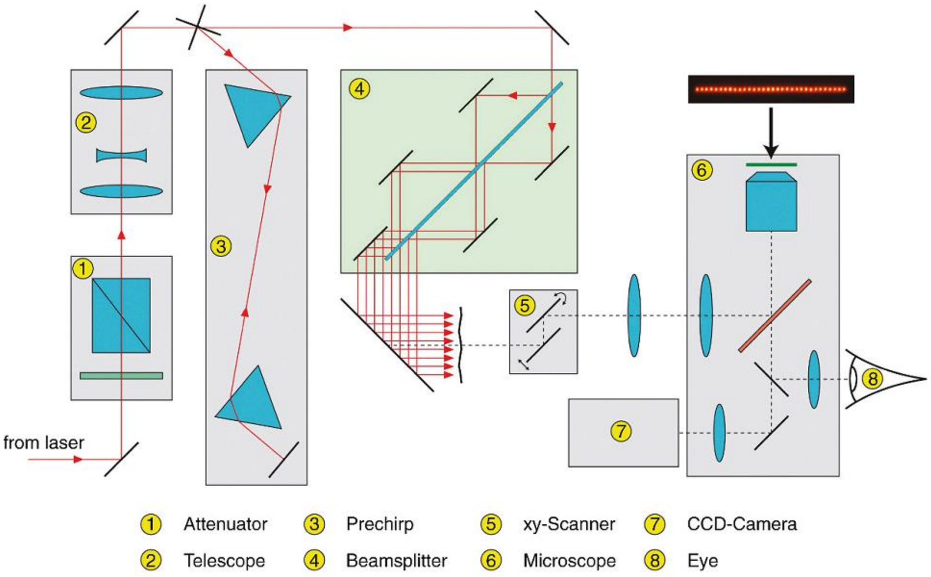

Figure 2-6: Light path of the LaVision BioTec TriM Scope [63].

Kumar et al also used the TriM Scope II with the FLIM module to obtain a 16-spot scan across the sample [62]. The 16-channel PMT was arranged to share the same orientation as the 1D foci array. A single axis galvo head performed the fast scan, perpendicular to the 1D array axis, while the slow scan was performed by moving the microscope stage. Since the active areas are long, the foci do not need to be descanned along the fast axis in order to be detected, and the foci are stationary along the slow axis (with the microscope stage moving instead).

Visitech VT-Infinity3

The Visitech VT-Infinity3 also has a similar working principle to the Opterra II. Instead of using a 1D pinhole array, the spots are generated with a 2D microlens array and the confocal effect is accomplished with a 2D variable diameter pinhole array. The vertical positions of the foci are staggered such that a single axis galvo scan results in a full scan of the sample. On the return path, the front face of the galvo is used to descan the foci to align back with the pinholes, while the back face of the galvo is used to rescan the image across an image sensor. This path is shown in Figure 2-7.

2.7. Discussion

The recent struggles of the pharmaceutical industry to develop novel drugs has made clear that current practices for early stage drug leads screening are not sufficient for determining drug candidates. Billions of dollars are wasted every

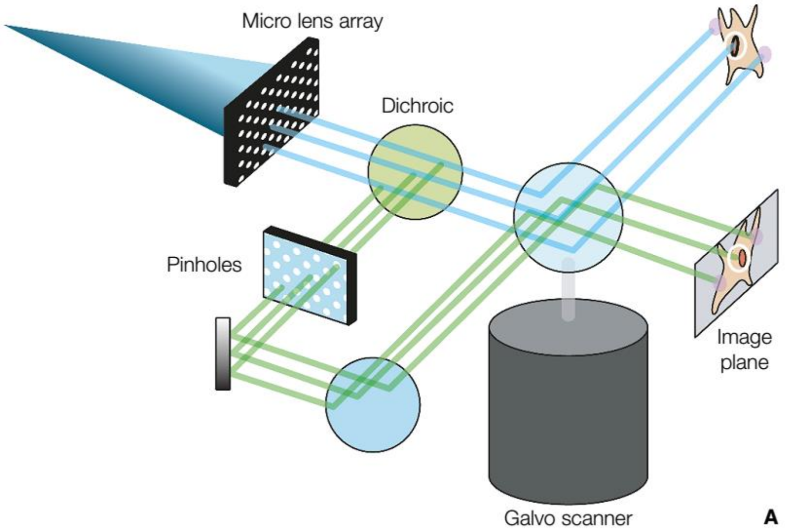

Figure 2-7: Light path of the Visitech VT-Infinity3 [63].

year pursuing promising drug candidates that are ultimately ruled ineffective or unsafe in clinical trials. Using FLIM FRET as a means of monitoring specific protein-protein interactions would provide a powerful new way to test drug leads, providing real insight into the underlying processes.

Applying FLIM-FRET as a tool for HCS is not straightforward. As outlined in Section 2.5, there is a series of important requirements that need to be fulfilled in order to create a FLIM module for HCS that is both useful and suitably high-throughput. The solution must be confocal in order to provide optical sectioning of the cell samples. It must also be fast-scanning in order to achieve high-throughput, and yet the excitation intensity must be kept low in order to prevent photobleaching and photodamage. With these factors combined, a multi-point confocal approach is considered ideal.

Multi-point confocal scanners are also quite common for this purpose. The majority of HCS microscopes employ a spinning disk confocal module to balance these same factors. The difference in the case of measuring FLIM FRET is that a widefield detector (i.e. gated ICCD) is not suitable in order to achieve a sufficient temporal resolution. The two detection options with acceptable temporal resolution are TCSPC detectors and the streak camera. Since TCSPC detectors of more than 16 detectors are not commercially available, the streak camera – which can fit 100 channels along its slit – appears to be the detector of choice.

For this reason, alternative scanning options need to be investigated. The three presented alternative options are all similar in that they use mirror galvos in order to perform the scan. Unlike the spinning disk, the return path through the mirror galvos causes the returning fluorescent light to descan back to its initial position.

This is a desired characteristic for this application, where the light needs to be traced back to discrete detectors instead of an imaging detector. However, each of these commercial scanners works with an imaging detector, and so is designed to rescan the fluorescence foci across the imaging detector.

The goal of the project is then to design a multi-point confocal system with optical scanner that uses a streak camera to collect a large number of fluorescence decays simultaneously. The system is being designed with the concept of being able to connect as a module to existing HCS microscope platforms, providing a turnkey solution for drug screening laboratories.

References

[1] Tufts University, "Cost to develop and win marketing approval for a new drug is $2.6 billion," 18 November 2014. [Online]. Available: http://csdd.tufts.edu/news/complete_story/pr_tufts_csdd_2014_cost_study. [Accessed 22 September 2016].

[2] F. Pammolli, L. Magazzini and M. Riccaboni, "The productivity crisis in pharmaceutical R&D," *Nature Drug Discovery,* vol. 10, no. June, pp. 428-438, 2011.

[3] I. Khanna, "Drug discovery in pharmaceutical industry: productivity challenges and trends," *Drug Discovery Today,* vol. 17, no. 19/20, pp. 1088-1102, 2012.

[4] M. Hay, D. W. Thomas, J. L. Craighead, C. Economides and J. Rosenthal, "Clinical development success rates for investigational drugs," *Nature Biotechnology,* vol. 32, no. 1, pp. 40-51, 2014.

[5] S. M. Paul, D. S. Mytelka, C. T. Dunwiddie, C. C. Persinger, B. H. Munos, S. R. Lindborg and A. L. Schacht, "How to improve R&D productivity: the pharmaceutical industry's grand challenge," *Nature Reviews Drug Discovery,* vol. 9, no. 3, pp. 203-214, 2010.

[6] Y. Etzion and A. J. Muslin, "The application of phenotypic high-throughput screening techniques to cardiovascular research," *Trends in Cardiovascular Medicine,* vol. 19, no. 6, pp. 207-212, 2009.

[7] F. Zanella, J. B. Lorens and W. Link, "High content screening: seeing is believing," *Trends in Biotechnology,* vol. 28, no. 5, pp. 237-245, 2010.

[8] S. Jupp, J. Malone, T. Burdett, J.-K. Heriche, E. Williams, J. Ellenberg, H. Parkinson and G. Rustici, "The cellular microscopy phenotype ontology," *Journal of Biomedical Semantics,* vol. 7, no. 28, pp. 1-8, 2016.

[9] J. Kotz, "Phenotypic screening, take two," *Science-Business eXchange,* vol. 5, no. 15, pp. 1-3, 2012.

[10] U. S. Eggert and T. J. Mitchison, "Small molecule screening by imaging," *Current Opinion in Chemical Biology,* vol. 10, no. 3, pp. 232-237, 2006.

[11] H. Brahmbhatt, S. Oppermann, E. Osterlund, B. Leber and D. W. Andrews, "Molecular pathways: leveraging the BCL-2 interactome to kill cancer cells - mitochondrial outer membrane permeabilization and beyond," *Clinical Cancer Research,* vol. 21, no. 12, pp. 2671-2676, 2015.

[12] D. E. Scott, A. R. Bayly, C. Abell and J. Skidmore, "Small molecules, big targets: drug discovery faces the protein-protein interaction challenge," *Nature Reviews Drug Discovery,* vol. 15, no. 8, pp. 533-550, 2016.

[13] C. B. Thompson, "Apoptosis in the pathogenesis and treatment of disease," *Science,* vol. 267, no. 5203, pp. 1456-1462, 1995.

[14] I. M. Ghobrial, T. E. Witzig and A. A. Adjei, "Targeting apoptosis pathways in cancer therapy," *CA: Cancer Journal for Clinicians,* vol. 55, no. 3, pp. 178-194, 2005.

[15] H. P. Erickson, "Size and shape of protein molecules at the nanometer level determined by sedimentation, gel filtration, and electron microscopy," *Biological Procedures Online,* vol. 11, no. 1, pp. 32-51, 2009.

[16] A. M. Sydor, K. J. Czymmek, E. M. Puchner and V. Mennella, "Super-resolution microscopy: from single molecules to supramolecular assemblies," *Trends in Cell Biology,* vol. 25, no. 12, pp. 730-748, 2015.

[17] G.-J. Kremers, D. W. Piston and M. W. Davidson, "Microscopy U: Basics of FRET Microscopy," Nikon Instruments, 2016. [Online]. Available: https://www.microscopyu.com/applications/fret/basics-of-fret-microscopy. [Accessed 17 January 2017].

[18] D. W. Piston and G.-J. Kremers, "Fluorescent protein FRET: the good, the bad and the ugly," *Trends in Biochemical Sciences,* vol. 32, no. 9, pp. 407-414, 2007.

[19] H. C. Ishikawa-Ankerhold, R. Ankerhold and G. P. C. Drummen, "Advanced fluorescence microscopy techniques - FRAP, FLIP, FLAP, FRET and FLIM," *Molecules,* vol. 17, no. 4, pp. 4047-4132, 2012.

[20] J. R. Lakowicz, H. Szmacinski and M. L. Johnson, "Ca2+ ion concentration imaged by FLIM of Quin-2 and Fura-2," *Journal of Fluorescence,* vol. 2, no. 1, pp. 47-62, 1992.

[21] H.-J. Lin, P. Herman and J. R. Lakowicz, "Fluorescence lifetime-resolved pH imaging of living cells," *Cytometry A*, vol. 52, no. 2, pp. 77-89, 2003.

[22] H. Wallrabe and A. Periasamy, "Imaging protein molecules using FRET and FLIM microscopy," *Current Opinion in Biotechnology*, vol. 16, no. 1, pp. 19-27, 2005.

[23] J. Lakowicz, "Time-Domain Lifetime Measurements," in *Principles of Fluorescence Spectroscopy*, New York, Springer, 2006, pp. 97-155.

[24] PicoQuant GmbH, "LDH Series Picosecond Laser Diode Heads," November 2016. [Online]. Available: https://www.picoquant.com/images/uploads/downloads/ldh_series.pdf. [Accessed 17 January 2017].

[25] Becker & Hickl, "16 Channel TCSPC / FLIM Detectors," January 2016. [Online]. Available: http://www.becker-hickl.com/pdf/pml16c27.pdf. [Accessed 17 January 2017].

[26] LaVision GmbH, "Ultra-Fast Gated Cameras," [Online]. Available: http://www.lavision.de/en/products/cameras/ultrafast_gated_cameras.php. [Accessed January 17 2017].

[27] Stanford Computer Optics, "Image intensifier: Photocathode," 2013. [Online]. Available: http://www.stanfordcomputeroptics.com/technology/image-intensifier/photocathode.html.

[28] Keysight Technologies, "Keysight U5310A PCIe High-Speed Digitizer with On-Board Processing," 30 April 2016. [Online]. Available: http://literature.cdn.keysight.com/litweb/pdf/5992-1538EN.pdf?id=2745996. [Accessed 17 January 2017].

[29] P. Summ, "Application Note: Detection quantum efficiency of Optoscope streak systems," Optronis.

[30] W. Becker, "Fluorescence lifetime imaging - techniques and applications," *Journal of Microscopy*, vol. 247, no. 2, pp. 119-136, 2012.

[31] P. R. Barber, S. M. Ameer-Beg, J. Gilbey, L. M. Carlin, M. Keppler, T. C. Ng and B. Vojnovic, "Multiphoton time-domain fluorescence lifetime imaging microscopy: practical application to protein-protein interactions using global analysis," *Journal of the Royal Society Interface*, vol. 6, no. S1, pp. S93-S105, 209.

[32] Q. Zhao, I. Young and J. de Jong, "Photon budget analysis for fluorescence lifetime imaging microscopy," *Journal of Biomedical Optics*, vol. 16, no. 8, p. 086007, 2011.

[33] D. M. Grant, W. Zhang, E. J. McGhee, T. D. Bunney, C. B. Talbot, S. Kumar, I. Munro, C. Dunsby, M. A. A. Neil, M. Katan and P. M. W. French, "Multiplexed FRET to image multiple signaling events in live cells," *Biophysical Journal,* vol. 95, pp. L69-L71, 2008.

[34] Optronis GmbH, "Optronis SC-10 Streak Camera Main Unit," March 2014. [Online]. Available: http://www.optronis.com/fileadmin/Upload/Product/Streak/SC-10.pdf. [Accessed 17 January 2017].

[35] R. Brooks, M. Ingle, J. Milnes and J. Howorth, "Wavelength-dependent resolution and electron energy distribution measurements of image intensifiers," in *Proceedings of the SPIE 6294,* San Diego, USA, 2006.

[36] Stanford Computer Optics, "Image intensifier: Phosphor screen," Stanford Computer Optics, 2013. [Online]. Available: http://www.stanfordcomputeroptics.com/technology/image-intensifier/phosphor-screen.html. [Accessed 17 January 2017].

[37] H. C. Gerritsen, A. Draaijer, D. J. van den Heuvel and A. V. Agronskaia, "Fluorescence lifetime imaging in scanning microscopy," in *Handbook of Biological Confocal Microscopy*, New York, Springer, 2006, pp. 516-534.

[38] A. Elder, S. Schlacter and C. F. Kaminski, "Theoretical investigation of the photon efficiency in frequency-domain fluorescence lifetime imaging microscopy," *Journal of the Optical Society of America A,* vol. 25, no. 2, pp. 452-462, 2008.

[39] ISS, "Alba v5 Laser Scanning Microscope for FFS/FLIM," 2014. [Online]. Available: http://www.iss.com/resources/pdf/datasheets/ISS_Albav5_DataSheet.pdf. [Accessed 18 January 2017].

[40] E. Povrozin, N. Redes and B. Barbieri, "Phasor plots for the analysis of time-resolved fluorescence," 2013. [Online]. Available: http://www.iss.com/resources/pdf/technotes/Time-resolved_Fluorescence_Phasor_Plots.pdf. [Accessed 18 January 2017].

[41] W. F. An and N. Tolliday, "Cell-based assays for high-throughput screening," *Molecular Biotechnology,* vol. 45, no. 2, pp. 180-186, 2010.

[42] E. Wang, C. M. Babbey and K. W. Dunn, "Performance comparison between the high speed Yokogawa spinning disc confocal system and single-point scanning confocal systems," *Journal of Microscopy,* vol. 218, pp. 148-159, 2005.

[43] V. Magidson and A. Khodjakov, "Circumventing photodamage in live cell microscopy," *Methods in Cell Biology,* vol. 114, pp. 545-560, 2013.

[44] S. E. Webb, Y. Gu, S. Lévêque-Fort, J. Siegel, M. J. Cole, K. Dowling, R. Jones and P. M. French, "A wide-field time-domain fluorescence lifetime imaging microscope with optical sectioning," *Review of Scientific Instruments*, vol. 73, no. 4, p. 1898, 2002.

[45] S. P. Poland, N. Krstajić, J. Monypenney, S. Coelho, D. Tyndall, R. J. Walker, V. Devauges, J. Richarson, N. Dutton, P. Barber, D. D.-U. Li, K. Suhling, T. Ng, R. K. Henderson and S. M. Ameer-Beg, "A high speed multifocal multiphoton fluorescence lifetime imaging microscope for live-cell FRET imaging," *Biomedical Optics Express,* vol. 6, no. 2, p. 277, 2015.

[46] D. K. Toomre, M. F. Langhorst and M. W. Davidson, "Introduction to Spinning Disk Confocal Microscopy," [Online]. Available: http://zeiss-campus.magnet.fsu.edu/articles/spinningdisk/introduction.html. [Accessed 18 January 2017].

[47] D. Toomre and J. Pawley, "Disk-scanning confocal microsopy live cell imaging: probing the future," in *Biological Confocal Microscopy*, New York, USA, Springer, 2006, pp. 223-238.

[48] J. Oreopoulos, R. Berman and M. Browne, "Spinning-disk confocal microscopy: present technology and future trends," *Methods in Cell Biology*, vol. 123, pp. 153-175, 2014.

[49] Perkin Elmer, "Opera High Content Screening System," 2008. [Online]. Available: http://www.flyrnai.org/supplement/BRO_OperaHighContentScreeningSystem.pdf. [Accessed 19 January 2017].

[50] Perkin Elmer, "Opera Phenix High Content Screening System," December 2013. [Online]. Available: http://www.perkinelmer.com/lab-solutions/resources/docs/BRO_011289_01_Opera_Phenix.pdf. [Accessed 19 January 2017].

[51] GE Healthcare Life Sciences, "IN Cell Analyzer 6000," 2017. [Online]. Available: http://www.gelifesciences.com/webapp/wcs/stores/servlet/ProductDisplay?categoryId=10970&catalogId=10101&productId=96736&storeId=11756. [Accessed 19 January 2017].

[52] L. Li, Q. Zhou, T. C. Voss, K. L. Quick and D. V. LaBarbera, "High-throughput imaging: Focusing in on drug discovery in 3D," *Methods,* vol. 96, no. 6, pp. 97-102, 2016.

[53] BD Biosciences, "BD Pathway High-Content Analyzers," 2009. [Online]. Available: https://www.bdbiosciences.com/documents/Pathway_TechSpec.pdf. [Accessed 19 January 2017].

[54] Molecular Devices, "ImageXpress Micro Confocal High-Content Imaging System," 2015. [Online]. Available: http://go.moleculardevices.com/l/83942/2015-11-17/y26tz/83942/29419/ImageXpress_Micro_Confocal_Brochure_1993B.pdf. [Accessed 19 January 2017].

[55] Thermo Fisher Scientific, "ArrayScan High-Content Systems," 2016. [Online]. Available: http://www.thermofisher.com/ca/en/home/life-science/cell-analysis/cellular-imaging/high-content-screening/high-content-screening-instruments/arrayscan-hca-readers.html. [Accessed 19 January 2017].

[56] TTP Labtech, "Acumen Cellista," [Online]. Available: http://ttplabtech.com/wp-content/uploads/2012/10/acumen-Cellista_TTPLabtech-brochure-V1.pdf. [Accessed 19 January 2017].

[57] Yokogawa Electric Corporation, "CV7000S," 2017. [Online]. Available: https://www.yokogawa.com/solutions/products-platforms/life-science/high-throughput-cytological-discovery-system/cv7000s/. [Accessed 19 January 2017].

[58] Bruker, "Optera II Specifications," 2017. [Online]. Available: https://www.bruker.com/products/fluorescence-microscopes/opterra-confocal-microscopy/technical-details.html. [Accessed 19 January 2017].

[59] LaVision BioTec, "TriM Scope II - Specifications," [Online]. Available: http://www.lavisionbiotec.com/trim-scope-ii-specifications.html. [Accessed 19 January 2017].

[60] Visitech International, "VT-Infinity3 2D Array Scanning Laser Confocal Microscope," [Online]. Available: http://www.visitech.co.uk/assets/vt-infinity-3-flyer-(2).pdf. [Accessed 19 January 2017].

[61] G. H. Patterson and D. W. Piston, "Photobleaching in two-photon excitation microscopy," *Biophysical Journal*, vol. 78, no. 4, pp. 2159-2162, 2000.

[62] S. Kumar, C. Dunsby, P. A. A. De Beule, D. M. Owen, U. Anand, P. M. P. Lanigan, R. K. P. Benninger, D. M. Davis, M. A. A. Neil, P. Anand, C. Benham, A. Naylor and P. M. W. French, "Multifocal multiphoton excitation and time correlated single photon counting detection for 3-D fluorescence lifetime imaging," *Optics Express*, vol. 15, pp. 12548-12561, 2007.

[63] J. B. Pawley, "Light Paths of the Current Commercial Confocal Light Microscopes Used in Biology," in *Biological Confocal Microscopy*, New York, USA, Springer, 2006, pp. 906-917.

Chapter 3

Paper I – Streak camera crosstalk reduction using a multiple delay optical fiber bundle

Anthony Tsikouras[1], Jin Ning[2], Sandy Ng[3], Richard Berman[4], David W. Andrews[4], and Qiyin Fang[1,2,*]

[1]*Department of Engineering Physics, McMaster University, 1280 Main Street West, Hamilton, Ontario, L8S 4L7, Canada*

[2]*Department of Biomedical Engineering, McMaster University, 1280 Main Street West, Hamilton, Ontario, L8S 4L7, Canada*

[3]*Spectral Applied Research, 9071 Leslie Street Unit 11, Richmond Hill, Ontario, L4B 3L8, Canada*

[4]*Department of Biochemistry and Biomedical Sciences, McMaster University, 1280 Main Street West, Hamilton, Ontario, L8S 4L7, Canada*

Published in Optics Letters; 37(2):250-252, 2012

Printed with permission

Introduction to Paper I

This chapter focuses on the role of the alternating fiber delay technique in multiplexing the streak camera input slit while minimizing the level of crosstalk between adjacent channels. The degree of multiplexing is a critical factor in the selection of the streak camera as an instrument for performing fluorescence lifetime imaging microscopy (FLIM). The fiber delay technique essentially doubles the number of fluorescence channels that can be fit in the streak camera's photocathode without incurring an optical crosstalk penalty.

In this work, the alternating delay fiber bundle was connected to the streak camera and the degree of optical crosstalk was gauged by the peak-to-valley ratio of the streak profile. The optical crosstalk was measured when the streak camera's sweep unit was active and when it was inactive, in order to demonstrate the impact of the fiber delay scheme. The optical crosstalk was found to be 19 ± 4 % with the fiber delay and 52 ± 11 % without the delay. The extra length of fiber was also not found to have an effect on the estimated fluorescence lifetime. A scanned image of *Convallaria* with intensity normalization applied between fibers. This was able to visually demonstrate the impact of reduced optical crosstalk, appearing as a contrast enhancement.

This work shows the ability to use the streak camera to measure 100 fluorescence channels without significant crosstalk. The targeted audience for this paper includes researchers investigating FLIM methods, as well as any time-resolved measurement modality that could benefit from a streak camera (e.g. photoluminescence in semiconductor physics). This manuscript was prepared by me and revised by the coauthors.

Contents of Paper I

Abstract

The streak camera is one of the fastest photodetection systems, while its capability of multiplexing is particularly attractive to many applications requiring parallel data acquisition. The degree of multiplexing in a streak camera is limited by the crosstalk between input channels. We developed a technique that introducing a fixed time delay between adjacent fiber channels in a customized two-dimensional to one-dimensional fiber array to significantly reduce crosstalk both at the sample plane and at the input of a streak camera. A prototype system has been developed that supports 100 input channels, and its performance in fluorescence microscopy is demonstrated.

3.1. Article

A streak camera is one of the fastest time-domain photo-detection systems with picoseconds resolution [1-3], which is achieved by using a time-varying voltage to deflect photoelectrons perpendicular to their direction of travel. The time of photoelectron generation therefore correlates to spatial position on a readout camera.

Over the past two decades, several groups have developed streak camera based fluorescence lifetime imaging microscopy (FLIM) techniques [3-8], which measures fluorescence lifetime in addition to intensity [9-13]. For example, Krishnan et al. developed a multiphoton FLIM system with both high temporal resolution (from the streak camera) and spatial resolution (from the scanning multi-photon illumination) [6, 7]. In this design, a single excitation point is raster-scanned across the field of view to generate a 2-dimensional (2D) lifetime image.

Similar to an imaging spectrograph, a streak camera supports multiple input channels, which makes it inherently suited for high-throughput applications such as FLIM. Qu *et al.* [8] and Shao *et al.* [14] used a microlens array to divide a laser beam into a 4 x 4 array of foci, and also a special streak camera input consisting of a matching pinhole array. A prism was used after the pinhole input, resulting in a 4 x 4 array of streak images combined with spectral information. This approach led to a substantial improvement of throughput by multiplexing but it required a special wide photocathode [8] and further multiplexing was limited by the photocathode’s spatial resolution [15]. The multiplexing ability is limited by crosstalk between adjacent input channels, which not only reduce image quality but also hinders the accurate estimation of time-domain data (e.g. lifetime). Instead of generating a 2D array at the input of a streak camera, we developed a 2D to one-dimensional (1D) fiber array that transfers the image of a 2D array of spots on the sample to a linear array entering a conventional streak camera with a slit photocathode. Crosstalk between channels at the sample plane on the 2D end is reduced by using large pitch between individual channels. Throughput improvement may be realized by increasing the number of fibers in the array, which is limited by the spatial resolution of the photocathode and crosstalk between adjacent fiber inputs at the 1D end. (Details of this design will be reported elsewhere.)

Besides spatial separation, short pulses/decays may be separated in time, by varying the optical path length to introduce a delay in the time domain [16]. In this report, we present a novel fiber bundle design that can significantly reduce crosstalk at the 1D end of the streak camera input by introducing a fixed optical path length difference between adjacent fibers. We demonstrate that this design significantly reduces crosstalk between adjacent fibers such that it enables a much greater degree of multiplexing at the streak camera input. This design is applicable for not only FLIM, but other multichannel applications using a streak camera.

Figure 3-1 shows the schematic of the experimental setup. Two microlenslet arrays (500 μm center-to-center pitch, square microlenses, SUSS MicroOptics, Neuchâtel, Switzerland) are used to generate arrays of excitation foci on the sample and focus the fluorescence emission to the fiber array. A diode laser (3 mW, 60 ps LDH-P-C-440M, PicoQuant GmbH, Berlin, Germany) provides pulsed excitation at 440 nm, which goes through the first lenslet array to generate a 10 x 10 array of foci. A 445 nm dichroic filter (Di01-R442-25x36, Semrock, Rochester, NY) reflects the beams to the side imaging port of an inverted fluorescence microscope (Axiovert 200, Carl Zeiss AG, Oberkochen, Germany). Fluorescence emission from the sample is relayed back through the two lenslet array, past an emission filter (FF01-542/27-25, Semrock) and focused onto the 2D end of a customized 2D-1D fiber array (0.11 NA, fused silica, n = 1.44, 50 μm diameter core, 50 μm cladding). At the 1D end of the fiber array, the fibers are arranged into a linear 1 x 100 array and coupled to the input slit of a streak camera (SC-10, Optronis, Kehl, Germany). In the fiber array, adjacent fibers are of alternating lengths of 1 and 2 m, which leads to a temporal separation of 4.8 ns. This temporal separation is translated into a spatial separation of 4.8 mm when sweeping at 1 ns/mm. FLIM acquisition is achieved by raster scanning the sample so that the 2D foci array covers the full frame. A lookup table correlating the 2D foci array to the 1D array on the streak camera readout is used to reconstruct the final FLIM image.

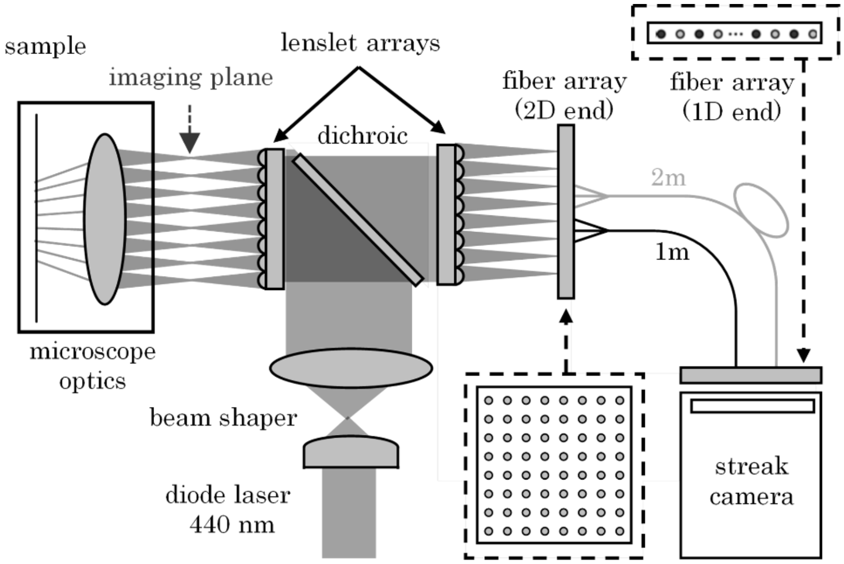

Figure 3-1. Instrument setup for multiple delay optical fiber array streak imaging.

The overall system temporal response is limited by a number of factors including the laser pulse width (60 ps), the fiber modal dispersion (15-30 ps), and the fiber core size (50 μm), which translates to a 50 ps spot at the streak camera readout. The impulse response of the system is measured to be 126 ps FWHM.

To demonstrate the crosstalk reduction using the alternating fiber delay lines, Coumarin 6 (546283, Sigma-Aldrich, St. Louis, Missouri) dissolved in ethanol solution (5 μM) is measured to form a uniform distributed image using the sweep on and sweep off modes of the streak camera. The sweep on mode is the normal operating mode of the streak camera, where a time-varying ramp voltage is applied on the horizontal (temporal) direction. As shown in Figure 3-2(b), fluorescence decay from each fiber becomes a streak on the readout camera. In this case, the difference in fiber lengths results in a right shift of 4.8 mm for longer fibers, which are spatially separated from streaks from the adjacent shorter fibers. As shown in Figure 3-2, each of the streaks is visibly separate with low crosstalk between adjacent channels.

To quantify the reduction in crosstalk achieved using alternating 1 and 2 m fibers, the extent of crosstalk when the fiber delay is not present was simulated by acquiring images using the sweep off mode. In this mode, there is no time-dependent deflection of electrons such that all photoelectrons reach the readout camera at the same time-axis location. As a result, the time delay between adjacent fibers does not lead to spatial separation on the readout camera, which is similar to the crosstalk between two adjacent streaks when the time delay is not present. As shown in Figure 3-2(c), the crosstalk between adjacent spots is obvious when the streak camera is operated in the sweep off mode.

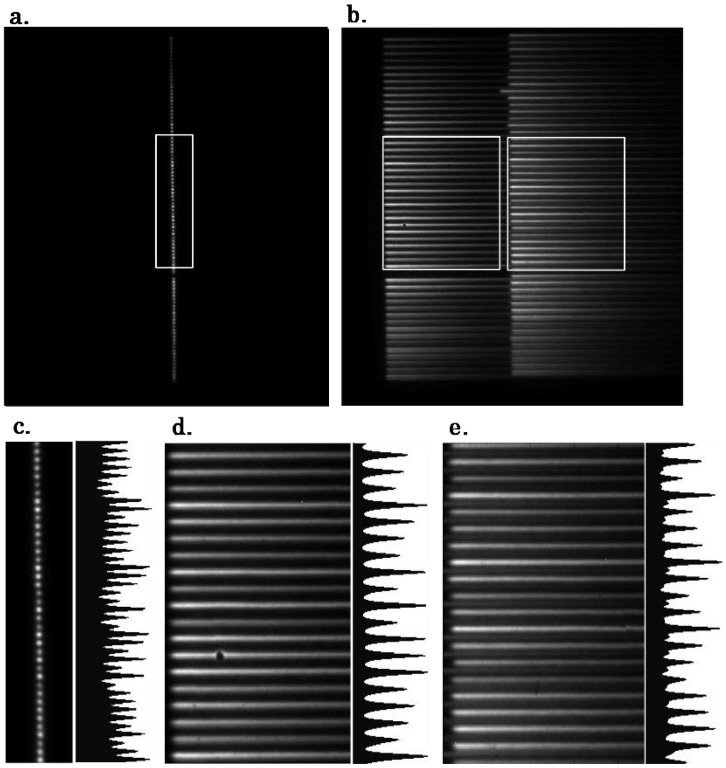

Figure 3-2. Streak images of fiber array inputs, with corresponding intensity profiles. (a) Fiber array imaged at the sweep off mode, (b) fiber array imaged at the sweep on mode. The left and right columns of streaks are from the 1 and 2 m fibers, respectively. (c) Magnified view of spots in the sweep off mode with corresponding intensity profile, (d), (e) magnified views of the sweep off mode and the corresponding intensity profiles.

To compare the crosstalk between the two modes quantitatively, intensity profiles of the spots in Figure 3-2(a) and the streaks in Figure 3-2(b) were calculated with the background noise subtracted. The crosstalk between adjacent channels was defined by the ratio of the valley between two spots to the average of the two adjacent peaks. The crosstalk in sweep off mode, which simulates a fiber array without alternating fiber lengths, was 52 ± 11 %. The crosstalk in sweep on mode was 19 ± 4 % and 33 ± 11 % for 1 m fibers and 2 m fibers, respectively. The 2 m fibers have significantly more crosstalk with the addition of the residual decay of the 1m streaks, which may be removed using incomplete decay algorithms [17, 18]. The lifetime of the Coumarin 6 was 2.58 ± 0.04 ns when fitted to a multiexponential decay. It is in good agreement with literature reported values [19].

Figure 3-3 shows steady-state fluorescence images of fixed *Convallaria* specimens (*Convallaria Majalis* fixed sample, Leica, Wetzlar, Germany) using the fiber array multiplexing method presented. The *Convallaria* sample is stained with safranin (530 nm, 590 nm) and fast green (620 nm, 660 nm) [20]. The sample was scanned using an X-Y stage with 40 steps and a 20x objective. The resulting image resolution is 1.3 μm, but the resolution can be improved to the objective limit of 0.6 μm by increasing the number of steps taken by the X-Y stage. Fig. 3a shows the fluorescence image acquired in the sweep off mode, simulating the situation when there is no fiber delay present.

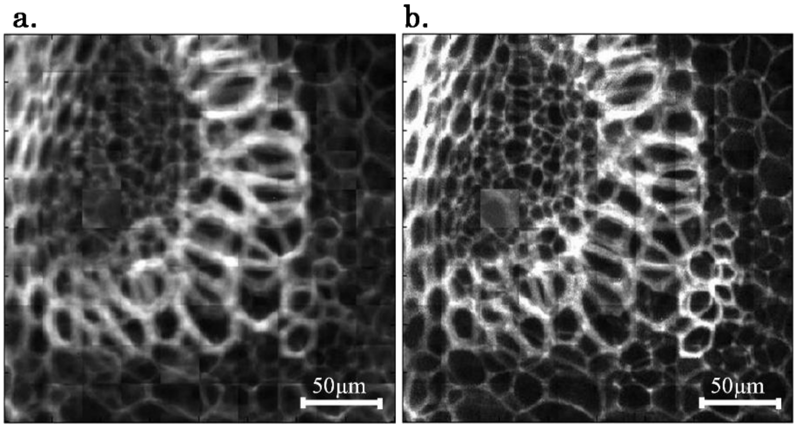

Figure 3-3. Reconstructed fluorescence intensity images of fixed *Convallaria* specimens imaged without sweeping (a) and with sweeping (b). When the streak camera is not sweeping (a), the fiber delay between adjacent fibers is not present and the image is reconstructed from steady-state acquisitions such as in Figure 3-2(c). When the streak camera is sweeping (b), the image is reconstructed from time-resolved acquisitions such as in Figure 3-2(d-e).

The images were reconstructed from the 1600 streak images. Furthermore, a normalization factor was applied to each channel to correct its intensity variations. The normalization table was obtained by each channel's intensity measurement when imaging a uniform paper fluorescence standard.

To acquire images shown in Figure 3-3, 0.5 s integration was required for each step, depending on sweep mode. This leads to over 800 s to acquire a full FLIM image. It should be noted that the current FLIM setup is optimized not for high speed but for the demonstration of the performance of crosstalk reduction. For example, the diode laser pulse energy is 75 pJ/pulse which is shared by over 100 foci. The acquisition time in this setup is also limited by the 4 MHz repetition rate of the streak camera, where the laser can operate at 40 MHz. A higher intensity laser and high repetition synchroscan sweeping module can significantly improve acquisition speed.

Figure 3-3(b) shows the time-integrated fluorescence image of the same sample region in the sweep on mode demonstrating the reduced crosstalk. Although the sweep off mode image (Figure 3-3(a)) shows better signal intensity, the sweep on image (Figure 3-3(b)) shows significantly improved contrast from lower crosstalk. This is especially apparent in the low-signal regions of the image, where crosstalk from an adjacent fiber would be especially detrimental.

The lifetime of most fluorescent probes used in FLIM are shorter than 4 ns. By introducing a 4.8 ns delay, lifetime estimation based on the intensity decay of the shorter fiber is minimally affected by the adjacent longer fibers. Nonetheless, different delay times can be introduced by using fibers of different lengths. A time-domain signal measured from the longer fibers only suffers from the residual decay (>4.8 ns) from the shorter fibers. This is similar to the incomplete decay effect commonly seen with high repetition rate laser excitation and may be corrected mathematically [17, 18]. Depending on the lifetime being studied, signal multiplexing may be increased further by introducing more groups with different delays. In addition to lifetime, the time delay is also limited by the overall width of the time window on the streak camera (20 ns in our case).

Because of the length limitation of this short communication, fluorescence lifetime imaging results as well as a detailed description of the FLIM system setup will be reported elsewhere. It is, however, important to confirm that the delayed fibers are able to measure the same lifetime decays as the non-delayed fibers.

In summary, alternating the length of adjacent fibers significantly reduces crosstalk between adjacent fiber channels and thereby increases the degree of multiplexing possible when using a streak camera to measure multiple input channels simultaneously. This technique is expected to be particularly useful both for live cell imaging and for high-throughput automated imaging as used in drug discovery systems, where the speed at which a FLIM image is acquired is a major hurdle.

The authors would like to thank P. Sinclair for his assistance in the FLIM system design. This project is supported by funding from the Canadian Institutes of Health Research [161934 (Q. F. & D. W. A.); FRN 10490 (D. W. A.)], the Ontario Centres of Excellence (Q. F. & D. W. A.), the Canadian Foundation of Innovation/Ontario Ministry of Research and Innovation (Q. F. & D. W. A.), and the Natural Sciences & Engineering Research Council. (D. W. A. holds the Canada Research Chair in Membrane Biogenesis, Q. F. holds the Canada Research Chair in Biophotonics.

References

[1] A. J. Campillo and S. L. Shapiro, "Picosecond streak camera fluorometry - A review," *IEEE Journal of Quantum Electronics,* vol. 19, no. 4, pp. 585-603, 1983.

[2] M. Nisoli and G. Sansone, "New frontiers in attosecond science," *Progress in Quantum Electronics,* vol. 33, no. 1, pp. 17-59, 2009.

[3] J. Mizeret, T. Stepinac, M. Hansroul, A. Studzinski, H. van den Bergh and G. Wagnières, "Instrumentation for real-time fluorescence lifetime imaging in endoscopy," *Review of Scientific Instruments,* vol. 70, no. 12, pp. 4689-4701, 1999.

[4] C. Biskup, T. Zimmer and K. Benndorf, "FRET between cardiac Na+ channel subunits measured with a confocal microscope and a streak camera," *Nature Biotechnology,* vol. 22, no. 2, pp. 220-224, 2004.

[5] A. Kusumi, A. Tsuji, M. Murata, Y. Sako, A. C. Yoshizawa, S. Kagiwada, T. Hayakawa and S. Ohnishi, "Development of a streak-camera-based time-resolved microscope fluorometer and its application to studies of membrane fusion in single cells," *Biochemistry,* vol. 30, no. 26, pp. 6517-6527, 1991.

[6] R. V. Krishnan, A. Masuda, V. E. Centonze and B. Herman, "Quantitative imaging of protein–protein interactions by multiphoton fluorescence lifetime imaging microscopy using a streak camera," *Journal of Biomedical Optics,* vol. 8, no. 3, pp. 362-367, 2003.

[7] R. V. Krishnan, H. Saitoh, H. Terada, V. E. Centonze and B. Herman, "Development of a multiphoton fluorescence lifetime imaging microscopy system using a streak camera," *Review of Scientific Instruments,* vol. 74, no. 5, pp. 2714-2721, 2003.

[8] J. Qu, L. Liu, D. Chen, Z. Lin, G. Xu, B. Guo and H. Niu, "Temporally and spectrally resolved sampling imaging with a specially designed streak camera," *Optics Letters,* vol. 31, no. 3, pp. 368-370, 2006.

[9] I. Bugiel, K. Konig and H. Wabnitz, "Investigations of cells by fluorescence laser scanning microscopy with subnanosecond resolution," *Lasers in the Life Sciences,* vol. 3, no. 1, pp. 47-53, 1989.

[10] X. F. Wang, T. Uchida and S. Minami, "A fluorescence lifetime distribution measurement system based on phase-resolved detection using an image dissector tube," *Applied Spectroscopy,* vol. 43, no. 5, pp. 840-845, 1989.

[11] Y. Fu and J. R. Lakowicz, "Enhanced fluorescence of Cy5-labeled DNA tethered to silver island films: fluorescence images and time-resolved studies using single-molecule spectroscopy," *Analytical Chemistry,* vol. 78, no. 17, pp. 6238-6245, 2006.

[12] Y. Chen and A. Periasamy, "Characterization of two-photon excitation fluorescence lifetime imaging microscopy for protein localization," *Microscopy Research and Technique,* vol. 63, no. 1, pp. 72-80, 2003.

[13] T. French, P. T. C. So, D. J. Weaver Jr., T. Coelho-Sampaio, E. Gratton, E. W. Voss Jr. and J. Carrero, "Two-photon fluorescence lifetime imaging microscopy of macrophage-mediated antigen processing," *Journal of Microscopy,* vol. 185, no. 3, pp. 339-353, 1997.

[14] Y. Shao, J. Qu, H. Li, Y. Wang, J. Qi, G. Xu and H. Niu, "High-speed spectrally resolved multifocal multiphoton microscopy," *Applied Physics B,* vol. 99, no. 4, pp. 633-637, 2010.

[15] M. Clampin and F. Paresce, "Spatial resolution characteristics of a GaAs-photocathode RANICON," *Review of Scientific Instruments,* vol. 60, no. 6, pp. 1092-1094, 1989.

[16] Y. Yuan, T. Papaiannou and Q. Fang, "Single-shot acquisition of time-resolved fluorescence spectra using a multiple delay optical fiber bundle," *Optics Letters,* vol. 33, no. 8, pp. 791-793, 2008.

[17] R. W. K. Leung, S. A. Yeh and Q. Fang, "Effects of incomplete decay in fluorescence lifetime estimation," *Biomedical Optics Express,* vol. 2, no. 9, pp. 2517-2531, 2011.

[18] Y. Sakai and S. Hirayama, "A fast deconvolution method to analyze fluorescence decays when the excitation pulse repetition period is less than the decay times," *Journal of Luminescence,* vol. 39, no. 3, pp. 145-151, 1988.

[19] Y. Sun, R. Day and A. Periasamy, "Investigating protein-protein interactions in living cells using fluorescence lifetime imaging microscopy," *Nature Protocols,* vol. 6, no. 9, pp. 1324-1340, 2011.

[20] J. H. Frank, A. D. Elder, J. Swartling, A. R. Venkitaraman, A. D. Jeyasekharan and C. F. Kaminski, "A white light confocal microscope for spectrally resolved multidimensional imaging," *Journal of Microscopy,* vol. 227, no. 3, pp. 203-215, 2007.

Chapter 4

Paper II – High-speed multifocal array scanning using refractive window tilting

Anthony Tsikouras[1], Richard Berman[2], David W. Andrews[3], and Qiyin Fang[1,4,*]

[1]*Department of Engineering Physics, McMaster University, 1280 Main Street West, Hamilton, Ontario, L8S 4L7, Canada*

[2]*Spectral Applied Research, 2 East Beaver Creek Road, Building #2, Richmond Hill, Ontario, L4B 2N3, Canada*

[3]*Department of Biochemistry, Sunnybrook Research Institute, University of Toronto, 2075 Bayview Avenue, Toronto, Ontario, M4N 3M5, Canada*

[4]*Department of Biomedical Engineering, McMaster University, 1280 Main Street West, Hamilton, Ontario, L8S 4L7, Canada*

Published in Biomedical Optics Express; 6(10):3737-3747, 2015

Printed with permission

Introduction to Paper II

This chapter describes the development and implementation of the window galvanometer-based scanner as a means of accomplishing a multifocal scan. The ability to perform a scan of the 10 x 10 foci without moving the microscope stage is important to the screening throughput of the system, as well as its ability to be a modular component of an existing high-content screening microscope.

In this work, the prospect of using a traditional mirror galvanometer to perform the multifocal scan is considered, and ultimately rejected due to complications involving the linearity and uniformity of the foci's movements. Instead, the window galvanometer scheme is considered, which allows for each beam in the array to be moved uniformly, with a reduction in additional required optics. Mirror and window galvanometer scanners are considered theoretically, and the linearity and uniformity of the window galvanometer is measured in a proof-of-principle setup to demonstrate its high linearity and uniformity. Following implementation of the scanner on the HCS FLIM system, a fixed slide of *Convallaria* is scanned with the window scanner, and intensity and lifetime images are presented from the resulting reconstruction.

This work shows the effectiveness of the window-based scanners as a solution for multifocal scanning. The targeted audience for this paper includes researchers in any application using multifocal raster scanning, as well as high resolution applications where the window-based scanner can offer higher precision than mirror galvanometers. This manuscript was prepared by me and revised by the coauthors.

Contents of Paper II

Abstract

Confocal microscopy has several advantages over wide-field microscopy, such as out-of-focus light suppression, 3D sectioning, and compatibility with specialized detectors. While wide-field microscopy is a faster approach, multiplexed confocal schemes can be used to make confocal microscopy more suitable for high-throughput applications, such as high-content screening (HCS) commonly used in drug discovery. An increasingly powerful modality in HCS is fluorescence lifetime imaging microscopy (FLIM), which can be used to measure protein-protein interactions through Förster resonant energy transfer (FRET). FLIM-FRET for HCS combines the requirements of high throughput, high resolution and specialized time-resolving detectors, making it difficult to implement using wide-field and spinning disk confocal approaches. We developed a novel foci array scan method that can achieve uniform multiplex confocal acquisition using stationary lenslet arrays for high resolution and high throughput FLIM. Unlike traditional mirror galvanometers, which work in Fourier space between scan lenses, this scan method uses optical flats to steer a 2-dimension foci array through refraction. After integrating this scanning scheme in a multiplexing confocal FLIM system, we demonstrate it offers clear benefits over traditional mirror galvanometer scanners in scan linearity, uniformity, cost and complexity.

4.1. Introduction

In confocal microscopy, an excitation focal point is raster scanned across the field of view to generate a 2- or 3-dimensional (2D or 3D) image [1]. A pair of confocal pinholes are used to preferentially reject light originating from outside of the focal plane, which significantly improves image contrast compared to wide-field microscopy. In general, confocal microscopy takes more time to acquire data, due to the need to scan in the spatial domain in order to form an image. Since only a single pixel photon detector and associated readout electronics are needed, this approach allows for the use of a very sensitive photo detection system with low noise at relatively low cost [2]. Single detection modules is particularly attractive in specific modalities such as time-resolved fluorescence [3] or spectroscopy [4, 5]. For instance, the cost and complexity of time-resolved imaging can be greatly reduced by using time-correlated single photon counting (TCSPC) methods [4, 5]. Point-scanning is also critical in other imaging modalities, such as multiphoton microscopy and stimulated emission depletion (STED) microscopy [6, 7].

There are many instances where the fast acquisition of a sample image is critical to the application. Live cell imaging, for instance, requires fast image acquisition such that the cells and intracellular components do not change significantly during acquisition [8]. Furthermore, in high content screening (HCS) a technique used in drug discovery, it requires a large number of images to be collected over a wide range of experimental conditions in order to establish a suitable set for statistical analysis [9].

One example is fluorescence lifetime imaging microscopy (FLIM), which measures the fluorescence decay dynamics in spectrally-resolved intensity images. It has found many applications in life sciences research [10] and drug discovery [11]. One of the major applications is to detect protein-protein interactions by using FLIM to measure Förster resonance energy transfer (FRET). In FLIM-FRET, the fluorescence lifetime is decreased when the excitation energy of a “donor” fluorophore is non-radiatively transferred to a nearby “acceptor” fluorophore [10–12]. Energy transfer is only efficient at very short distances, typically less than 10 nm. Therefore, by attaching donor and acceptor fluorophores onto a pair of targets (e.g. two proteins), it is possible to detect when these targets interact with each other [10, 12]. Compared to conventional steady state fluorescence imaging measurements, FLIM-FRET offers the advantages of not being affected by spectral crosstalk between the donor and acceptor, changes in excitation intensity, detector sensitivity and is relatively insensitive to differences in fluorophore population levels [10].

A new method of using both FLIM and intensity images to quantify protein-protein interactions in live cells [13, 14] has increased the need to collect data at high speed so that the intensity images and FLIM data are co-registered. Techniques able to achieve high speed FLIM-FRET measurements with good spatial resolution would be a significant advance for cell biology and drug discovery efforts, as it would enable measuring the modulation of protein-protein interactions by small molecules to identify leads for drugs. Current FLIM systems do not offer a good balance between resolution (spatial and temporal) and acquisition speed. For example, the majority of current FLIM systems use TCSPC techniques, which have good resolution but are too slow (minutes) for HCS applications [15]. Time-gated intensified CCD based time [16, 17] and frequency [18] domain imaging techniques offer faster (in seconds) images acquisition but suffer from limitations in spatial resolution, difficulty in resolving complex decay dynamics, and require high power excitation [15]. It is worth noting that out-of-focus light in a FLIM setup not only introduces a loss in spatial resolution, but distorts the multi-exponential decay collected at each pixel by adding contributions from out-of-focus fluorophores [19, 20].

One way to increase the rate of image acquisition is to increase the raster scan speed. This approach is of limited value when imaging biological specimens because scan speeds are frequently limited by the excitation time required to generate enough emitted photons to obtain a good image. Particularly for TCSPC, the requirement for low count rates renders it generally too slow for live cell imaging applications. In these situations, a good alternative to increase image acquisition speed is to parallelize the scanning process.

Point-scanning setups can be multiplexed using a pair of spinning disks, where specially patterned pinholes produce an array of foci, covering the entire sample when spun [21]. This multiplexing approach allows for a significant improvement in image quality, due to the rejection of out-of-focus light, while using cameras to achieve high frame rates. Spinning disk systems typically experience low excitation light throughput, which can increase the integration time required to obtain a quality image [22]. Furthermore, out of focus light rejection is limited particularly in thicker samples, since out-of-focus light can leak into adjacent pinholes [22]. The camera itself is also limited by its own noise sources, which are generally more significant than those of discrete single detectors. The cameras used in a spinning disk setup cannot be replaced with stationary single-point detectors, since the emission foci generated by the spinning disks are always moving. Furthermore, the high speed gated cameras required to record time domain information using a spinning disk system suffer from poor spatial resolution that many subcellular details are lost. This typically limits such systems to collecting intensity images.

Risi et. al. recently reported a modified line-scanning confocal microscope that was given true confocal capabilities by spinning a disk of radial slits perpendicular to the primary confocal slit [23]. This maintained the microscope's ability to provide a line output for a slit detector (e.g. spectrometer), though is still not suitable for point detection, as the disk does not descan the foci for a stationary point detector array.

To take full advantage of a multiplexed confocal approach, the detection may be made by discrete single-point detectors, which offer better signal-to-noise performance and temporal resolution than a CCD array [24]. For these methods, a foci array is generated by a lenslet array or spatial light modulator, and raster scanning is performed by the entire array [25, 26]. The de-scanning process, by which the emitted light from the sample returns through the same path, allows for fixed positioning of the discrete detectors. A number of different methods using a foci array to multiplex image acquisition have been reported where an array of up to 16 excitation beams is scanned across the sample (Nikon/Prairie Technologies) or the sample itself can be scanned relative to a static foci array by using a motorized microscope stage, though the latter approach is limited in speed and results in vibrations that are not ideal for live cell imaging [25, 27, 28].

We recently demonstrated a square multiple foci array scheme to achieve FLIM using a streak camera as a detector [28]. In this method, a two-dimensional (2D) foci array was generated by a lenslet array and relayed onto the sample plane. The fluorescence signal of each focal point is returned back through the dichroic, and collected by a matching 2D optical fiber array, which rearranges the fiber channels from a 10x10 arrangement into a one-dimensional (1D) 1x100 arrangement suitable for the slit of the streak camera. In that system, the sample was scanned using a motorized high-precision stage. For live cell imaging and HCS applications, an efficient and fast beam scanning technique is required. In this communication, we present the design and development of a novel array scanning technique that allows stationary foci array readout. This technique is implemented with a streak camera based multiplexing FLIM system to demonstrate its performance. It should be noted that the applications of such array scanning techniques are not limited to FLIM, but are useful to other confocal applications where stationary foci array readout is desired.

4.2. Mirror galvanometer scanning

The majority of current single beam confocal applications use mirror galvanometers to achieve raster scanning of the focal spot [4, 5, 24, 29]. A pair of orthogonal mirror galvanometers are used to tilt the trajectory of a light beam along two axes. The beam is then focused, at which point the tilt in the beam in each axis corresponds to a lateral spatial shift in the location at which the focus is generated. There is a nearly linear relation between tilt angle (ϕ) and lateral shift (Δd), which is also affected by the focal length of the focusing lens (f), as shown in Equation 4.1.

$$\Delta d = f \tan 2\phi \cong 2f\phi \tag{4.1}$$

Mirror galvanometers are also suitable for scanning an array of foci [29]. In this case, the foci array are collimated first, which converts each focal point to a collimated beam propagating at a given angle. Each scanning mirror is often placed between a pair of lenses or concave mirrors designed to take the foci array in and out of Fourier space [30]. This scheme requires a collimating lens and a focusing lens, hence the resulting relation becomes:

$$\Delta d = f \tan\left(\tan^{-1}\left(\frac{d_{in}}{f}\right) + 2\phi\right) - d_{in} \cong 2f\phi \tag{4.2}$$

In Equation 4.2, d_{in} is the starting height of the focal point, relative to the optical axis of the lens. The described mirror scanning scheme is shown in Figure 4-1(a).

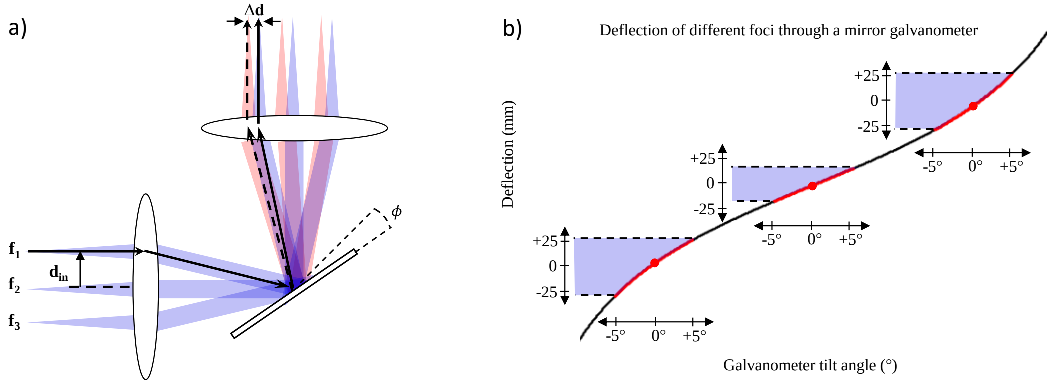

Figure 4-1: (a) Beam propagation of a foci array member din from the normal axis of the lens. The solid line path shows how the beam propagates when the mirror is at its initial position, 45° to each lens. The dashed line shows the beam path when the mirror has been tilted by φ. The lateral displacement is highlighted as Δd. (b) Plot of the deflection experienced by different foci (f_1, f_2, f_3) in a mirror galvanometer scanner. The curve shows an extreme case of non-linear response of deflection with tilt angle. Since the input foci are collimated at different angles relative to the mirror, they will experience different segments of the deflection response. Each red spot represents a different focal point when the galvo is in a neutral 45° position. The red line shows the range of motion of each output focal point as the galvanometer is tilted from -5° to +5°. The deflection range for each focal point over this same angle range is highlighted in blue, showing a larger range for the outer focal points compared to the central focal point.

While mirror galvanometers are capable of scanning an array of foci, divergence from the linear approximation begins to cause problems for high resolution scanning. Some of the collimated beams will be incident on the mirrors at large angles to the normal, causing non-linear scanning. This could also occur in a single beam mirror galvanometer scheme, but then the galvanometer angle steps could be adjusted to account for the non-linearity. When there are multiple beams, some of them will be in the linear scanning region, while some will be non-linear, causing different scan ranges for different foci array members. This foci-dependent non-linearity is demonstrated in Figure 4-1(b). To mitigate the non-linearity, lenses with a longer focal length can be used. This will have the effect of compressing the angle range to the linear region, while the required angular resolution is reduced in order to maintain the same lateral resolution. This can quickly approach the angular resolution limits of the galvanometer, typically in the range of 15 μrad (e.g., GVS412 2D large beam diameter galvo system, Thorlabs, Newton, NJ).

One possible solution for this would be to replace the lenses of the mirror galvanometer scanner system with f-theta lenses, also known as scanning lenses. As the name suggests, f-theta lenses are corrected to have a linear relationship with the angle of a collimated beam: a beam propagating at angle θ will be focused to a point on the focal plane, at a distance of $f \cdot \theta$ from the center. However, this requires the use of up to four f-theta lenses, one on either side of each mirror galvanometer increasing the cost of the scanning solution, which rises quickly with scanning field size and scanning aperture [31]. The addition of the scan lenses also adds several elements to the optical train, reducing the transmission efficiency and increasing the alignment complexity of the system. Both of which are of particular concern for high speed applications such as live cell imaging and HCS. While resolving the non-linearity issue, f-theta lenses do not manage to solve the tight angular resolution requirements inherent to mirror galvo systems. F-theta lenses have focal lengths in the range of 100 mm to 250 mm (e.g. FTH series f-theta lens, Thorlabs Inc., Newton, NJ). In order to achieve a pre-objective lateral step of 5 μm (or 250 nm after a 20x objective), a galvo scanner equipped with one of these f-theta lenses would need to take a 10-25 μrad step, which is at the limit of the galvanometer's tilt repeatability.

A spatial light modulator-based approach for generating the foci array was recently demonstrated in the FLIM-FRET domain on which galvanometer mirrors were used to scan the foci [26]. Poland et. al. were able to perform FLIM with very high temporal (150 ps) and spatial (0.8 μm) resolution at high throughput speeds (10 sec/FLIM image), though it does highlight some of the limitations of the mirror galvanometer scanning scheme. First, each galvanometer is placed between a pair of relay lenses. Second, as was mentioned earlier, the mirror scan resolution required would very quickly approach the repeatability limits of the scanner, where the smallest step size of 15 μrad would correspond with a scanning resolution of 0.3 μm at the sample plane (83 x 83 scan).

The QuadScanner is another mirror galvanometer implementation designed specifically for stimulated emission depletion microscopy [32]. Contrary to previously discussed mirror galvanometer scanners, the QuadScanner is implemented in the image space, on either side of the conjugate sample plane. Two mirror galvanometers are required for each axis, in order to shift the beams in the image plane while maintaining the collimated beam position in the pupil plane. This removes the requirement of expensive f-theta relay lenses, allowing for a more compact system. It can also achieve beam multiplexing, as long as all beams fit on the scanners throughout the scan. Since the scanner is in the image space, the lateral displacement is not governed by Equation 4.2, and so it is possible to achieve discrete lateral steps sizes on the scale of 0.2 μm before demagnification by the objective. The main drawback is the increase in the number of galvanometers, adding to the cost and complexity of the system.

4.3. Design of a window tilt scanning scheme

To relax the tilt resolution requirements, and reduce the number of optical components as well as the overall size of the multifocal mirror galvanometer, we developed an array scanning scheme using galvanometers mounted with flat windows to shift incident beams through refraction. Contrary to mirror galvanometers, window galvanometers do not require the foci array to be shifted into the Fourier domain. Through the use of basic refractive properties, a tilt (ϕ) in the window of refractive index n and thickness t will cause a lateral deflection (Δd) of the output beam according to Equation 4.3.

$$\Delta d = t\left[\tan\phi - \tan\left(\sin^{-1}\left(\frac{\sin\phi}{n}\right)\right)\right]\cos\phi \cong \phi t\left(\frac{n-1}{n}\right) \tag{4.3}$$

This relation is shown in Figure 4-2. As was the case in the mirror galvanometer equation, a small angle approximation can be made here as well, allowing for approximately linear translation with tilt angle.

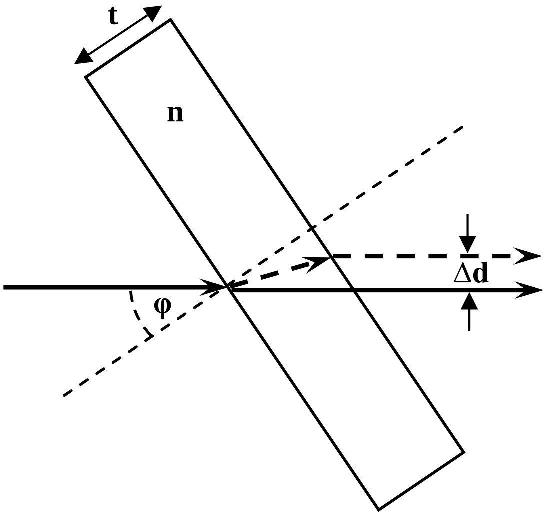

Figure 4-2: Beam propagation through a tilted glass. The solid line shows how the beam propagates when the window is normal to direction of propagation. The dashed line shows the beam path when the window has been tilted by φ.

As the scan relies on the small angle approximation, it will be vulnerable to the same nonlinearities at larger scan angles that the mirror tilt scheme experiences. The difference is that, since all of the members of the foci array are experiencing the same deflection nonlinearity, it is possible to correct this by adapting the angle step size at large angles.

One important distinction is that, even in the original non-approximated relationship, the lateral displacement Δd is not a function of the original location of the focal point. Therefore, this method will treat all foci equally, and the scan ranges will be inherently uniform. This makes the window galvanometer scheme especially well-suited for multiplexed beam scanning.

The refractive scan has a number of linear tuning parameters, most notably the window thickness. The window material and full scan angle can also be used to tune the lateral deflection of the output foci. In contrast, the mirror tilt scheme essentially requires that all of the possible angles that the collimated beams make to the normal of the mirror are within the small angle approximation range. This means that the scan angle will be small, and the scan step angle could approach the angle resolution of the scanner. The window tilt can be over much larger scan angles, allowing the system to relax the angle resolution requirements of the scanners.

There is also a reduction in the complexity of the optical system. The mirror tilt scheme requires lenses or concave mirrors to convert to and from the Fourier domain. Furthermore, typically two sets of lenses/mirrors are needed to ensure that each galvanometer mirror can be at a Fourier plane. The window tilt scheme does not require any additional lenses, as long as all of the beams can still fit on the two successive windows. As a result, the system can achieve higher throughput than a similar mirror-galvanometer system. A multifocal mirror galvanometer system, with two coated mirrors (e.g. GVS011 silver-coated, Thorlabs Inc., Newton, NJ) and two scan lenses (e.g. FTH100-1064 visible AR coating, Thorlabs Inc., Newton, NJ) is calculated to have a round-trip efficiency through the scanner of 61%. Alternatively, a window galvanometer system comprised of two AR-coated fused silica windows (e.g. UVFS windows AR-A coating, Thorlabs Inc., Newton, NJ) is calculated to have a round-trip efficiency of 95%. This is particularly important for multiplexing scenarios, where the laser’s power is already divided between the foci.

4.4. Results and discussion

To study the effectiveness of the refractive window tilt scheme in scanning a foci array, we integrated two scanners into a square foci array set up shown in Figure 4-3. A 10 x 10 region of a 20 x 20 lenslet array (18-1453-100-000, 500 μm pitch, square lenslets, SUSS MicroOptics, Neuchâtel, Switzerland) was used to generate the foci array. Based on the pitch of the lenslets, in order for the foci array to reach every point of the sample, each scanner must allow for ± 250 μm lateral deflection. If the galvanometers are fitted with fused silica ($n = 1.47$) windows of thickness 5 mm, this lateral deflection can be accomplished with a tilt angle of ± 8.9°. The galvanometer heads used for the experiment are capable of ± 10°, or ± 280 μm.

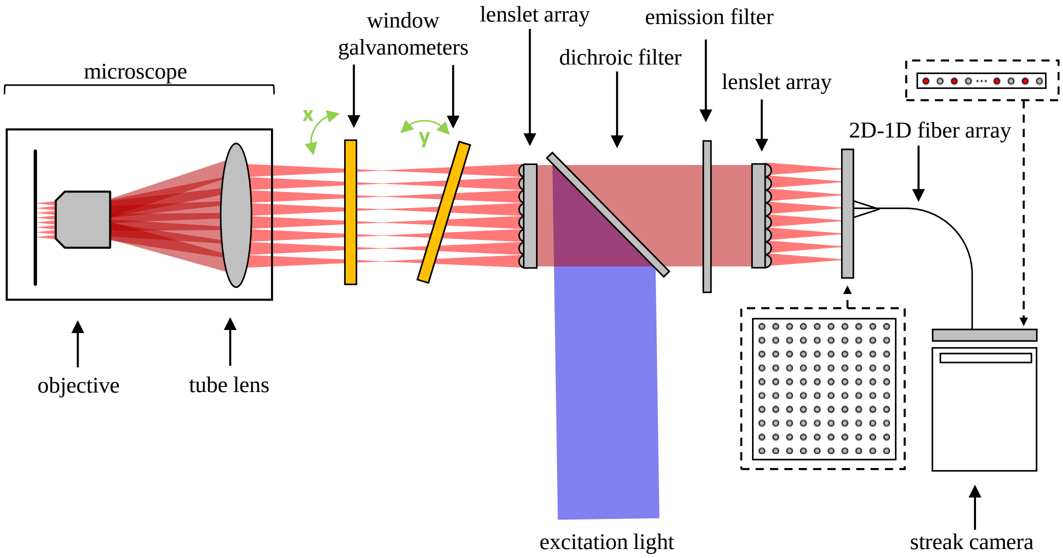

Figure 4-3: Instrument setup for multiplexed FLIM, using window galvanometer scanners.

The setup uses a 440 nm diode laser (3 mW, 60 ps LDH-P-C-440M, PicoQuant, Berlin, Germany) as the excitation source, which is reflected off a 445 nm dichroic filter (Di01-R442-25 × 36, Semrock, Rochester, New York) into the first lenslet array. The lenslet array generates the foci array, which is subsequently scanned by the two window galvanometers (6230HM40B, Cambridge Technology, Cambridge, Massachusetts) along the two principal axes. The image of the shifted foci array is relayed into an inverted fluorescence microscope (Axiovert 200, Carl Zeiss, Oberkochen, Germany) onto the sample by a 20x objective. Fluorescent light generated at each excitation focal point is reversed through the system, undergoing an inverted shift back into alignment with the lenslet array. The lenslet array re-collimates the light before a second lenslet array (18-1531-100-000, 500 μm pitch, square lenslets, SUSS MicroOptics) refocuses the channels into a foci array on a custom 2D fiber array of matching pitch (0.11 NA, fused silica, n = 1.44, 50 μm diameter core, 125 μm diameter cladding. This fiber array acts effectively as a stationary array of single detectors, and so permits multiplexing that cannot be accomplished with a spinning disk confocal system. The fiber cores also act as an array of pinholes, through which the multiplexed image can become confocal. The fibers of the 2D fiber array are rearranged from 10 x 10 to a 1 x 100 line of fibers, suitable to couple to the input slit of the streak camera (SC-10, Optronis GmbH, Kehl, Germany), where the fluorescence decay of each channel can be observed in the readout camera (SRU-ED 16-bit mono, Optronis GmbH, Kehl, Germany). The 2D-1D fiber array has been reported previously [28].

The streak camera runs at 40 MHz repetition rate, synchronized to the pulsed diode laser driver, and a relative delay is employed in order to properly center the fluorescence decay streaks on the readout. By coupling the input with 50 μm core fibers, the time resolution of the streak camera can be as low as 20 ps. However, the system response function is limited by the relatively long pulse width of the diode laser, which is on the order of 100 ps. The readout camera can acquire frames up to a rate of 100 fps. This is the current bottleneck for how quickly a scan can be performed.

One concern with a refractive scanning solution for fluorescence imaging is how the scanning will vary with wavelength. If there is a significant enough change in refractive index, the fluorescent light will not be descanned properly. Fused silica was selected as the window material due to its low chromatic dispersion in the visible range. For the window parameters selected, excitation light at 440 nm ($n = 1.46635$) will allow ± 250 μm at 8.92°. As a worst case scenario, if 700 nm ($n = 1.45529$) light is generated and returns through the system, it will be scanned back ± 246 μm, meaning there will be a descanning deviation of up to 4 μm. Even in this extreme case, the deviation is small compared to the size of the single point detectors. In our case, the single point detector array is the 2D fiber array, where the core diameter of 50 μm will make this deviation insignificant. Similarly, this means that the scanning scheme can be applied to multiple excitation sources with minimal chromatic deviation between scan positions.

The window scanning galvanometer was first tested in the setup shown in Figure 4-4(a), to assess uniformity and linearity. In this case, uniformity is described as how similar different foci move as they travel through the scanner, and linearity describes how linearly the beam is deflected versus tilt angle. The beam of a diode laser (PicoQuant LDH-510) was expanded to illuminate a lenslet array (1 mm pitch) to generate the foci array. A window galvanometer placed in the image plane of the foci array, caused the lateral shift. The image was then relayed onto a CCD (Qimaging QICAM 10-bit mono, Surrey, BC, Canada). Successive images were collected at different window tilt angles to measure the lateral displacement of the foci relative to their mean scan positions. The relative displacements were used to create an ensemble to test the uniformity of the displacement.

Each spot was located as the center of mass of the surrounding pixels (Figure 4-4(b)). This creates a collection of spot locations for each fiber at each tilt angle step. By subtracting each fiber spot set by the mean value of the scan, the sets are normalized and can be compared to each other (Figure 4-4(c)). By taking the ensemble average of all foci, there is an inter-spot variability of ± 1.6 μm (at 95% confidence). While already very small, this variability is very likely due to limitations in centroiding given the pixel size of the readout camera, which is 4.65 x 4.65 μm^2.

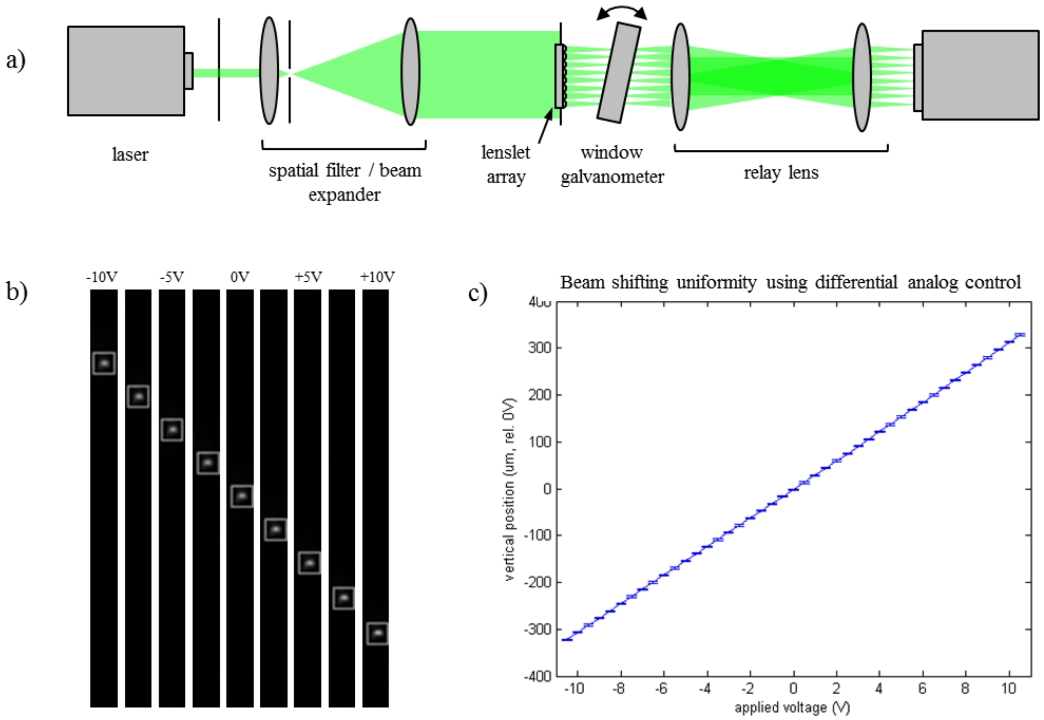

Figure 4-4: (a) Experimental setup for testing the linearity and uniformity of the window tilt scanning scheme. (b) Readout images of single beam spot as the differential voltage across the galvanometer is changed. (c) Plot of the relative vertical position of 24 foci as they are scanned, with 95% confidence intervals included for each data point.

The linearity of the scan was >99.99% against a line of best fit, with a maximum deviation from the best fit of 5 μm. Therefore, due to the small angle approximation region, the window galvanometer can be driven with uniform step spacing to obtain suitably linear deflection. If the tilt range exceeded the small angle approximation region, or if better precision were required, a non-uniform stepping scheme could be used. Since all the spots would still scan identically to each other, there would never be the uniformity concerns that arise with the mirror galvanometer scheme.

The window galvanometer raster scan was used to image a fixed *Convallaria* specimen. The image shown in Figure 4-5 is comprised of 100 raster-scanned squares stitched together. There are a few regions of the image where the boundaries of the squares can be visualized, due to artifacts arising from manufacturing errors in the fiber array (e.g. three dead fibers led to three black squares – highlighted by the white square outlines, and alignment with respect to the lenslet array). These problems are not unique to the window galvanometer

solution, and can be solved through more precise optomechanics or through reconstruction corrections.

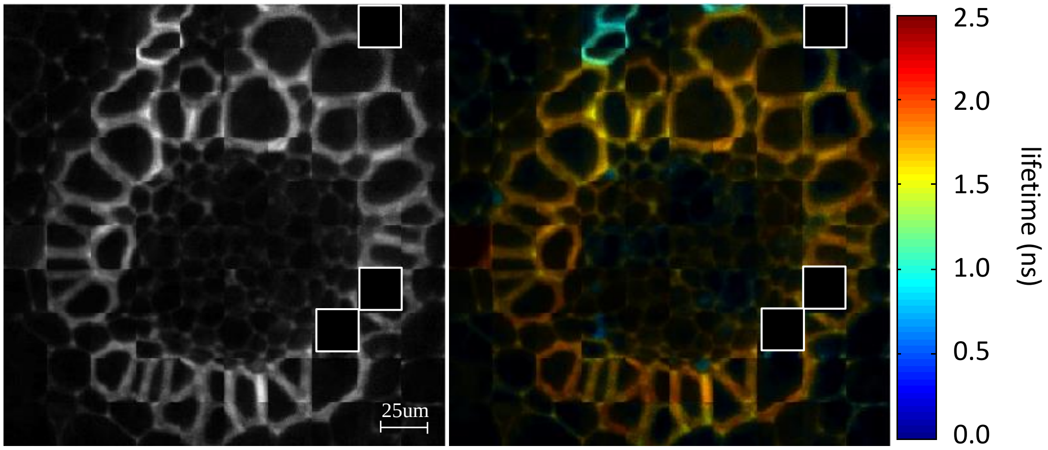

Figure 4-5: Intensity (left) and lifetime (right) reconstructions of *Convallaria* sampled after a 30 x 30 raster scan with the window galvanometers. Dark regions outlined in white indicate the scan regions of channels that were not collected due to dead fibers in the fiber array.

The *Convallaria* image shown in Figure 4-5 is comprised of 100 raster-scanned squares stitched together. There are a few regions of the image where the boundaries of the squares can be visualized, due to artifacts arising from manufacturing errors in the fiber array (e.g. three dead fibers led to three black squares – highlighted by the white square outlines, and alignment with respect to the lenslet array). These problems are not unique to the window galvanometer solution, and can be solved through more precise optomechanics or through reconstruction corrections.

The sample image was collected at a 30 x 30 scan. The angle step size used was 11.6 mrad, though the galvanometer head itself has a repeatability of 8 μrad. Therefore, our window galvanometer system does not come close to reaching the possible resolution limits. Due to the noise level in the electronic signal, the galvanometer head is limited to 2000 resolvable steps, meaning it is possible to perform a 20,000 x 20,000 scan. In our implementation, this would correspond to an angular step size of 174 μrad, providing a 0.25 μm lateral step size – before the objective. After a 20x objective, the step size at the sample is effectively 13 nm. Therefore, the resolution of the reconstructed image will not be limited by the window galvanometer even for super-resolution imaging techniques with higher resolution than optical diffraction.

For test purposes the galvanometer head was operated in step mode, though it can be run with linear motion as well. In step mode, it takes a single step in 700 μs. This means that a 30 x 30 scan is possible in 630 ms. If the fast axis were scanned continuously instead of by step, without considering the rest of the system, the galvo is capable of performing a line scan in 2.5 ms, and so a 30 x 30 scan could be performed in 75 ms. Thus using window galvanometers data collection for virtually any application will not be limited by the scan speed. Instead, in our FLIM set up acquisition is limited by the camera readout time of 10 ms per frame. Due to the frame rate, a 30 x 30 scan of the 10 x 10 foci (corresponding to final reconstructed image area of 300 x 300 pixels and 700 pixels in time) requires 900 readout frames, taking at least 9 seconds, or effectively 0.1 ms per FLIM data point. By comparison, collection of a TCSPC image of 256 x 256 area and 256 pixels in time requires approximately 45 seconds using avalanche photodiodes, or 0.7 ms per FLIM data point. Our benchmark of 1 FLIM image per second could be achieved by further multiplexing the streak camera, such that fewer readout frames are required for a scan of equal size.

4.5. Conclusion

In summary, we presented a novel but simple window galvanometer scheme for multiplexed scanning schemes with stationary detectors. This technique exhibited perfect uniformity and excellent linearity over the scan range, and is easily scalable to further multiplexing. The choice of window material and thickness provide an accurate way to tune the scanner’s sensitivity to tilt angle. The scheme does not require any additional scan lenses, saving in size, complexity, throughput and cost, making it possible to add multiplexing confocal capability to any existing wide-field microscope. The lateral translation is also significantly less sensitive to tilt angle, which means the tolerance on tilt angle resolution can be relaxed. Conversely, operated at the angular resolution limits of the scanner, the window tilt scheme is capable of high resolution scans far below the optical diffraction limit.

While our implementation of this scanning scheme has been limited to FLIM applications and temporal detection, a window galvanometer offers the same advantages for any other imaging modality that could be improved by single-point detector arrays. For instance, multiplexed hyperspectral imaging could be performed using a similar 2D-1D fiber array fitted to a spectrometer slit. It is also an attractive option for the emerging capabilities of single-photon avalanche diode arrays [33], which could be used for low-light and time-of-flight imaging.

Acknowledgements

This project is supported in part by the Ontario Centres of Excellence through a Phase IIa Market Readiness grant to QF and DWA as well as CIHR grant FRN-10490 to DWA. AT holds the NSERC Industrial Postgraduate Fellowship. QF holds the Canada Research Chair in Biophotonics.

References

[1] D. M. Shotton, "Confocal scanning optical microscopy and its applications for biological specimens," *Journal of Cell Science,* vol. 94, p. 175, 1989.

[2] J. Art, "Photon Detectors for Confocal Microscopy," in *Handbook of Biological Confocal Microscopy*, New York, Springer, 2006, p. 251.

[3] K. Suhling, P. M. French and D. Phillips, "Time-resolved fluorescence microscopy," *Photochemical and photobiological sciences,* vol. 4, no. 1, p. 13, 2005.

[4] L. Liu, J. Qu, Z. Lin, Z. Fu, B. Guo and H. Niu, "Simultaneous time- and spectrum-resolved multifocal multiphoton microscopy," *Applied Physics B,* vol. 84, pp. 379-383, 2006.

[5] S. Kumar, C. Dunsby, P. A. A. De Beule, D. M. Owen, U. Anand, P. M. P. Lanigan, R. K. P. Benninger, D. M. Davis, M. A. A. Neil, P. Anand, C. Benham, A. Naylor and P. M. W. French, "Multifocal multiphoton excitation and time correlated single photon counting detection for 3-D fluorescence lifetime imaging," *Optics Express*, vol. 15, pp. 12548-12561, 2007.

[6] W. R. Zipfel, R. M. Williams and W. W. Webb, "Nonlinear magic: multiphoton microscopy in the biosciences," *Nature Biotechnology,* vol. 21, no. 11, p. 1369, 2003.

[7] S. W. Hell and J. Wichmann, "Breaking the diffraction resolution limit by stimulated emission: stimulated-emission-depletion fluorescence microscopy," *Optics Letters,* vol. 19, no. 11, p. 780, 1994.

[8] M. Straub, P. Lodemann, P. Holroyd, R. Jahn and S. W. Hell, "Live cell imaging by multifocal multiphoton microscopy," *European Journal of Cell Biology,* vol. 79, p. 726, 2000.

[9] M. Bickle, "The beautiful cell: high-content screening in drug discovery," *Analytical and Bioanalytical Chemistry,* vol. 398, no. 1, p. 219, 2010.

[10] D. M. Grant, W. Zhang, E. J. McGhee, T. D. Bunney, C. B. Talbot, S. Kumar, I. Munro, C. Dunsby, M. A. A. Neil, M. Katan and P. M. W. French, "Multiplexed FRET to image multiple signaling events in live cells," *Biophysical Journal*, vol. 95, pp. L69-L71, 2008.

[11] P. Lang, K. Yeow, A. Nichols and A. Scheer, "Cellular imaging in drug discovery," *Nature Reviews Drug Discovery,* vol. 5, pp. 343-356, 2006.

[12] J. R. Lakowicz, "Energy Transfer," in *Principles of Fluorescence Spectroscopy,* New York, Springer, 2006, pp. 443-475.

[13] A. Aranovich, Q. Liu, T. Collins, F. Geng, S. Dixit, B. Leber and D. W. Andrews, "Differences in the Mechanisms of Proapoptotic BH3 Proteins Binding to Bcl-XL and Bcl-2 Quantified in Live MCF-7 Cells," *Molecular Cell,* vol. 45, no. 6, p. 754, 2012.

[14] E. J. Osterlund, Q. Liu and D. W. Andrews, "The use of FLIM-FRET for the detection of mitochondria-associated protein interactions," in *Mitochondrial Medicine I: Probing Mitochondrial Function*, New York, Springer, 2015, pp. 395-419.

[15] A. Esposito, H. C. Gerritsen and F. S. Wouters, "Optimizing frequency-domain fluorescence lifetime sensing for high-throughput applications: photo economy and acquisition speed," *Journal of the Optical Society of America A,* vol. 24, pp. 3261-3273, 2007.

[16] S. Wachsmann-Hogiu, D. Krakow, V. T. Kirilova, D. H. Cohn, C. Bertolotto, D. Acuna, Q. Fang, N. Krivorov and D. L. Farkas, "Multiphoton, confocal, and lifetime microscopy for molecular imaging in cartilage," in *SPIE Proceedings 5699*, San Jose, CA, 2005.

[17] A. V. Agronskaia, L. Tertoolen and H. C. Gerritsen, "High frame rate fluorescence lifetime imaging," *Journal of Physics D: Applied Physics,* vol. 36, pp. 1655-1662, 2003.

[18] C. Buranachai, D. Kamiyama, A. Chiba, B. Williams and R. M. Clegg, "Rapid frequency-domain FLIM spinning disk confocal microscope: lifetime resolution, image improvement and wavelet analysis," *Journal of Fluorescence,* vol. 18, pp. 929-942, 2008.

[19] S. E. Webb, Y. Gu, S. Lévêque-Fort, J. Siegel, M. J. Cole, K. Dowling, R. Jones and P. M. French, "A wide-field time-domain fluorescence lifetime imaging microscope with optical sectioning," *Review of Scientific Instruments,* vol. 73, no. 4, p. 1898, 2002.

[20] E. B. van Munster, J. Goedhart, G. J. Kremers, E. M. M. Manders and T. W. J. Gadella, "Combination of spinning disk confocal unit with frequency-

domain fluorescence lifetime imaging microscopy," *Cytometry Part A,* vol. 71, no. 1, pp. 207-214, 2007.

[21] E. Wang, C. M. Babbey and K. W. Dunn, "Performance comparison between the high speed Yokogawa spinning disc confocal system and single-point scanning confocal systems," *Journal of Microscopy,* vol. 218, pp. 148-159, 2005.

[22] D. Toomre, "Disk-Scanning Confocal Microscopy," in *Handbook of Biological Confocal Microscopy,* New York, Springer, 2006, p. 221.

[23] M. D. Risi, H. Makhlouf, A. R. Rouse, A. A. Tanbakuchi and A. F. Gmitro, "Design and performance of a multi-point scan confocal microendoscope," *Photonics,* vol. 1, no. 4, p. 421, 2014.

[24] K. H. Kim, C. Buehler, K. Bahlmann, T. Ragan, W.-C. A. Lee, E. Nedivi, E. L. Heffer, S. Fantini and P. T. C. So, "Multifocal multiphoton microscopy based on multianode photomultiplier tubes," *Optics Express,* vol. 15, pp. 11658-11678, 2007.

[25] A. Chmyrov, J. Keller, T. Grotjohann, M. Ratz, E. d'Este, S. Jakobs, C. Eggeling and S. W. Hell, "Nanoscopy with more than 100,000 ‘doughnuts’," *Nature Methods,* vol. 10, pp. 737-740, 2013.

[26] S. P. Poland, N. Krstajić, J. Monypenney, S. Coelho, D. Tyndall, R. J. Walker, V. Devauges, J. Richarson, N. Dutton, P. Barber, D. D.-U. Li, K. Suhling, T. Ng, R. K. Henderson and S. M. Ameer-Beg, "A high speed multifocal multiphoton fluorescence lifetime imaging microscope for live-cell FRET imaging," *Biomedical Optics Express,* vol. 6, no. 2, p. 277, 2015.

[27] T. Nielson, M. Fricke, D. Hellweg and P. Andresen, "High efficiency beam splitter for multifocal multiphoton microscopy," *Journal of Microscopy,* vol. 201, pp. 368-376, 2001.

[28] A. Tsikouras, J. Ning, S. Ng, R. Berman, D. W. Andrews and Q. Fang, "Streak camera crosstalk reduction using a multiple delay optical fiber bundle," *Optics Letters,* vol. 37, pp. 250-252, 2012.

[29] L. Sacconi, E. Froner and R. Antolini, "Multiphoton multifocal microscopy exploiting a diffractive optical element," *Optics Letters,* vol. 28, pp. 1918-1920, 2003.

[30] W. B. Amos and J. G. White, "How the confocal laser scanning microscope entered biological research," *Biology of the Cell,* vol. 95, pp. 335-342, 2003.

[31] J. Xie, S. Huang, Z. Duan, Y. Shi and S. Wen, "Correction of the image distortion for laser galvanometric scanning system," *Optics and Laser Technology*, vol. 37, pp. 305-311, 2005.

[32] F. Gürlitz, P. Hoyer, H. J. Falk, L. Kastrup, J. Engelhardt and S. W. Hell, "A STED microscope designed for routine biomedical applications," *Progress in Electromagnetics Research,* vol. 147, pp. 57-68, 2014.

[33] C. Cammi, A. Gulinatti, I. Rech, F. Panzeri and M. Ghioni, "SPAD array module for multi-dimensional photon timing applications," *Journal of Modern Optics,* vol. 59, no. 2, p. 131, 2012.

Chapter 5

Paper III – Characterization of SPAD array for multifocal high-content screening applications

Anthony Tsikouras[1], Pietro Peronio[2], Ivan Rech[2], Nehad Hirmiz[3], M. Jamal Dean[4] and Qiyin Fang[1,3,*]

[1] *Department of Engineering Physics, McMaster University, 1280 Main Street West, Hamilton, Ontario, L8S 4L7, Canada*

[2] *Dipartimento di Elettronica, Informazione e Bioingegneria, Politecnico di Milano, 20133 Milano, Italy, L8S 4L7, Canada*

[3] *Department of Biomedical Engineering, McMaster University, 1280 Main Street West, Hamilton, Ontario, L8S 4L7, Canada*

[4] *Department of Electrical and Computer Engineering, McMaster University, 1280 Main Street West, Hamilton, Ontario, L8S 4L7, Canada*

Published in MDPI Photonics; 6(10):3737-3747, 2015

Introduction to Paper III

This chapter describes the exploration of a 32-channel single-photon avalanche diode (SPAD) array with an aim for determining how well a future 32 x 32 SPAD array could serve our multifocal high-content screening (HCS) system. As SPAD arrays are emerging as a leading contender for the next generation of fluorescence lifetime imaging microscopy (FLIM), the characterization of the SPAD array for this application could be a first step towards replacing the streak camera in our setup.

In this work, existing performance characteristics of the SPAD array are evaluated with respect to the requirements of the HCS FLIM application. A function is developed to relate the various SPAD noise sources to the resulting increase in noise in fluorescence decays when compared to an ideal shot-noise-only scenario. Fluorescence lifetime measurements were done using a known standard at varied number of counts collected, to determine the impact of lower count rates on lifetime estimation. Calculations were also performed to estimate the readout speed of the 32 x 32 SPAD array design in order to determine how it could be made suitably high throughput to meet the demands of high-throughput screening.

This works shows the future promise of the emerging SPAD array devices, which should be a solid improvement on the streak camera in terms of photon detection efficiency, noise performance and degree of multiplexing. This paper acts as a bridge between the disciplines of SPAD array development and FLIM applications, and so the targeted audience includes researchers from both disciplines. This manuscript was prepared by me and revised by the coauthors.

Contents of Paper III

Abstract

Current instruments used to detect specific protein-protein interactions in live cells for applications in high-content screening (HCS) are limited by the time required to measure the lifetime. Here, a 32 × 1 single-photon avalanche diode (SPAD) array was explored as a detector for fluorescence lifetime imaging (FLIM) in HCS. Device parameters and characterization results were interpreted in the context of the application to determine if the SPAD array could satisfy the requirements of HCS-FLIM. Fluorescence lifetime measurements were performed using a known fluorescence standard; and the recovered fluorescence lifetime matched literature reported values. The design of a theoretical 32 × 32 SPAD array was also considered as a detector for a multi-point confocal scanning microscope.

5.1. Introduction

In drug discovery, one of the most time-consuming stages is the identification of candidate drugs. Modern high-content screening (HCS) microscopes process thousands of living cell samples, which have been treated with varied dosages of drug leads. The resulting images are analyzed by advanced algorithms to determine the drug effectiveness and dosage optimization [1]. These results are analyzed for imaging phenotypes related to the cell's morphology and proliferation rate, as a means of determining the underlying reaction to the drug [2]. While important discoveries can be made through these phenotypes, it is impossible to determine the exact nature of how the drug is affecting the cell line.

Inside a cell, a complex interaction network of proteins exists to maintain homeostasis and regulate cell behavior [3]. Whether it is two proteins binding to each other or multiple proteins forming an oligomer, these protein-protein interactions happen at the scale of a few nanometers: far below the optical diffraction limit. Consequently, such interactions are invisible in morphological high-content screening. More insight can be obtained if a more direct approach to monitoring protein-protein interactions is used in HCS. Such techniques use existing information of these interactions, as well as their biological pathways, to enable a better understanding of how the drug works, as well as the side effects. One such directed approach is to use Förster resonance energy transfer (FRET), which offers the ability to qualitatively and quantitatively monitor molecular interactions at nanometer scales. FRET is a phenomenon whereby an excited "donor" fluorophore non-radiatively transfers its excitation energy to a nearby "acceptor" fluorophore, which then fluoresces as it returns to the ground state. The proximity of the two fluorophores must be on the scale of <10 nm, which makes it suitable for tagging a specific protein-protein interaction [4]. While FRET can be monitored, to some degree, by measuring the ratio of donor emission to acceptor emission ("intensity FRET"), this method has complications, due to the differing local populations of donor and acceptor fluorophores and spectral bleeding effects between the excitation and emission spectra of the FRET pair [4, 5]. Polarization-resolved FRET can be performed with a very good signal-to-noise ratio [6], but is complicated by losses and distortions due to polarization [7]. It also is not good at distinguishing between varying degrees of FRET [7].

Fluorescence lifetime imaging microscopy can measure FRET (FLIM-FRET), through monitoring the reduction in the fluorescence lifetime of the donor fluorophore. FLIM-FRET does not have the abovementioned complications, making it a more accurate measure of FRET activity—subsequently protein-protein interaction—within the cell. At the same time, fluorescence lifetime is also inherently more challenging to measure, however, since the targeted lifetimes are on the scale of 1–10 ns and the requirement of resolving the lifetime changes to a few hundreds of picoseconds. Furthermore, each pixel of an image could have many of the proteins of interest with differing degrees of FRET interaction. In the simplified case where both interacting and non-interacting fluorophores contribute to the same pixel, the fluorescence signal of the pixel would be a biexponential decay [8].

Time-correlated single-photon counting (TCSPC) is the gold standard by which FLIM is performed [9]. The principle is to measure the arrival times of each photon with very high precision, and form a histogram of arrival times as the fluorescence decay curve. This method requires the use of very low emission light levels in order to ensure that only a maximum of one photon arrives for each repetition, with the rule-of-thumb being a collection rate never exceeding 5% of the repetition rate [10]. Dividing the signal between multiple detectors and TCSPC circuits can proportionally improve the maximum allowable collection rate [11]. The method uses a raster scanning (confocal or multiphoton) approach, where each spot of the image is measured sequentially, with the signal being collected by a photomultiplier tube or single-photon avalanche diode (SPAD) [12]. Understandably, this makes TCSPC a challenge to apply to HCS, where a high priority is placed on acquisition throughput.

FLIM is also measured by time-gated imaging, where intensified charge-coupled device imagers (ICCDs) are made active for only a short time window [10, 13].

By measuring multiple time windows over repeated excitations, an approximation of the fluorescence lifetime curve can be generated. Due to the large gate width (>300 ps), the ICCD gating is not able to achieve a suitably high time resolution in order to separate the components of biexponential decays. Typically, this technique only measures two time windows, and uses their ratio to measure an average fluorescence lifetime [13]. For a biexponential fluorescence decay, this is not ideal in determining the ratio of binding to non-binding FRET pair populations measured from a spot in the image. It is also a wide-field imaging technique, which not only affects the ability to resolve subcellular features, but also means that each decay represents a larger volume of the sample (including out-of-focus contributions), greatly reducing the precision of the FRET measurement [14]. Finally, it is a slow technique, due to the rejection of photons arriving outside of the time window, and the inherently low quantum efficiency of the image intensifier. FLIM can also be measured through frequency domain analysis. In its most common implementation, a modulated ICCD is used to collect phase and attenuation information at different frequencies [15], but this method suffers similar drawbacks as the time-domain gated-ICCD approach discussed previously.

While gated imaging and other analog approaches are faster and can be easier to implement, TCSPC is the most sensitive method of acquiring fluorescence decays, due to the discrete photon-counting nature that offers excellent signal-to-noise ratios [16]. This is especially important in the case of live cell imaging, where the number of available photons in severely limited because low illumination intensities must be used since fluorophores are irreversibly photobleached after excitation [17].

In order to achieve a suitable effective spatial resolution and optical sectioning, confocal (or multiphoton) scanning fluorescence microscopy is required for measuring protein-protein interactions by FLIM-FRET [18]. While laser scanning can be performed very quickly and accurately, the time to acquire a confocal scan is limited by the collection time: the pixel dwell time must be set such that sufficient emitted light is collected at each spot in the image. While the laser power could be increased, in order to reduce the required dwell time, a very high laser irradiance could lead to photobleaching and photodamage of the specimen. Furthermore, if time-resolved data is being collected by TCSPC, the emitted photon collection rate must be kept below 5% of the laser repetition rate in order to prevent pulse pileup distortions in the fluorescence decay curve. This further limits the maximum laser power that could be used for sample illumination.

As an example, a 256 × 256 FLIM image, requiring 10,000 counts per pixel for suitable biexponential fitting, would then need 655 × 106 photon counts. At a

40 MHz repetition rate—the repetition rate best matched for the range of biological fluorescence lifetimes—the highest collection rate would be 2 Mcps (5% of 40 MHz). Therefore, the image would take nearly 330 s to acquire. The goal for high-throughput screening, however, is typically benchmarked to be 100,000 assays per day, or one acquisition per second [19].

If the speed of confocal imaging cannot be improved by increasing the excitation energy, the alternative would be to parallelize the confocal process. By employing multiple foci to scan across the sample, the laser power for each focal spot could be kept low to protect against photodamage and remain TCSPC-friendly, but the combined excitation at the sample plane can be much higher. The imaging speed of a system like this would then scale with the number of excitation foci. An additional benefit to using lower laser powers is that a single sample can be imaged repeatedly without photobleaching. This allows for the creation of a timelapse sequence capturing the dynamics of protein-protein interactions.

The main challenge of achieving multiplexed FLIM has been in the lack of a suitable detection module capable of sub-nanosecond response as well as digitization of such fast signals. Photomultiplier tubes (PMT) are the most commonly used detectors for single-photon counters, but they are generally too large and expensive to implement in a large parallel detection scheme [20]. PMTs typically have an active area diameter of 8 mm or larger and further miniaturization is limited since a great deal of their assembly is done manually.

The largest commercially available multi-anode PMT that has been implemented for TCSPC has 16 channels and a total active area of 16 × 16 mm2 (Becker and Hickl PML-16, Berlin, Germany). In this instrument, count signals from the 16 anodes are routed to eight TCSPC channels. Another research group [21] has been developing microchannel plate (MCP) PMTs with a multi-anode readout of 32 × 32 pixels, though this is still under development. MCP PMTs have the advantage that they are already greatly multiplexed due to their pore structure, and their low transit time spread gives them the best temporal resolution among TCSPC detectors. However, interfacing between the anodes and the TCSPC electronics has proven difficult. Recently, a wide-field approach to TCSPC was developed using an MCP PMT with a crossed delay line anode detector for spatially resolving each photon count [22]. This technique has the benefit of making TCSPC achievable in non-scanning setups, making it suitable for techniques such as light-sheet microscopy and total internal reflection microscopy. However, it can only achieve the collection rate of a single PMT. Since it is not actually a multiplexed solution, there is no gain in throughput and it is not a solution for HCS.

The possibility of multiplexing is now feasible with the advent of solid-state detector arrays specially designed for time-resolved imaging. There are a number of research groups actively pursuing integrated circuit detector arrays that are capable of creating hundreds to thousands of independent time-resolved pixels. A large number of these efforts involve the use of SPAD arrays using TCSPC [23, 24, 25, 26], while there are a few on-board time-gating approaches [27, 28, 29].

In addition to the clear advantages of size and scalability, SPADs match or outperform PMTs in other aspects. Their time resolution, usually determined by the transit time spread of a detected photon, is on the scale of 50 ps, compared to 100 ps or longer in conventional PMTs [19, 20]. However, MCP PMTs are indeed capable of a shorter transit time spread [30]. Silicon-based SPADs are also more efficient and well-tuned to the emission range of biological fluorophores: such SPADs have a quantum efficiency of nearly 50% at 500 nm, while it is less than 20% for a PMT [31, 32]. Hybrid PMT-SPAD detectors with a GaAsP photocathode are capable of 50% peak quantum efficiency as well, though these are costly and have not yet been developed into an array [33]. Possibly the most significant benefit to a SPAD array is low cost, as integrated circuits are significantly cheaper to manufacture than vacuum-tube technology.

We have previously designed a multiplexed confocal setup [34, 35], which uses a microlens array to generate a grid of foci. A galvo-mounted window is used to raster scan the foci across the sample, and then de-scan the returning emission light back in line with the microlenses. The returning light that transmits through the dichroic filter is collimated, but spatially encoded by the different lenslet channels. A single pinhole is used to achieve confocality for all of the channels, before the light is collimated once more, then separated into foci by a second microlens array. The end result is that we have a multifocal confocal setup in which the emission foci at the detector plane remain stationary. This means that discrete stationary detectors can be used to collect the signals, unlike spinning disk confocal setups where the emission foci are painted across an imaging sensor.

By placing a SPAD array at the detector plane, it would be possible to create a high-speed confocal imager with very high temporal resolution. Since the TCSPC process is multiplexed, the acquisition time would no longer be limited to prevent pulse pile-up distortions. In this project, we explored the possibility of implementing a custom-made SPAD array with an integrated TCSPC chip for HCS FLIM. Based on the performance of a 32 × 1 channel SPAD array, we determine that the future development of a 32 × 32 channel array would be suitable for achieving high-speed FLIM.

5.2. Materials and methods

5.2.1. Requirements for FLIM

It is difficult to state the de facto requirements for FLIM, since it can be very dependent on the particular sample, selection of fluorophore, and feature of interest. For instance, if the fluorescence lifetime quenching is significant enough, then an average lifetime measure could be sufficient to determine the FRET efficiency. Similarly, if the features of interest in the sample are relatively large, TCSPC histograms from each pixel of the feature can be binned together, meaning that fewer counts are required per pixel in order to get a good fit. Finally, the required field-of-view and spatial resolution also depend on the sample of interest.

For the sake of comparison, we will narrow the discussion to a typical case, where a 100× immersion objective is used. The pitch between foci in our experimental setup is 400 μm. With a 32 × 32 array of foci, the field of view at the microscope input is 12.8 × 12.8 mm—roughly the input aperture limit of commercial microscope side ports. After the 100× objective, this translates to a 128 × 128 μm field-of-view at the sample, with a foci pitch of 4 μm. To achieve 0.5 μm resolution, a 16 × 16 raster scan is required, meaning 256 scan acquisitions are needed to collect the entire FLIM image—which would have a pixel resolution of 512 × 512.

Since each SPAD would be responsible for collecting a 16 × 16 subset of this image, it would need to collect each TCSPC histogram in 3.9 ms. If approximately 10,000 counts are required in order to fit a biexponential decay, then each SPAD should be capable of collecting at least 10,000 counts at each scan position, which works out to 2.56 Mcps.

The required temporal resolution is also specific to the experiment, and depends on both the fluorescence lifetime range of the fluorophores present, and the impulse response function (IRF) of the excitation source. For ultrashort laser pulses, such as a Ti:sapphire laser, the laser pulse can be considered an ideal impulse, and so its pulse shape will not impact the fluorescence decay. In the case of diode lasers, whose full-width half-maximum pulse width is on the order of 100 ps, this ideal impulse assumption is no longer valid, and the IRF is required in order to deconvolve and properly fit the collected decay. It is then required that the temporal resolution of the TCSPC signal be sufficient to resolve the IRF. This can be accomplished with 25 ps time bins.

Given a repetition rate of 40 MHz, and thus a period of 25 ns, this means that 1000 time bins are required to collect the histogram. While the target number of counts per histogram is 10,000, it is unlikely that the peak number of counts per bin will exceed 1000, and so a 10-bit dynamic range would be sufficient.

The data transfer rate is a final concern with regards to the SPAD array solution. Based on the above calculation, a single histogram would be 10,000 bits in size. Since each SPAD would be transferring 256 histograms per second, then the data transfer rate for a single SPAD would be 2.56 Mbps. The entire 32 × 32 SPAD array would then have a transfer rate of 2.62 Gbps. This is comfortably possible with current generation readout speeds, such as USB 3.0, which can transfer data at a speed of 5 Gbps.

5.2.2. SPAD array characteristics

A customized SPAD array was used in these experiments. Its architecture and performance characterization have been previously reported in detail [26]. It has 32 one-dimensional pixels, which are 50 μm in diameter and spaced at 250 μm from each other. A summary of the SPAD array specifications can be found in Table 5-1. The SPAD chip has a USB output to read photon counting data from all 32 channels. It also connects to a customized TCSPC box consisting of four eight-channel time-to-amplitude converters (TAC) [26]. TCSPC histograms are compiled on-chip, and can be read out in real-time via another USB connection. Characterization experiments were performed previously on the SPAD array prototype. Results of the characterization are collected in Table 5-1.

Table 5-1: Characteristics of the 32-channel SPAD array.

pixel size	50 μm		
pixel-to-pixel pitch	250 μm		
array size	32 x 1		
pixel output dead time	16 ns (min)		
TAC dead time	250 ns		
photon detection efficiency	45% @ 540 nm (peak) 25% @ 700 nm		[26]
	-10°C	**25°C**	[26]
dark count rate (per pixel)	< 600 cps (90%) 4 kcps (max)	<10 kcps (90%) 60 kcps (max)	[26]
temporal resolution	65 ps		[26]
afterpulsing probability (-10°C)	< 1.6% (90%) 1.9% (max)		[36]
optical crosstalk	1.8% (adjacent) 0.07% (two away) negligible (further)		[36]

Many SPAD arrays are being developed using standard CMOS processes, since this allows for monolithic integration of electronics alongside the SPAD detectors, and cheaper fabrication. CMOS processes, however, have a number of limitations that are not ideal for SPAD development, including shallow implant depths, low doping concentrations, and design rule restrictions [37, 38]. This SPAD array is unique from most other emerging options because it is not made with a standard CMOS process. The customized process is more costly to fabricate, but allows greater control over their characteristics so as to achieve higher temporal resolution and better quantum efficiency.

It also presents challenges in scaling up the array. While the SPADs are fabricated via a custom process, the detection electronics are standard CMOS. What this means is that the SPAD array cannot be constructed as “smart pixels”, in which each detector’s electronics is designed to fit in the interstitial space between SPADs. Instead, the TACs are not on the same chip, and are only interfaced with the SPAD array along the perimeter. For larger SPAD arrays using this interfacing method, it becomes difficult to provide a dedicated TAC for every SPAD. Furthermore, the custom-designed SPADs and TACs are very power intensive (40 W for 32 SPADs, and 30 W for 32 TCSPC channels [26]), requiring large power supplies and heat dissipation techniques.

SPADs are able to generate an avalanche effect, where the signal for a single photon is amplified to produce a macroscopic signal. The arrival of an emitted photon results in a quickly rising current that reaches a steady-state signal in less than a nanosecond. More importantly, the jitter of this rising edge is typically in the range of picoseconds. TCSPC works by accurately discriminating the time of this rising edge relative to the excitation pulse, therefore measuring the arrival time of the photon. After many repeated trials, it is possible to generate a histogram of emitted photon arrival times, which can be fit as a fluorescence decay.

There are many important parameters involved in characterizing SPADs for photon-counting. First, the photon detection efficiency (PDE) of the detector dictates the likelihood that a photon incident on the detector will be counted. Higher efficiency is always beneficial, since this either means that the TCSPC histograms can be accumulated in a shorter time, or that a lower laser power can be used, which is less likely to damage or photobleach the sample. The uniformity of the PDE in the array is also a concern. Since the scan is done with all foci in parallel, the scan rate is limited by that of the SPAD with the worst PDE. SPADs also have an upper bound collection rate due to the 5% TCSPC limit, so increasing the laser power to accommodate the worst performing SPAD may push the best performing SPAD into a pulse pile-up situation. The PDE was previously measured using an integrating sphere and monochromator to generate uniform quantifiable light [26]. The SPADs were measured to have a peak PDE of approximately 45% at 540 nm, and a relatively slow fall-off towards longer wavelengths, still achieving 25% PDE at 700 nm.

There are actually multiple possible sources of pulse pileup distortion, beyond the 5% TCSPC limit discussed here. First, the SPAD itself has a dead time after each count, where it cannot receive another count. The dead time in this case is 20 ns, meaning it is unlikely to be a factor when compared to the 5% TCSPC limit. In other words, the 5% TCSPC limit already ensures that two photons do not arrive within the same 25 ns period, so it follows that they also would not arrive within 20 ns of each other. The TAC also has a dead time of 250 ns after each count, which could be a minor source of lost counts, but is unlikely to cause any skew to the resulting histograms [11].

Another parameter of interest is dark count rate (DCR). A dark count in this case is when an electron spontaneously sets off an avalanche effect which is not related to the arrival of a photon. Similar to dark current in an image sensor, the DCR increases with operating temperature. SPADs often vary widely in terms of their characteristic DCR, and the highest DCR would limit the speed at which the image can be acquired with a suitable signal-to-noise ratio. The DCR was previously found by measuring collection rates for each SPAD while the detector was in a dark environment [26]. At room temperature, the DCRs of the SPADs ranged from 200 cps to 60 kcps. The highest DCR is not very representative of the overall DCR distribution, as 90% of the SPADs had a DCR of less than 20 kcps. When measured at −10 °C, the range of DCR values is from 15 cps to 4000 cps, with 90% of SPADs featuring a DCR less than 600 cps. There does not appear to be any pattern as to where the high DCR SPADs are situated on the chip, and so the variability in DCR is more likely to be associated with variability in the manufacturing process of each individual SPAD than with device geometry considerations.

Afterpulsing has a unique mechanism for SPADs [39]. This is when a charge from a previous avalanche gets trapped in a material defect, and starts its own avalanche at a later time. The likelihood of this occurring is known as the afterpulsing probability (AP). The result is very similar to dark counts, except the number of erroneous counts are proportional to the collection rate. Afterpulsing is different in PMTs, since it results in a set of afterpulses at discrete time delays from the original pulse, where the time delays correspond to different ionized residual gases in the vacuum tube [40, 41]. By comparison, SPAD afterpulsing is much more uniform across the histogram and, therefore, can be removed as a uniform background subtraction [42]. Afterpulsing can be minimized by applying a longer hold-off time for the SPAD, but this comes at the cost of a reduced repetition rate for the experiment. It can also be reduced by increasing the temperature of the SPAD array, since this will reduce the lifetime of the trapping sites. Increasing the temperature, however, will also increase the DCR. The afterpulsing that remains after a hold-off period is also expected to be very long-lived, and not very sensitive to changes in temperature or longer hold-off times. The afterpulsing probability (AP) was previously measured using the time-correlated carrier counting technique and is found to be less than 1.9% across the entire SPAD array when measured at −10 °C [36].

In addition to detector-specific noise sources, a major source of uncertainty in a TCSPC histogram is shot noise due to the stochastic nature of photon counts. The dark counts and afterpulsing counts might skew the histogram towards longer decays, but this can be corrected by subtracting off the noise background. What is left once this is done is the added uncertainty in the number of counts in each bin due to these noise sources. Since shot noise is unavoidable, the goal of a good avalanche detector would be to keep extrinsic noise sources low enough that the shot noise remains the dominant source of noise in the measurements.

Optical crosstalk refers to when a light signal incident on one SPAD results in counts on adjacent SPADs. When a photon triggers an avalanche, secondary photons are emitted from the SPAD which can trigger other avalanches in nearby SPADs. This crosstalk can be caused by either direct optical paths between detectors, or light reflecting off the bottom of the chip [43]. The measure of optical crosstalk is a percentage, referring to what fraction of photon counts at the original SPAD are also measured at a secondary SPAD. The crosstalk can be measured with respect to adjacent SPADs or further removed SPADs, and diminishes quickly with distance. Optical crosstalk from a bright feature could result in artifacts appearing in the reconstructed images of adjacent SPADs. Optical crosstalk was measured between adjacent and non-adjacent SPADs, and was measured to be 1.8% for adjacent SPADs (250 μm separation), and 0.07% for next-to-adjacent SPADs (500 μm separation) [36]. SPADs at further separations resulted in negligible crosstalk.

The temporal resolution of a SPAD depends on transit time spread at the detector and the timing accuracy of the TCSPC electronics. This can be as low as tens of picoseconds. The resolution is not the whole story: the linearity of the time axis is also important in order to ensure that the collected fluorescence signal is not distorted. The time resolution was measured using a fiber laser with sub-picosecond FWHM, and was determined to be 65 ps under typical collection rates, with excellent differential non-linearity performance [26].

As discussed in the introduction, the TCSPC readout sets a limit on the allowable collection rate of 5% of the repetition rate: for a 40 MHz repetition rate, the collection rate must be kept below 2 MHz. In addition to this, the TAC has its own bandwidth limitation of 4 MHz. Therefore, in a typical one SPAD to one TAC arrangement, the collection rate is still TCSPC-limited.

Finally, when greatly multiplexing the acquisition process, the sheer size of the data readout becomes a concern. The imaging rate is ultimately limited by how quickly the data can be read out at each scan position. This depends on the data transfer protocol as well as the data size of each histogram.

5.2.3. Experimental methods

Fluorescence lifetime experiments were performed using the experimental setup is shown in Figure 5-1. The SPAD array was tested by measuring the fluorescence lifetime of Coumarin 6 using a 470 nm diode laser head (PicoQuant LDH-P-C-470, Berlin, Germany). The laser was directed towards a cuvette of Coumarin 6, and the fluorescence was collected along a perpendicular path by a pair of lenses. After passing through an emission filter (Semrock FF542/27, Rochester, NY, USA), the fluorescent light was then focused onto the SPAD array, and the positioning was adjusted in order to attain a roughly uniform collection rate of 1 Mcps across the 32 detectors. The acquisition was done at a 40 MHz repetition rate, and an acquisition time designed to achieve differing total numbers of counts. Four conditions were tested: 1000 counts, 5000 counts, 10,000 counts, and a large number of counts (20,000,000), to see the impact on lifetime estimation.

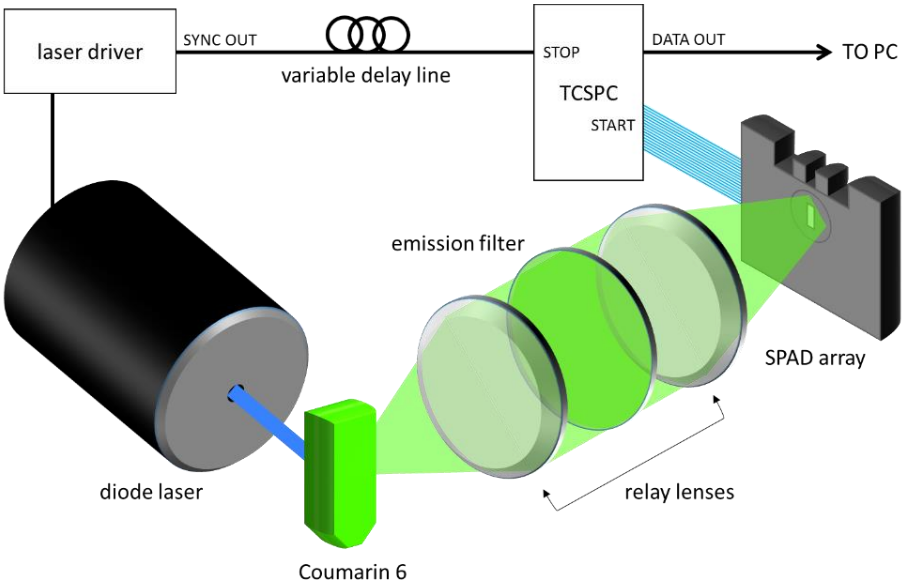

Figure 5-1: Experimental setup. Pulsed laser light is used to excite and fluoresce a cuvette of Coumarin 6 dye. The signal is collected perpendicular to the excitation using a pair of relay lenses and an emission filter, and focused onto the SPAD array. The laser driver is synchronized with the TCSPC through a variable delay line.

5.3. Results

5.3.1. Photon detection efficiency (PDE)

As the majority of fluorophores of interest have emission peaks in the 500-600 nm range, the 540 nm peak of the SPAD detector and slow roll-off towards longer wavelengths is an ideal fit.

There also appears to be great uniformity with regard to PDE across the SPAD array. At 500 nm, the PDE across all 32 channels ranges from 42% to 44%. It is worth noting that, for the application of multiplexed confocal FLIM, the SPAD with the lowest PDE can be limiting to the system. In order to achieve sufficiently high image quality across the entire region of interest, it is important that each detector is able to obtain sufficient counts. In the case where there is a high variability in PDE, the scanning process needs to be slowed down such that the SPAD with the lowest PDE can achieve a sufficient SNR. The laser power of the setup could be increased instead, but the maximum collection rate of the SPAD with the highest PDE must still be kept below 5% TCSPC limit. Fortunately, with a PDE that varies by ± 2.5%, PDE non-uniformity is not a significant issue.

5.3.2. Dark count rate (DCR)

Similar to the case of PDE, the noisiest SPAD can be severely limiting to the system. Since all of the SPADs acquire signal for the same time period, the entire scan can be slowed down by the SPAD with the highest noise in order to maintain a suitable SNR. Given that the maximum count rate is TCSPC-limited to 2 Mcps, and assuming that the pixels in the image will have a contrast ratio of at least 100:1, it is implied that there will be foci on the sample where collection rates of 20 kcps or less are expected. In these cases, it becomes quite problematic when the signal is of the same magnitude as the noise. Fortunately, the SPAD array is capable of being cooled to −10 °C. This has been tested previously in Milan, and found to reduce the largest DCR by an order of magnitude, from 60 kcps to 4 kcps [26]. The variability of SPAD DCR performance remains a concern, but appears to be manageable under cooled conditions. The relation between noisy channels and the presence of impurities is under investigation.

5.3.3. Afterpulsing probability

A maximum afterpulsing probability of 1.9% implies that a 2 Mcps SPAD would be accompanied by less than 40 kcps of spurious counts associated with afterpulsing. Afterpulsing counts cannot be directly compared to dark counts, though. Since afterpulsing counts and acquired signal both scale with the collection rate, afterpulsing is never able to dominate the signal. In contrast, while a high-level signal can effectively eliminate the impact of dark counts, afterpulsing counts scale with the signal, and so are indicative of the highest achievable SNR of the detector.

5.3.4. Comparison to shot noise

As mentioned earlier, an ideal TCSPC detector would be one in which its own noise sources are not significant when compared to the shot noise of the TCSPC process. It is then important to define equations for shot noise as well as the DCR and AP noise. The signal dS associated with a single exponential decay can be described as:

$$dS = \frac{N}{\tau}\exp\left(-\frac{t}{\tau}\right)dt \tag{5.1}$$

where N is the number of photon counts, τ is the fluorescence lifetime, and t is the histogram time. The number of photons arriving within a time window can be found by integrating the function between the time window bounds, t_1 and t_2. The shot noise ns is the square root of the number of counts in a time window, and so can be expressed as:

$$n_s = \sqrt{\int_{t_1}^{t_2} dS} = \sqrt{\frac{c\,T}{\tau}\int_{t_1}^{t_2}\exp\left(-\frac{t}{\tau}\right)dt} \tag{5.2}$$

where N has been replaced by the product of the collection rate c and the integration time T. The dark signal dD would have a uniform distribution with respect to time. This signal can be described as:

$$dD = \frac{(DCR)T}{P}dt \tag{5.3}$$

where DCR is the dark count rate and P is the period. Similarly, the number of dark counts in a time window can be found by integrating over the time bounds, and the dark noise n_D will be the square root of this value:

$$n_D = \sqrt{\int_{t_1}^{t_2} dS} = \sqrt{\frac{(DCR)T}{P}\int_{t_1}^{t_2} dt} \tag{5.4}$$

Afterpulsing signal dA can be approximated as a uniform distribution in this case as well. The signal is defined as:

$$dA = \frac{(AP)cT}{P}dt \tag{5.5}$$

where AP is the afterpulsing probability. Once more integrating over a time window and taking the square root gives the expression for afterpulsing noise n_A:

$$n_A = \sqrt{\int_{t_1}^{t_2} dA} = \sqrt{\frac{(AP)cT}{P}\int_{t_1}^{t_2} dt} \tag{5.6}$$

Using Equations 5.2, 5.4, and 5.6, an expression for the ratio of total noise n_T to shot noise n_S alone can be solved:

$$\frac{n_T}{n_S} = \frac{\sqrt{n_S^2 + n_D^2 + n_A^2}}{n_S} \tag{5.7}$$

This is solved and simplified to yield:

$$\frac{n_T}{n_S} = \sqrt{1 + \frac{\tau}{P}\left(\frac{(DCR)}{c} + (AP)\right)exp\left(\frac{t}{\tau}\right)} \tag{5.8}$$

Equation 5.8 presents how much larger the uncertainty is once the device-specific noise sources are included. Using the measured values for DCR and AP, it is possible to determine how significant of a contribution these mechanisms will have on the resulting histograms. As an example, we consider a target fluorophore with a lifetime of 5 ns. The added noise is calculated over a time window of twice the fluorescence lifetime, and for a range of collection rates from 10 kcps to 2 Mcps. The DCR of the worst performing SPAD is used for the cooled (−10 °C) and room temperature (25 °C) cases, while the afterpulsing rate of 1.9% is used. Contour plots according to Equation 5.8 are generated for these ranges of parameters in Figure 5-2.

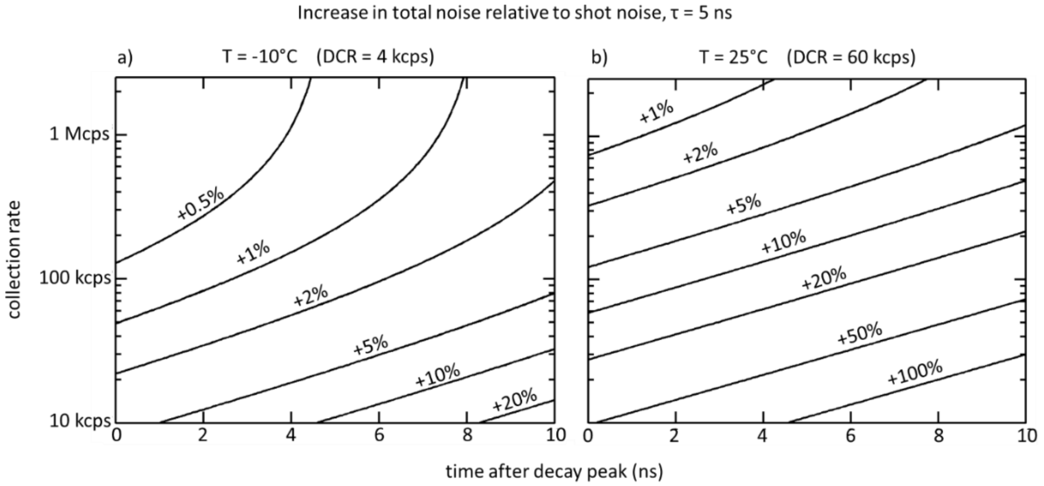

Figure 5-2: Increase in total noise along TCSPC histogram compared to shot noise alone for a 5 ns fluorescence decay at (a) T = -10°C and (b) T = 25°C. Contour lines indicate the increase in total noise in terms of percentage of the shot noise.

5.3.5. Optical crosstalk

In the context of the multiplexed confocal microscope, optical crosstalk represents another type of signal contamination. There is still a time-correlated nature to it, and so the time-resolved signal from one channel can spread into an adjacent channel, adding its own lifetime components, as well as its intensity. While a 2% contribution of crosstalk may not be very significant when adjacent SPADs are receiving photons at roughly the same collection rates, it can be quite problematic when a SPAD is measuring low-level signals while adjacent SPADs are measuring high signals. In other words, this affects the maximum contrast ratio that can be obtained in a reconstructed image. This would also be a more critical issue in a 2D SPAD arrangement, when each SPAD has eight adjacent SPADs that can contribute to crosstalk.

It is worth noting that the optical crosstalk of this 32-channel SPAD array was an order of magnitude higher than the crosstalk value measured in the Milan group's eight-channel SPAD array (0.2%). It is suspected that the cause of the increased crosstalk is due to a change in device substrate. If the crosstalk can be reduced to these previously attained levels, then it should not cause significant intensity or temporal artifacts in a reconstructed FLIM image.

5.3.6. Temporal resolution

With the current design, the TCSPC histogram is divided into 2^{14} columns, meaning that the temporal bin size for a 25 ns full scale range is 1.5 ps. This is far below the temporal resolution of the SPAD array, adding nothing to the actual resolution while requiring more data to be transferred.

5.3.7. Lifetime estimation

The standard log-linear fit method was employed. First the TCSPC histograms were temporally binned to have a 50 ps bin size. An example of this is shown in Figure 5-3(a). Next, the flat noise level was subtracted from each histogram. The histograms were then truncated to start at the peak of the decay. The logarithm was taken of each histogram, such that a single exponential decay becomes a first-order polynomial, and the negative inverse of its slope is the fluorescence lifetime. Finally, a linear least squares fit was performed, but this fitting was truncated to end at the first bin with zero counts. The resulting lifetime fits for one of the SPADs are shown in Figure 5-3(b). The average lifetime estimated under

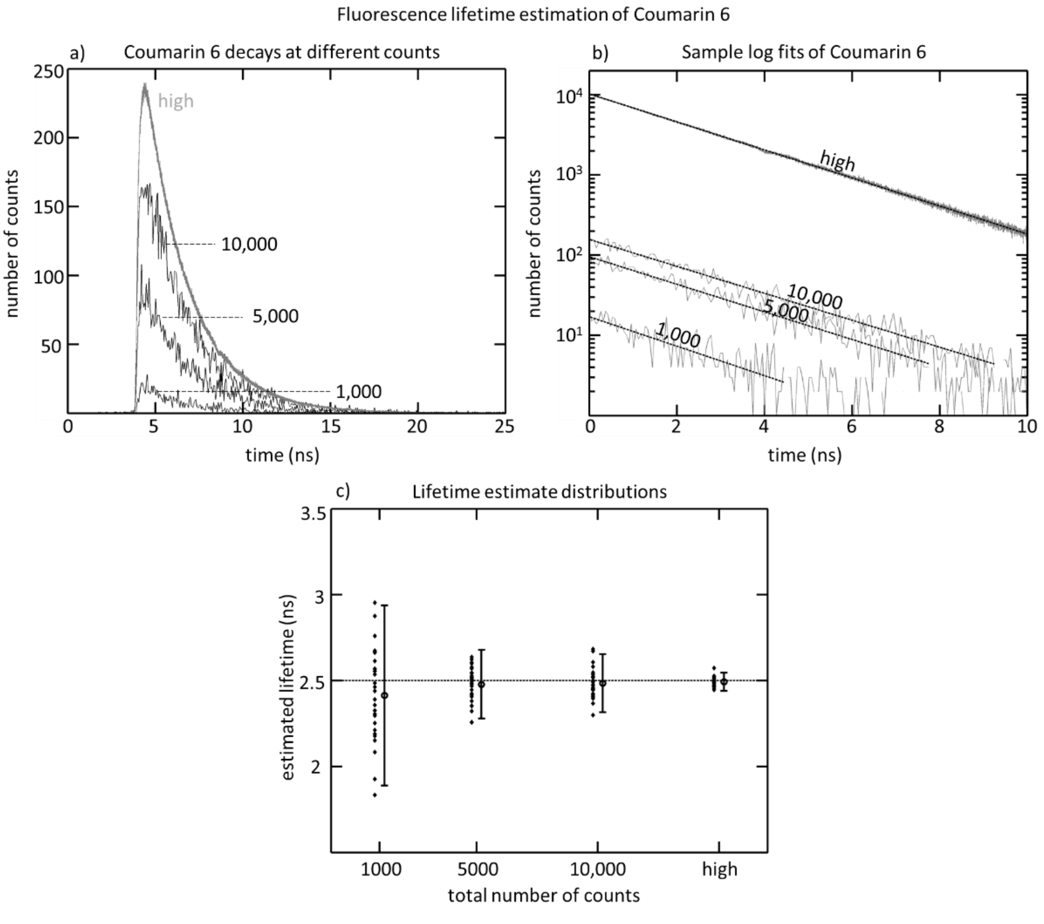

Figure 5-3: Fluorescence lifetime estimation of Coumarin 6. (a) TCSPC histograms for a SPAD after a range of different numbers of photon counts. The decay resulting from a "high" (>20,000,000) number of counts is scaled independently of the other three cases, and so does not correspond with the left axis; (b) logarithmic fits of TCSPC histograms under different count scenarios; and (c) results for lifetime estimation under each count scenario, as an ensemble of all SPADs in the array, with 95% confidence interval bounds.

each count condition are shown in Figure 5-3(c), with 95% confidence interval bounds associated with all of the SPADs' individual measurements.

5.4. Discussion

5.4.1. Noise performance

The benefit of cooling the SPAD array to −10 °C is clear in the plots in Figure 5-2. At 25 °C, AP noise is insignificant compared to DCR noise. In Figure 5-2(b), it can be seen that a weak 10 kcps fluorescence signal (along the horizontal axis) will already have 50% larger uncertainty than in the ideal shot noise case, and the uncertainty increases to twice the ideal value at a point 5 ns away from the decay peak. However, at −10 °C (Figure 5-2(a)), under the same conditions, these device-specific noise sources only increase the ideal shot noise by <5% and 10%, respectively. It is also clear that AP becomes the dominant source of added noise at higher collection rates.

The significance of these results depends greatly on how the histogram data is analyzed. It varies with which sections of the decay are important for the given lifetime estimation method. It could be that the shot noise is already at an insignificant level for the estimation, and so a doubling of this uncertainty is not very detrimental. In the case of HCS however, where you are likely to be starved for photon counts, a doubling of the uncertainty can, instead, be interpreted as requiring the scan rate to be reduced by a factor of four compared to the speed of an ideal TCSPC performance.

The plots in Figure 5-2 are calculated for a fluorescence lifetime of 5 ns. It is worth noting that shorter lifetime decays, as they are less spread out across the histogram, would be less affected by the device-specific noise sources.

5.4.2. Lifetime estimation

The lifetime estimation experiment is not meant to demonstrate the precision with which a fluorescence lifetime can be found, since it depends on the lifetime extraction technique. Instead, it is designed to show the agreement between the lifetime of a standard fluorophore and all 32 channels of the SPAD array. The results show this to be true, as the estimated lifetime is more tightly restricted to the expected lifetime with an increasing number of counts.

It is also important to mention that no TCSPC channels tended to systematically over- or underestimate the fluorescence lifetime, and so the variability in lifetime measurement is a random spread. The TACs are found to be very linear and predictable.

5.4.3. Towards a 32 x 32 array

The current challenge for the Milan team is to increase the custom-fabricated SPAD array size to 32 × 32. This would be extremely attractive to HCS FLIM applications, achieving roughly the same multiplexing level as spinning disk confocal, but with the benefit of TCSPC collected behind each pixel.

As discussed briefly earlier, the task of scaling up the SPAD array is not straightforward. The primary issue is that the SPAD array chip needs to interface with the TAC array in a non-monolithic arrangement. This quickly becomes challenging when there are hundreds of SPADs. There is also the concern of bandwidth: if there are 1024 TACs that are each converting millions of counts to a timestamp each second, the data flow on the device quickly becomes unmanageable.

The proposed solution is to instead use 64 undedicated TACs to interface with the 1024 SPADs. A smart router setup has been designed whereby a detected photon count signal is routed to the next available TAC [44]. Each TAC has a maximum collection rate of 4 Mcps. This was not important before because the collection rate was ultimately limited by the 5% TCSPC limit for a single SPAD. In a smart router scenario where each TAC is not dedicated to a single SPAD, this limit no longer exists. It is, therefore, possible for 64 TACs to achieve a global collection rate of 256 Mcps.

For a uniform fluorescent sample, this would mean that each SPAD is limited to a collection rate of 250 kcps—significantly lower than the 2 Mcps afforded by the 5% TCSPC limit. Fortunately, images are typically more interesting than a uniform field. Due to the TAC smart routing, darker regions on a sample contribute less to the capacity of the TACs, and allow for brighter areas to exceed the 250 kcps average. For instance, if half of the foci are not collecting any signal, then the other half could have a collection rate of 500 kcps. This capability would definitely depend on the target sample, but it is quite possible for a sparsely populated cell well to be unhindered by a dearth of TACs. In contrast, the Megaframe MF32 CMOS-based 32 × 32 SPAD array allows for a global collection rate of 500 Mcps, but each individual SPAD is limited to 500 kcps readout when using the entire array, consistent with the 500 kfps full-frame rate [23].

Data transfer rate is the other concern. As outlined as a requirement for HCS FLIM, the entire data transfer for a 512 × 512 image should be done in 1 s. For the case where 2^{14} time channels are used with a bit depth of 16 bits for each histogram, this amounts to a required data transfer rate of 69 Gbps—drastically higher than today’s data connection standards. For our purposes, however, the number of time channels and bit depth are not sensible. If only 2^{10} time channels (25 ps per channel) and 10-bit-depth histograms (maximum 1024 counts per channel) are needed, the required data transfer rate is reduced to 2.7 Gbps—well within the 5 Gbps capabilities of a USB 3.0 connection.

5.5. Conclusions

The advent of the SPAD array brings great promise to many fields of research, and the advantages to HCS FLIM cannot be overstated. With the capability of multiplexing confocal and two-photon FLIM, SPAD array technology could finally make it feasible to apply FLIM-FRET protein-protein interaction studies to the realm of HCS. This would be a major advance for the drug discovery process.

There are a number of unique characteristics to SPADs that need to be taken into account when considering a multiplexed confocal setup. The PDE determines the SPAD’s collection rate, while the DCR and afterpulsing determine the noise on the SPAD signal. The uniformity of each of these properties is also important. SPADs are prone to having sporadically high DCRs, for instance, which could mean that certain SPADs are collecting significantly lower quality signals. Optical crosstalk is another factor that could have significant effects on the multiplexed FLIM process. The impact of these factors on lifetime estimation is worth investigating further.

We also showed that the design of the 32 × 32 SPAD array should be able to perform FLIM imaging at a speed and precision suitable for HCS. Though the global collection rate is limited, the smart routing TAC setup should not significantly limit the collection rate for a typical live cell sample. The data transfer rate, when the TCSPC histogram data structure is reduced in size, should be well within the capabilities of USB 3.0 bandwidth.

Acknowledgements

This work was supported in part by the Ontario Centres of Excellence through a Market Readiness grant, the Natural Sciences and Engineering Research Council of Canada through an Idea to Innovation Grant and Industry Postgraduate PhD Scholarship (AT), and the Canadian Foundation of Innovation. QF held the Canada Research Chair in Biophotonics.

Author contributions

A.T., P.P., I.R. and Q.F. conceived and designed the experiments and analyzed the data; A.T. and P.P. performed the experiments; NH contributed to the introduction; M.J.D. contributed to the discussion of the results; A.T. wrote the paper.

Conflicts of interest

The authors declare no conflict of interest.

References

[1] M. Bickle, "The beautiful cell: high-content screening in drug discovery," *Analytical and bioanalytical chemistry,* vol. 398, no. 1, pp. 219-226, 2010.

[2] F. Gaspari, "An overview of cell phenotypes in HCS: limitations and advantages," *Expert Opinion on Drug Discovery,* vol. 4, no. 6, pp. 643-657, 2009.

[3] Y. Sun, R. Day and A. Periasamy, "Investigating protein-protein interactions in living cells using fluorescence lifetime imaging microscopy," *Nature Protocols,* vol. 6, no. 9, pp. 1324-1340, 2011.

[4] H. Wallrabe and A. Periasamy, "Imaging protein molecules using FRET and FLIM microscopy," *Current Opinion in Biotechnology,* vol. 16, no. 1, pp. 19-27, 2005.

[5] E. J. Osterlund, Q. Liu and D. W. Andrews, "The use of FLIM-FRET for the detection of mitochondria-associated protein interactions," in *Mitochondrial Medicine I: Probing Mitochondrial Function*, New York, Springer, 2015, pp. 395-419.

[6] D. Matthews, L. Carlin, E. Ofo, P. Barber, B. Vojnovic, M. Irving, T. Ng and S. Ameer-Beg, "Time-lapse FRET microscopy using fluorescence anisotropy," *Journal of Microscopy,* vol. 237, no. 1, pp. 51-62, 2010.

[7] H. C. Ishikawa-Ankerhold, R. Ankerhold and G. P. C. Drummen, "Advanced fluorescence microscopy techniques - FRAP, FLIP, FLAP, FRET and FLIM," *Molecules,* vol. 17, no. 4, pp. 4047-4132, 2012.

[8] J. Lakowicz, "Time-Domain Lifetime Measurements," in *Principles of Fluorescence Spectroscopy,* New York, Springer, 2006, pp. 97-155.

[9] W. Becker, "Fluorescence lifetime imaging - techniques and applications," *Journal of Microscopy,* vol. 247, no. 2, pp. 119-136, 2012.

[10] K. Suhling, P. M. French and D. Phillips, "Time-resolved fluorescence microscopy," *Photochemical and photobiological sciences,* vol. 4, no. 1, pp. 13-22, 2005.

[11] J. Arlt, D. Tyndall, B. R. Rae, D. D.-U. Li, J. A. Richardson and R. K. Henderson, "A study of pile-up in integrated time-correlated single photon counting systems," *Review of Scientific Instruments,* vol. 84, p. 103105, 2013.

[12] D. Palubiak, M. El-Desouki, O. Marinov, M. J. Deen and Q. Fang, "High-speed, single-photon avalanche-photodiode imager for biomedical applications," *IEEE Sensors,* vol. 11, no. 10, pp. 2401-2412, 2011.

[13] A. V. Agronskaia, L. Tertoolen and H. C. Gerritsen, "High frame rate fluorescence lifetime imaging," *Journal of Physics D: Applied Physics,* vol. 36, pp. 1655-1662, 2003.

[14] S. E. Webb, Y. Gu, S. Lévêque-Fort, J. Siegel, M. J. Cole, K. Dowling, R. Jones, P. M. French, N. R. Juskaitis, O. D. Sucharov, T. Wilson and M. J. Lever, "A wide-field time-domain fluorescence lifetime imaging microscope with optical sectioning," *Review of Scientific Instruments,* vol. 73, no. 4, p. 1898, 2002.

[15] P. Schneider and R. Clegg, "Rapid acquisition analysis and display of fluorescence lifetime-resolved images for real-time applications," *Review of Scientific Instruments,* vol. 68, no. 11, pp. 4107-4119, 1997.

[16] J. Philip and K. Carlsson, "Theoretical investigation of the signal-to-noise ratio in fluorescence lifetime imaging," *Journal of the Optical Society of America A,* vol. 20, no. 2, pp. 368-379, 2003.

[17] Q. Zhao, I. Young and J. de Jong, "Photon budget analysis for fluorescence lifetime imaging microscopy," *Journal of Biomedical Optics,* vol. 16, no. 8, p. 086007, 2011.

[18] S. Wachsmann-Hogiu, D. Krakow, V. T. Kirilova, D. H. Cohn, C. Bertolotto, D. Acuna, Q. Fang, N. Krivorov and D. L. Farkas, "Multiphoton, confocal, and lifetime microscopy for molecular imaging in cartilage," *Proc. SPIE 5699,* no. 75, 2005.

[19] W. F. An and N. Tolliday, "Cell-based assays for high-throughput screening," *Molecular Biotechnology,* vol. 45, no. 2, pp. 180-186, 2010.

[20] C. Niclass, M. Sergio and E. Charbon, "A single photon avalanche diode array fabricated in deep-submicron CMOS technology," in *Proceedings of the Design, Automation and Test in Europe Conference,* Munich, 2006.

[21] J. S. Lapington, T. J. R. Ashton, D. Ross and T. Conneely, "Progress towards a 256 channel multi-anode microchannel plate photomultiplier system with picosecond timing," *Nuclear Instruments and Methods in Physics Research A,* vol. 695, pp. 78-82, 2012.

[22] W. Becker, L. Hirvonen, J. Milnes, T. Conneely, O. Jagutzki, H. Netz, S. Smietana and K. Suhling , "A wide-field TCSPC FLIM system based on an MCP PMT with a delay-line anode," *Review of Scientific Instruments,* vol. 87, no. 9, 2016.

[23] N. Krstajic, S. Poland, J. Levitt, R. Walker, A. Erdogan, S. Ameer-Beg and R. K. Henderson, "0.5 billion events per second time correlated single photon counting using CMOS SPAD arrays," *Optics Letters,* vol. 40, no. 18, pp. 4305-4308, 2015.

[24] C. Niclass, C. Favi, T. Kluter, M. Gersbach and E. Charbon, "A 128 x 128 single-photon image sensor with column-level 10-bit time-to-digital converter array," *IEEE Journal of Solid-State Circuits,* vol. 43, no. 12, pp. 2977-2989, 2008.

[25] F. Villa, B. Markovic, S. Bellisai, D. Bronzi, A. Tosi, F. Zappa, S. Tisa, D. Durini, S. Weyers, U. Paschen and W. Brockherde, "SPAD smart pixel for time-of-flight and time-correlated single-photon counting measurements," *IEEE Photonics Journal,* vol. 4, no. 3, pp. 795-804, 2012.

[26] A. Cuccato, S. Antonioli, M. Crotti, I. Labanca, A. Gulinatti, I. Rech and M. Ghioni, "Complete and compact 32-channel system for time-correlated single-photon counting measurements," *IEEE Photonics,* vol. 5, no. 5, p. 6801514, 2013.

[27] F. Guerrieri, S. Tisa, A. Tosi and F. Zappa, "Two-dimensional SPAD imaging camera for photon counting," *IEEE Photonics Journal,* vol. 2, no. 5, pp. 759-774, 2010.

[28] S. Kawahito, G. Baek, Z. Li, S. Han, M. Seo, K. Yasutomi and K. Kagawa, "CMOS Lock-in Pixel Image Sensors with Lateral Electric Field Control for Time-Resolved Imaging," in *International Image Sensor Workshop,* Snowbird, Utah, 2013.

[29] H. Chen, G. Holst and E. Gratton, "Modulated CMOS camera for fluorescence lifetime microscopy," *Microscopy Research and Technique,* vol. 78, no. 12, pp. 1075-1081, 2015.

[30] Hamamatsu Photonics, "Microchannel Plate Photomultiplier Tubes (MCP-PMT) R3809U-50 Series," Hamamatsu Photonics, Iwata, 2015.

[31] PicoQuant GmbH, "PDM Series Single Photon Avalanche Diodes," PicoQuant GmbH, Berlin, 2015.

[32] PicoQuant GmbH, "PMA Series Photomultiplier Detector Assembly," PicoQuant GmbH, Berlin, 2014.

[33] W. Becker, B. Su, O. Holub and K. Weisshart, "FLIM and FCS detection in laser-scanning microscopes: increased efficiency by GaAsP hybrid detectors," *Microscopy Research and Technology,* vol. 74, no. 9, pp. 804-811, 2011.

[34] A. Tsikouras, J. Ning, S. Ng, R. Berman, D. W. Andrews and Q. Fang, "Streak camera crosstalk reduction using a multiple delay optical fiber bundle," *Optics Letters,* vol. 37, pp. 250-252, 2012.

[35] A. Tsikouras, R. Berman, D. Andrews and Q. Fang, "High-speed multifocal array scanning using refractive window tilting," *Biomedical Optics Express,* vol. 6, no. 10, pp. 3737-3747, 2015.

[36] A. Cuccato, "Development of electronic systems for single-photon avalanche diode arrays [thesis]," Politecnico di Milano, Milan, 2013.

[37] J. A. Richardson, L. A. Grant and R. K. Henderson, "A low dark count single photon avalanche diode structure compatible with standard nanometer scale CMOS technology," *IEEE Photonics Technology Letters,* vol. 21, no. 14, pp. 1020-1022, 2009.

[38] D. P. Palubiak and M. J. Deen, "CMOS SPADs: design issues and research challenges for detectors, circuits and arrays," *IEEE Journal of Selected Topics in Quantum Electronics,* vol. 20, no. 6, p. 600718, 2014.

[39] D. Palubiak, Z. Li and M. J. Deen, "Afterpulsing characteristics of free-running and time-gated single-photon avalanche diodes in 130-nm CMOS," *IEEE Transactions on Electron Devices,* vol. 62, no. 11, pp. 3727-3733, 2015.

[40] U. Akgun, A. Ayan, G. Aydin, F. Duru, J. Olson and Y. Onel, "Afterpulse timing and rate investigation of three different Hamamatsu photomultiplier tubes," *Journal of Instrumentation,* vol. 3, no. 1, p. T01001, 2008.

[41] P. Coates, "The origin of afterpulses in photomultipliers," *Journal of Physics D: Applied Physics,* vol. 6, pp. 1159-1166, 1973.

[42] J. Enderlein and I. Gregor, "Using fluorescence lifetime for discriminating detector afterpulsing in fluorescence correlation spectroscopy," *Review of Scientific Instruments,* vol. 76, no. 033102, 2005.

[43] I. Rech, A. Ingargiola, R. Spinelli, I. Labanca, S. Marangoni, M. Ghioni and S. Cova, "Optical crosstalk in single photon avalanche diode arrays: a new complete model," *Optics Express,* vol. 16, no. 12, pp. 8381-8393, 2008.

[44] G. Acconcia, M. Crotti, I. Rech and M. Ghioni, "High-performance timing electronics for single photon avalanche diode arrays," *SPIE Proceedings,* vol. 9504, p. 95040A, 2015.

Chapter 6

Conclusions and future work

The application of fluorescence lifetime imaging microscopy to high-content screening, and development of a multifocal confocal microscope module using a streak camera is presented in this thesis. This chapter provides a summary of this work, as well as a discussion on the system's shortcomings and suggestions for future improvements based on emerging technologies.

6.1. Summary

There is a lot of promise in the application of a high resolution fluorescence lifetime imaging microscopy (FLIM) modality to the high-content screening (HCS) process. The ability to accurately measure Förster resonant energy transfer (FRET) between proteins involved in regulating cellular pathways allows for an unprecedented level of insight into the mechanisms of action in a phenotypic screening assay. This more informed approach allows for better optimization of drug leads and can also predict their unwanted off-target effects. With proper implementation of this technique at the high resolution and high throughput rates required for HCS, there is the potential to significantly reduce the number of failed drug candidates in clinical testing, as well as the average drug development cost.

This thesis dissertation has presented improvements made to our multifocal FLIM system in order to make it more ready to be implemented in an HCS microscope. These following milestones have been achieved towards these improvements:

1. The 2D-1D fiber array was characterized to demonstrate its effectiveness at reducing optical crosstalk. The fiber array scheme was validated using a fluorophore with a known fluorescence lifetime, and a reconstruction of a fixed sample was used in order to demonstrate the impact that reducing the optical crosstalk has on image quality (Chapter 3).

2. A refractive galvanometer scanner was developed in order to uniformly shift the array of foci with high resolution. The scanner was tested to ensure high linearity and uniformity of the foci motion while scanning, and a fixed sample was successfully scanned and reconstructed (Chapter 4).
3. An explorative study was done on a prototype 32-channel single-photon avalanche diode (SPAD) array. Fluorescence lifetime estimations of a known standard were performed with the SPAD array, and calculations were done in order to relate SPAD characteristics to parameters relevant to HCS FLIM implementation. Theoretical calculations were done in terms of the collection rate and data throughput of a future 32 x 32 SPAD array based on the same design (Chapter 5).
4. The streak camera was upgraded to a synchroscan sweep unit, raising the repetition rate of the system to 40 MHz. An updated 2D-1D fiber array was designed to match the synchroscan approach, and time axis linearization algorithms were developed in order to correct the fluorescence lifetime decay streaks.
5. The optical power and throughput of the experimental setup was improved in several ways. The diode laser was upgraded in terms of power output and desired excitation wavelength. The beam shaper was replaced with a square core fiber that allows for significantly better throughput. The microlens arrays and scanner windows were also given an antireflective (AR) coating to reduce optical losses at each interface.

The resulting system has been upgraded in nearly every aspect. These changes are summarized in Table 6-1. While the system still falls short of the 1-second acquisition time expected of HCS, it can now accomplish in 16 seconds what the original system could only manage in 13 minutes. The main remaining limitations are based on the frame rate of the streak readout camera as well as collecting a sufficient fluorescence signal to make use of the high speed.

Table 6-1: Improvements to each aspect of the original HCS-FLIM system

	Original System	**Current System**
Excitation	405nm 2mW diode laser, 4 MHz	440nm 40mW diode laser, 40 MHz
Beam Shaping	Cylindrical lens beam shaper	Square core fiber beam shaper
Scanner	Motorized microscope stage	Window galvanometers
Optical path	Uncoated microlens arrays	AR-coated microlens arrays
Streak camera sweep	Slow triggered sweep unit (< 4 MHz)	Synchroscan sweep unit (40 MHz)
Readout	CCD camera (7.5 fps)	sCMOS camera (100 fps)

6.2. Future Work

While the current prototype has demonstrated the feasibility of the design, there are still hurdles to pass in order to make it a viable HCS module.

6.2.1. Streak camera improvements

The streak camera was upgraded to a 40 MHz synchroscan sweep unit in order to increase the repetition rate of the pulsed laser, and therefore reduce the required acquisition time. 40 MHz corresponds to a period of 25 ns, which is considered ideal for a typical fluorophore's fluorescence signal to have sufficiently decayed. For instance, a 5 ns lifetime decay would be reduced to 0.7% of its peak intensity at the end of the period. However, a 40 MHz synchroscan involves a sinusoidal sweep back and forth, meaning that the effective time across the screen is only 12.5 ns – and actually less after the turnaround points at the sweep edges are excluded. After 12.5 ns, a 5 ns lifetime decay is only reduced to 8% of its peak intensity, and the remaining decay tail will fold over and become traced on top of the decay. Finally, when optical crosstalk is taken into consideration with a fiber delay scheme, this one-way time range needs to be divided once more in order for the two sets of different length fibers to be isolated from each other. This means that only a 6.3 ns optical-crosstalk-reduced time window is available for each decay, which is insufficient for most fluorophores. One possible solution to this would be to replace the synchroscan sweep unit with a 20 MHz version at the cost of reduced repetition rate. There are also alternative methods to reduce the optical crosstalk without shifting the arrival time of alternating fibers, such as taking advantage of the lateral space on the entrance photocathode, or using a specialized photocathode to accomplish this [1].

The acquisition speed of the streak readout camera is also a limiting factor in terms of acquisition speed, and is what currently limits the system from attaining faster than 16 second acquisitions of 400 x 400 reconstructions. The sCMOS camera is capable of 100 fps readout of the 1600 x 1052 subregion fitting the streak camera's output region. There could be gains in readout speed by increasing the demagnification of the phosphor screen onto the sensor to use a smaller readout region. The fiber array pitch is approximately 10 pixels on the readout, which leaves some room for shrinking the image while still being able to resolve the individual streaks. Frame rate typically scales with the number of rows read out, so this is a simple way to improve the acquisition speed, though it would not improve the readout speed to 1600 fps. Ultimately, the 1.5 ms lifetime decay of the P43 phosphor screen prevents significant improvements in the frame rate anyhow, before ghosting begins to occur between frames [2, 3]. While this could be corrected for, it would come at the cost of reduced signal quality.

The low collection efficiency of the streak camera, however, represents the primary challenge for the system. Its 5% photodetection efficiency means that 19 out of 20 photon counts are not detected. This is an unreasonable level of wasted photon counts, given that live cell imaging at high speeds is going to be a photon-starved situation anyhow. Despite significant efforts to improve the optical throughput at every stage leading up to the streak camera, its inherent losses are enough to challenge the concept's feasibility. To put it in perspective, a SPAD detector typically has 50% collection efficiency. Time-correlated single-photon counting (TCSPC) limits the collection rate of a SPAD detector to 2 Mcps in order to prevent pulse pileup, which is 4 Mcps photons incident on the detector. A streak camera would require an incident photon flux of greater than 40 Mcps in order for it to collect the same signal level, and even then, it would still have higher analog noise than a TCSPC detector. The fluorescent proteins expressed in live cells cannot generate these high photon fluxes, and sufficiently high excitation power would certainly lead to photobleaching and photodamage. Even with its multiplexed approach, the streak camera is too wasteful with the limited number of photon counts available.

6.2.2. Alternative detectors

When the decision to use a streak camera was made, the major advantage was its parallel detection of 100 fluorescence signals – something that current TCSPC detectors could not provide. This fact has changed with the recent advancements in SPAD arrays and TCSPC electronics. SPAD arrays with over 1000 independent detectors are emerging: The MegaFrame 32 x 32 CMOS SPAD array recently became a commercial product under the spinoff company Photon Force [4], while there are several other research efforts in this direction as well [5, 6, 7]. SPAD arrays are now able to outcompete the streak camera in terms of multiplexing, while maintaining the strong advantage in detection efficiency. The clear direction for the project would be to seriously consider using a SPAD array as the time-resolved detector for the system. Extending the degree of multiplexing to the 1024 available in these emerging SPAD arrays would bring the system closer to the level of multiplexing present in spinning disk confocal systems.

Alternatively, there have also been advances in time-gated detectors. Originally, there were three main drawbacks to time-gated imaging: the gated sensor rejects the vast majority of the signal, the image intensifier introduces significant analog noise to the signal, and the time resolution is not fine enough. Instead of using an intensified CCD (ICCD), emerging devices can accomplish the time gating on a CMOS sensor and reduce the first two of these drawbacks. The MPD SPC^3 detector uses an array of 32 x 64 SPADs that is capable of a 1.5 ns time gate [8]. Similarly, the SwissSPAD contains an array of 512 x 128 SPADs with a minimum of 4 ns gating [9]. Since the signal in these detectors is acquired with photon-counting, there is significantly less noise than with an ICCD. Another recent gating 256 x 512 pixel detector is able to split an incoming signal between two 6.3 ns taps based on arrival time, meaning a two-window time-resolved signal can be acquired in a single acquisition without rejecting photon counts [10]. The PCO FLIM detector works along a similar principal to split the signal along two bins. Though it has been designed for frequency domain FLIM applications, the device could in principle be used in the time domain as well [11].

There are a number of good emerging options for highly parallel fluorescence lifetime measurement. The TCSPC SPAD arrays are a particularly good match for our system, due to their sparser 32 x 32 size and their sub-nanosecond time resolution. The one concern with TCSPC SPAD arrays is the sheer quantity of data that needs to be read out, as is outlined in Chapter 5 for the future 32 x 32 design. The time gating options are also impressive, though the long gating windows do impact the temporal resolution that can be achieved by the sensors. There are methods to shift the time gates by small increments in order to achieve higher temporal resolution, though this comes at the cost of acquisition speed, and still cannot compare to TCSPC for temporal resolution.

6.2.3. Scanner improvements

Regardless of which type of solid-state detector is used, one clear trend is that switching from a streak camera could allow for at least 10 times as many foci to be used to scan the sample. This would require a suitably large microlens array, as well as a large enough pair of scanner windows to contain the new array. This adds some inertia to the load, though more powerful galvanometer motors are available that could handle this without sacrificing scan speed.

The galvo scanners should also be designed for continuous scanning, in order to ensure that the galvo scanner does not become the acquisition speed limiting step. This will require careful synchronization between the galvo controller and the detector in order to ensure that frames are being acquired at the right times.

6.2.4. Flexible optical path

There are a number of small changes along the optical path that could greatly improve the usability of the instrument.

First, the design needs to be extended to include multiple excitation sources as well as corresponding filter sets. A laser merge module can be included to control the different sources. Either a multiband dichroic filter or a dichroic filter wheel should be installed along with an emission filter wheel. This will allow for donor and acceptor excitation, as well as flexibility for different experiments. This is the expectation for a commercial confocal system.

The choice of microscope objective impacts the optimal entrance f-number at the conjugate plane. Depending on the type of objective and magnification, the optimal f-number can vary from f/13 to f/25. In order to allow the user the option of selecting any objective, the relay lens before the microscope should also be switchable in order to best accommodate the selected objective.

It could also be useful to have switchable lenses directly following the square core beam shaper, in order to adjust the output size of the excitation square. This would allow the user to be able to balance between the degree of multiplexing and the optical power that is delivered to each beam. Reducing the number of foci could also result in faster detector readout, depending on the choice of detector.

6.2.5. Alternative imaging modalities

While the targeted application for the system has always been towards FLIM applications, the module itself is a multifocal scanner that can be used with any type of detector – with the advantage being specialized sparse detectors that are able to provide some benefit compared to spinning disk confocal. Intensity imaging with SPAD arrays could be done, for example, which would provide discrete photon counting for improved signal-to-noise ratio compared to spinning disk. It is also possible to take advantage of the space between foci: a prism-based spectrometer technique could be used to create an emission spectrum in this space, enabling high-speed hyperspectral imaging.

6.3. Conclusion

The work presented in this dissertation have been aimed towards the improvement in acquisition speed and photon economy of the HCS-FLIM module. There have been a collection of advances that have brought this system closer to its goal as a high-throughput screening tool. The optical crosstalk of fiber channels at the streak camera was reduced through the use of an alternating fiber delay scheme. A fast and compact window galvanometer scanner was developed and implemented that allowed for the entire foci array to be scanned linearly and uniformly. The streak camera was upgraded with a synchroscan sweep unit, and a unique fiber array design and linearization scheme was implemented. An exploration was performed on one of the emerging solid-state detectors that could soon replace the streak camera. Finally, a number of small improvements were made to improve the system’s optical throughput. The resulting system is capable of scan speeds that approach the 1 FLIM image / second benchmark of HCS, given a sufficiently large fluorescent signal.

As the system design advances, new detector options will likely be considered to replace the streak camera, in order to improve the photodetection efficiency. There is also a trend towards a higher degree of multiplexing, and better flexibility in order to work with a large variety of objectives and microscope platforms. There is also the possibility of using the system for applications other imaging modalities besides FLIM.

References

[1] J. Qu, L. Liu, D. Chen, Z. Lin, G. Xu, B. Guo and H. Niu, "Temporally and spectrally resolved sampling imaging with a specially designed streak camera," *Optics Letters,* vol. 31, no. 3, pp. 368-370, 2006.

[2] Optronis GmbH, "Optronis SC-10 Streak Camera Main Unit," March 2014. [Online]. Available: http://www.optronis.com/fileadmin/Upload/Product/Streak/SC-10.pdf. [Accessed 17 January 2017].

[3] Stanford Computer Optics, "Image intensifier: Phosphor screen," 2013. [Online]. Available: http://www.stanfordcomputeroptics.com/technology/image-intensifier/phosphor-screen.html. [Accessed 2 February 2017].

[4] Photon Force, "Photon Force - Accelerating progress in the fight against disease," 2017. [Online]. Available: https://www.photon-force.com/. [Accessed 2 February 2017].

[5] A. Cuccato, S. Antonioli, M. Crotti, I. Labanca, A. Gulinatti, I. Rech and M. Ghioni, "Complete and compact 32-channel system for time-correlated single-photon counting," *IEEE Photonics Journal,* vol. 5, no. 5, 2013.

[6] F. Villa, R. Lussana, D. Tamborini, A. Tosi and F. Zappa, "High-fill-factor 60 x 1 SPAD array with 60 subnanosecond integrated TDCs," *IEEE Photonics Technology Letters,* vol. 27, no. 12, pp. 1261-1264, 2015.

[7] C. Niclass, C. Favi, T. Kluter, M. Gersbach and E. Charbon, "A 128 x 128 single-photon image sensor with column-level 10-bit time-to-digital converter array," *IEEE Journal of Solid-State Circuits,* vol. 43, no. 12, pp. 2977-2989, 2008.

[8] M. Vitali, D. Bronzi, A. J. Krmpot, S. N. Nikolic, F.-J. Schmitt, C. Junghans, S. Tisa, T. Friedrich, V. Vukojevic, L. Terenius, F. Zappa and R. Rigler, "A single-photon avalanche camera for fluorescence lifetime

microscopy and correlation spectroscopy," *IEEE Journal of Selected Topics in Quantum Electronics*, vol. 20, no. 6, p. 3804010, 2014.

[9] S. Burri, F. Polowny, C. Bruschini, X. Michalet, F. Regazzoni and E. Charbon, "A 65k pixel, 150k frames-per-second camera with global gating and micro-lenses suitable for fluorescence lifetime imaging," in *Proceedings of SPIE 9141: Optical Sensing and Detection III, 914109*, Brussels, 2014.

[10] M.-W. Seo, K. Kagawa, K. Yasutomi, Y. Kawata, N. Teranishi, Z. Li, I. A. Halin and S. Kawahito, "A 10 ps time-resolution CMOS image sensor with two-tap true-CDS lock-in pixels for fluorescence lifetime imaging," *IEEE Journal of Solid-State Circuits,* vol. 51, no. 1, pp. 141-154, 2016.

[11] R. Franke and G. A. Holst, "Frequency-domain fluorescence lifetime imaging system (pco.flim) based on a in-pixel dual tap control CMOS image sensor," in *Proceedings of SPIE 9328, Manipulation and Analysis of Biomolecules, Cells, and Tissues XIII, 93281K,* San Francisco, 2015.